Late First-Row Transition Metals in Weak Ligand Fields - Correlating High-Spin Electronic Structure and Reactivity

Late First-row Transition Metals in Weak Ligand Fields – Correlating High-Spin Electronic Structure and Reactivity

A dissertation presented

by

Graham Thomas Sazama

to

The Department of Chemistry and Chemical Biology

in partial fulfillment of the requirements

for the degree of

Doctor of Philosophy

in the subject of

Chemistry

Harvard University

Cambridge, Massachusetts

May 2013

Dissertation Advisor: Professor Theodore A. Betley Graham Thomas Sazama

Late First-row Transition Metals in Weak Ligand Fields – Correlating High-Spin Electronic Structure and Reactivity

Abstract

High spin has been shown to be necessary for optimal reactivity of transition metal complexes toward the activation and functionalization of C-H bonds. This thesis presents our examination of the weak-field, tripodal, trianionic tris(pyrrolyl)ethane (tpe) ligand and its complexes.

Outer-sphere oxidation of the manganese, iron, cobalt, nickel and zinc complexes of tpe were performed by electrochemical and chemical methods. Electrochemical oxidation occurred at the same potential for each species, suggesting a ligand-based oxidation. The reaction product of chemical oxidation of iron showed oxidation of a pyrrole unit followed by H-atom abstraction to form a dichelated species. Density functional theory calculations confirm these results, and *in silico* oxidation of the complexes is entirely ligand-based. These results establish that tpe complexes are oxidized at the pyrrolide subunits in outer-sphere electron transfers, and elucidate minimal metal-ligand electronic communication.

The more reactive $[(tpe)Fe(THF)]^-$ anion exhibits rapid binding of three equivalents of *tert*-butyl isonitrile, while reaction with excess carbon monoxide induces ligand fragmentation to form a species wherein two molecules of carbon monoxide have been reductively coupled. A mechanism based on the observed isonitrile species is proposed.

The use of inner-sphere oxidant reagents allows for several stable iron (III) complexes of tpe to be isolated and characterized. Alkyl peroxides and alkyl disulfides, organic azides, and diphenyldiazomethane are all shown to oxidize iron by a single electron. Reaction with organic azides results in the formation of iron (III) amide species, likely as a result of H-atom abstraction. The weak-field of tpe creates a high propensity for forming high-spin iron (III) complexes, to the extent that diphenyldiazoalkane acts as a redox-active ligand and provides a one-electron reservoir to reveal a high-spin Fe^{3+}. Spectroscopic and computational studies were undertaken to rigorously assign the physical oxidation state of iron in all cases. Given the outer-sphere redox liability of the tpe ligand, and the capability for inner-sphere oxidation local to iron, tpe complexes of iron represent a new class of metal-ligand redox activity, wherein the metal and ligand form two separate redox reservoirs, accessible via different mechanisms.

Table Of Contents

List of Schemes

Chapter 2

Chapter 3

Chapter 4

List of Figures

Chapter 1

Chapter 2

Chapter 3

Chapter 4

List of Tables

List of Chemical Abbreviations

ACN	acetonitrile
Bn	benzyl
CHD	cyclohexadiene
dba	dibenzylideneacetone
DCM	dichloromethane
DDQ	2,3-dichoro-5,6-dicyano-1,4-benzoquinone
dpma	dipyrromethane
dpme	dipyrromethene or dipyrrin
Et	ethyl
Fc	ferrocene
Fc^+	ferrocenium
^{i}Pr or iPr	isopropyl
JohnPhos	2-di-*tert*-butylphosphinobiphenyl
Me	methyl
Mes	mesityl or 2,4,6-trimethylphenyl
OTf	trifluoromethylsulfonate or triflate
PDI	pyridine diimine, 2,6-bis[1-(2,6-diisopropylphenylimino)ethyl]pyridine
Ph	phenyl
PPTS	pyridinium *para*-toluenesulfonate
py	pyridine
TBA	tetrabutylammonium
^{t}Bu or *t*Bu	*tert*-butyl
tpe	1,1,1-tris(2-mesitylpyrrolyl)ethane
thf or THF	tetrahydrofuran
TMS	trimethylsilyl
tol	toluene
Ts	*para*-toluenesulfonyl or tosyl

List of Acronyms, Symbols and Units

•	radical
{^{1}H}	proton decoupled
^{13}C	carbon-13
^{1}H	proton
A	hyperfine coupling constant
Å	angstrom, 10^{-10} meters
avg	average
br	broad
CHN%	combustion or elemental analysis percentages for carbon, hydrogen, and nitrogen
cm^{-1}	wavenumbers or inverse centimeters
CV	cyclic voltammetry or cyclic voltammogram
D	axial zero field splitting parameter
d	doublet in NMR
D or ^{2}H	deuterium
DC	direct current
d_n	deuterated (n is the number of positions where ^{2}H replaces ^{1}H)
DPV	differential pulse voltammetry or differential pulse voltammogram
e	elementary charge, charge of a single proton or electron, 1.602×10^{-19} coulombs
E	rhombic zero field splitting parameter
e^-	electron
EPR	electron paramagnetic resonance
ESI^+	positive ion electron spray ionization
G	gauss
g	Landé g-factor (but may also refer to the anomalous gyromagnetic ratio, 2.0023)
GHz	gigahertz, 10^9 Hertz or 10^9 s^{-1}
$\boldsymbol{H}$	Hamiltonian operator
H	magnetic field
HAT	hydrogen atom transfer
HOMO	highest occupied molecular orbital
HRMS	high-resolution mass spectrometry
I	current in microamperes
IR	infrared spectroscopy (NIR denotes near infrared spectroscopy)
J	coupling constant
J_{HH}	proton–proton coupling constant
k	Boltzmann constant, 0.695 cm^{-1}/K
K	kelvin
KIE	kinetic isotope effect

LC/MS	liquid chromatography/mass spectrometry
LUMO	lowest unoccupied molecular orbital
M	molar, moles per liter
m	multiplet in NMR
m-	*meta* position on an aryl ring, indicating a 1,3 relationship
m/*z*	mass to charge ratio
MHz	megahertz, 10^6 Hertz or 10^6 s^{-1}
MLMB	metal-ligand multiple bond
mmol	millimole, 10^{-3} moles
MO	molecular orbital
mV	millivolt, 10^{-3} volts
N	Avogadro constant, 6.022×10^{23} mol^{-1}
nm	nanometer, 10^{-9} meters
NMR	nuclear magnetic resonance
o-	*ortho* position on an aryl ring, indicating a 1,2 relationship
Oe	oersted
p-	*para* position on an aryl ring, indicating a 1,4 relationship
ppm	parts per million
q	quartet in NMR
rt	room temperature
s	singlet in NMR or second
S	spin
$\boldsymbol{S}$	spin operator
sh	shoulder
SOMO	singly-occupied molecular orbital
SQUID	superconducting quantum interference device
T	tesla
t	triplet in NMR
T or T	temperature
T_c	crossover temperature
UV/Vis	ultraviolet-visible absorption spectroscopy
V	potential in mV or V
V	volt
w/*w*	mass fraction or percentage weight solute per weight solution
δ	delta, chemical shift in ppm
δ	isomer shift for ^{57}Fe Mössbauer in mm/s
ΔE_Q	quadrupole splitting for ^{57}Fe Mössbauer in mm/s
ΔH	enthalpy
ε	epsilon, extinction coefficient or molar absorptivity in $M^{-1}cm^{-1}$
η^n	eta, hapticity or the number, n, of contiguous atoms in a ligand bound to a metal
κ^n	kappa, denticity or the number, *n*, of atoms in a polydentate ligand bound to the metal
λ	lambda, wavelength in nm

μA	microampere, 10^{-6} ampere
μ_B	Bohr magneton, 9.274×10^{-21} erg/G
μ_{eff}	mu effective, effective magnetic moment in Bohr magnetons
μ^n	mu, the number, *n*, of metal atoms to which a bridging ligand is bound (default *n* = 2)
ν	frequency
χ	magnetic susceptibility
χ_M or χ_m	molar magnetic susceptibility in cm^3/mol

for Claire

Acknowledgements

I owe a great deal to many people for their assistance and patience as I worked through my PhD. The Chemistry PhD process is not for the faint of heart, but I feel that even the faintest heart could make it through given the level support and encouragement I received. Being a part of the Golden Age of the Betley Group was and still is exciting, frustrating, enlightening and enjoyable. The friends and colleagues I've had here at Harvard will undoubtedly remain friends and colleagues for the rest of my career.

I would have had nowhere to start if it weren't for the first tastes of chemistry I got. Thanks to Mr. Rhode, my high school chemistry teacher for realizing that the best way to get kids interested is to tell funny stories and light things on fire. I'll never forget the lesson on increased surface area's effect on reaction rate. A hearty thank you to the entire UW-Madison chemistry department, but especially to Tehshik Yoon for implementing a plan to make Jacobsen's catalyst as my first organometallic compound in Advanced Organic Lab; Shannon Stahl, who taught me in inorganic class, and then schooled me in the lab; to John Berry, for his support and encouragement in my first days as a teaching assistant and continuing since; to Fleming Crim for insisting we do EPR in physical chemistry lab even though the spectrum plotter was running out of markers; and last, but not least, Chris Scarborough, for his immense role in helping me become the lab chemist I am today. Without the coffee, tea, basketball, tea, and constant conversations about chemistry, I'd be nowhere near an inorganic lab today.

To my friends, Bob and Alison, who shared with Claire and me the pain and suffering of earning a PhD, and made numerous trips up from "New Brunstink" to visit. It is clear that

no matter the field, a PhD is a PhD, and you've both earned yours! To Aaron McCann for calling even though it sometimes takes me 6 months to call back, and to Chris and Sarah for making multiple Boston trips, including one very memorable Beantown proposal. And thanks to Megan and Jeremy, Nick and Shannon, Bo and Lia, and the entire BU English crew for helping me remember that there's more to life than just labwork. And thanks to the Kervin family for always making me feel smarter than I am by dunking yourselves into the jargon-filled world of chemistry. You read my papers and came to my talk and told me I did great, whether you had any idea what I was saying or not.

The Betley Group is a force to be reckoned with, and will continue to be so for a long time with Ted at the helm. Thanks to Benji, Diana and Brian; I hope they learned from me well the keys to passive-aggressively emailing the entire lab about things you want changed. To Matt, your enthusiasm is on 130% speed, and it will serve the lab, and you, well. Don't stop being yourself. Raul, you're in charge now; good luck – we'll all need it. To my cohort, Austin, Tamara and Libby: I couldn't ask to be part of a finer group of students. I am proud to graduate with you three, and excited to see what the future holds for us all. Thanks for being there to listen, chat science, and have a laugh whenever it was needed. Wherever we go from here, I know it won't quite be the same without you three there.

I owe a great deal of my scientific progress to Shao-Liang Zheng, Alison Fout, and Dave Harris, for opening their brains to me and helping advance my understanding of crystallography, synthesis and whatever the hell anisotropy is. My committee, Dick Holm and Eric Jacobsen, made me feel comfortable enough to bare my scientific soul to them, and then uncomfortable enough to know there's so much more to learn. I greatly appreciate

their honest and insightful feedback and have enjoyed the chance to discuss my work with them.

To Evan King I owe a great many things. My understanding of spectroscopy, instrumentation, the city of Cambridge, the NFL, the NBA, the Celtics, television, and how to get paid – all have been influenced or even created by your influence. Well done, sir. And to Ted Betley—I couldn't have found a better home to earn a PhD, or a better advisor to push me to learn and thrive. I look forward to seeing your name on numerous papers, reviews, grants and awards, and will be proud to have been a part of it.

To Ella, my sis – thanks for sending me much needed *Dumb and Dumber* quotations to keep things light. You can always make me laugh. To my mother and father, Alison and John, I quite literally owe my life. I have had a charmed existence thus far, and can't thank you enough for everything you've done to help me get this far. Hopefully now I can make my way back a little closer. Mom, thanks for supporting and encouraging me to keep at it when times got tough; you are an example for all of us in that regard. Dad, I'm still working on that taking initiative thing. I think I'm getting better at it.

Finally, to my wife, Claire. You set my path to inorganic chemistry in motion the day you found the Stahl group in the research catalog at Wisconsin (so this is your fault). But I could have done none of this without you. You have been there when I needed inspiration, comfort, laughter, commiseration, a trip to the beach for a lobster roll, but most of all love. Thank you so much for your support and your unending efforts to help me be happy.

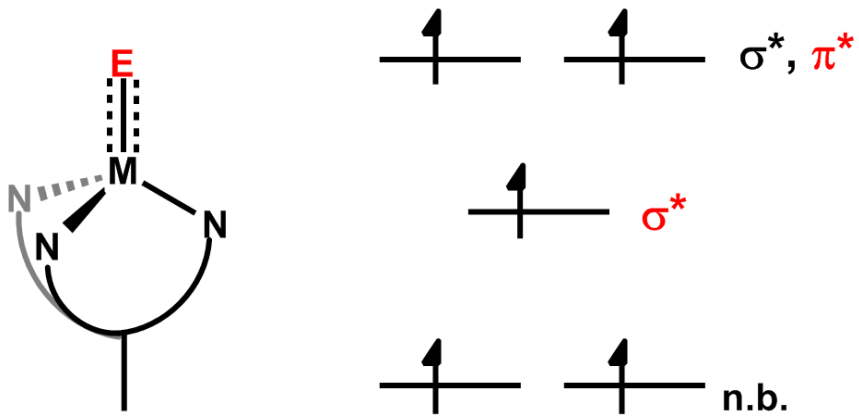

Chapter 1: Metal-Ligand Interactions in the Weak-Field/High-Spin Regime

1-1. Introduction

Chemical synthesis has long been limited to using functional groups as synthetic handles to achieve desired transformations. Functionality must either be introduced very early in a synthetic route using harsh conditions or by starting with functionalized materials extracted from fossil fuel sources. C-H bond functionalization has attracted significant interest in recent decades, as the controlled introduction of functionality directly into unactivated C-H bonds is an attractive tool for chemical synthesis.[1] Understanding the fundamental properties of systems capable of C-H functionalization is paramount to the development of efficient, selective C-H functionalization methodologies.

While the application of C-H functionalization to chemical synthesis has recently burgeoned into a topic of great interest, biological systems have encountered substrates with unsubstituted alkyl C-H bonds for millenia, and have thus evolved mechanisms for the

(1) Zalatan, D. N.; Du Bois, J. *Top. Curr. Chem.* **2010**, *292*, 347.

functionalization of unactivated substrates. A large body of literature spanning the fields of Chemistry, Biology and Physics has been amassed studying the enzymes capable of such transformations. Several enzymatic pathways for C-H functionalization exist, and a large number of them are mediated by iron metalloenzymes.[2] The enzyme Cytochrome P-450 catalyzes the hydroxylation of a large number of substrates, including the unactivated C-H bonds of alkanes. Methane monooxygenase, found in methanotrophic bacteria, is capable of activating and functionalizing a C-H bond of methane—the strongest possible aliphatic C-H bond. Because of their ability to activate and functionalize strong aliphatic C-H bonds, Cytochrome P-450 and soluble methane monooxygenase serve as exemplars for biological C-H functionalization chemistry.

To better understand the characteristics necessary to achieve a high level of reactivity and selectivity in C−H functionalization, we were prompted to explore the chemistry of coordination complexes that might allow us to address the following questions regarding enzymatic and synthetic C-H functionalization: What are the key aspects of the ligand-metal interactions? Specifically, do the ligands play an active role in the molecular redox chemistry of the complexes? What type of electronic structure do the ligands impose on the reactive species? Are the ligand field-strength and redox activity linked in some way? What role does the geometry of the ligand environment play? What ligand design principles can we learn from such systems?

(2) Lewis, J. C.; Coelho, P. S.; Arnold, F. H. *Chem. Soc. Rev.* **2011**, *40*, 2003.

1-2. Redox–active Ligands

Oxidation state is a foundational principle of inorganic chemistry. Undergraduates learn the assignment of formal oxidation states and electron counting for coordination compounds, and are taught techniques such as Mössbauer, EPR, and vibrational spectroscopies to assess the physical oxidation state of a transition metal atom. When ligands bound to a transition metal are capable of existing in multiple redox states, even as open shell species, the formal oxidation state of the metal and the physical oxidation state may not agree.[3] Modern coordination chemistry requires a more nuanced view of metal-ligand bonding, one that addresses the possibility of redox-active ligands (RAL).

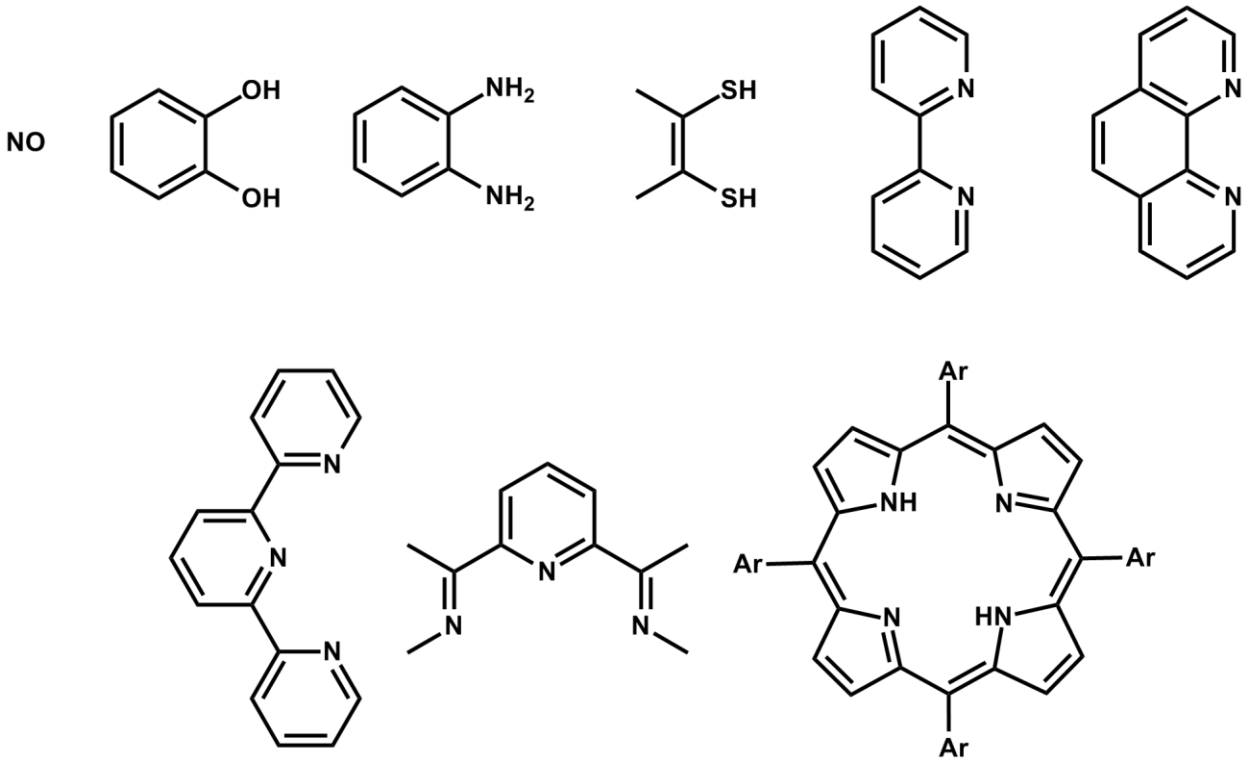

Figure 1.1. Selected examples of ligands with significant spectroscopic evidence for redox non-innocence.

(3) Chaudhuri, P.; Verani, C. N.; Bill, E.; Bothe, E.; Weyhermüller, T.; Wieghardt, K. *J. Am. Chem. Soc.* **2001**, *123*, 2213.

Inorganic chemists first described redox-active ligands in the 1960s,[4] and since then a number of ligand variations have been synthesized and studied that are stable in multiple redox states when bound to transition metals (Figure 1.1).[4e, 5] Recently, RAL have been employed in coordination complexes to extend the redox reservoir of metal complexes[6] to enable typically redox-inert transition metals to perform classic oxidative addition and reductive elimination reactions,[7] and to elicit two-electron transformations from transition metals that typically undergo one-electron processes.[8] The most commonly employed photosensitizer, $[Ru(bpy)_3]^{2+}$, owes its unique properties in part to the redox activity of its ligands.[9] Because of their implication in C-H hydroxylation by cytochrome P-450, the possible interplay between RAL and transition metals must be considered in the design of synthetic systems.

While the characteristics that predispose organic ligands to being redox-active—good energetic match between transition metal and ligand orbitals, ligand redox potentials matched with those of the metals being used, and generally large π systems with relatively

(4) (a) Schrauzer, G. N.; Mayweg, V. *J. Am. Chem. Soc.* **1962**, *84*, 3221. (b) Davison, A.; Edelstein, N.; Holm, R. H.; Maki, A. H. *Inorg. Chem.* **1963**, *2*, 1227. (c) Gray, H. B.; Williams, R.; Bernal, I.; Billig, E. *J. Am. Chem. Soc.* **1962**, *84*, 3596. (d) Billig, E.; Williams, R.; Bernal, I.; Waters, J. H.; Gray, H. B. *Inorg. Chem.* **1964**, *3*, 663. (e) Eisenberg, R.; Gray, H. B. *Inorg. Chem.* **2011**, *50*, 9741.

(5) (a) Scarborough, C. C.; Wieghardt, K. *Inorg. Chem.* **2011**, *50*, 9773. (b) Scarborough, C. C.; Lancaster, K. M.; DeBeer, S.; Weyhermüller, T.; Sproules, S.; Wieghardt, K. *Inorg. Chem.* **2012**, *51*, 3718. (c) Pierpont, C. G. *Inorg. Chem.* **2011**, *50*, 9766. (d) England, J.; Scarborough, C. C.; Weyhermüller, T.; Sproules, S.; Wieghardt, K. *Eur. J. Inorg. Chem.* **2012**, *2012*, 4605. (e) Bart, S. C.; Chłopek, K.; Bill, E.; Bouwkamp, M. W.; Lobkovsky, E.; Neese, F.; Wieghardt, K.; Chirik, P. J. *J. Am. Chem. Soc.* **2006**, *128*, 13901.

(6) (a) Pierpont, C. G. *Inorg. Chem.* **2011**, *50*, 9766. (b) England, J.; Scarborough, C. C.; Weyhermüller, T.; Sproules, S.; Wieghardt, K. *Chem. Eur. J.* **2012**, *2012*, 4605.

(7) (a) Zarkesh, R. A; Ziller, J. W.; Heyduk, A. F. *Angew. Chem. Int. Ed.* **2008**, *47*, 4715. (b) Blackmore, K. J.; Ziller, J. W.; Heyduk, A. F. *Inorg. Chem.* **2005**, *44*, 5559. (c) Stanciu, C.; Jones, M. E.; Fanwick, P. E.; Abu-Omar, M. M. *J. Am. Chem. Soc.* **2007**, *129*, 12400. (d)

(8) (a) Tondreau, A. M.; Atienza, C. C. H.; Weller, K. J.; Nye, S. A; Lewis, K. M.; Delis, J. G. P.; Chirik, P. J. *Science,* **2012**, *335*, 567. (b) Bouwkamp, M. W.; Bowman, A. C.; Lobkovsky, E.; Chirik, P. J. *J. Am. Chem. Soc.* **2006**, *128*, 13340.

(9) Hendrickson, D. N.; Pierpont, C. G. *Top. Curr. Chem.* **2004**, *234*, 63.

strong metal-ligand π interactions[10]—are relatively well-understood. However, the properties necessary for transition metal systems to confer redox activity onto traditionally non-redox-active ligands remain somewhat unexplored.[11,12] Utilizing the inherent stability of specific electronic configurations of transition metals in particular ligand fields to influence organic ligands to become redox active is a promising approach for uncovering novel reactivity.

1-3. Group Transfer from High-Spin Complexes – The Weak-field Ligand Effect

Generally speaking, high-spin complexes are far more favorable for complexes of 3d transition metals as opposed to their 4d and 5d counterparts.[13] The frontier orbitals of third row transition metals (3d) are lower in energy than 4d and 5d orbitals, and thus closer to the nucleus with less spatial extent into the coordination sphere. As a result, third row metals form weaker interactions with ligand orbitals (such as those of C, N, O, and halides). Depending on the strength of the ligand field, 3d transition metals are able to exhibit both high- and low-spin states, with weak-field ligands favoring high spin. Because metalloenzymes are built of peptides, they typically employ weak-field ligands such as carboxylate, histidine, water, hydroxo, amine and sulfide. In addition, metalloenzymes typically only employ earth-abundant, bioavailable transition metals, which are far more

(10) (a) Heyduk, A. F.; Zarkesh, R. A; Nguyen, A. I. *Inorg. Chem.* **2011**, *50*, 9849. (b) Pierpont, C. G.; Lange, C. W. *Prog. Inorg. Chem.* **1994**, *41*, 331. (c) Lever, A. B. P. *Coord. Chem. Rev.* **2010**, *254*, 1397. (d) Evangelio, E.; Ruiz-Molina, D. *Eur. J. Inorg. Chem.* **2005**, *2005*, 2957.

(11) Scarborough, C. C.; Sproules, S.; Doonan, C. J.; Hagen, K. S.; Weyhermüller, T.; Wieghardt, K. *Inorg. Chem.* **2012**, *51*, 6969.

(12) Dzik, W. I.; Zhang, X. P.; de Bruin, B. *Inorg. Chem.* **2011**, *50*, 9896.

(13) Miessler, G. L.; Tarr, D. A. *Inorganic Chemistry (4th Edition)*; Prentice Hall, 2010.

likely to be 3d transition metals. Thus, metalloenzymes typically contain high-spin metal centers.

Group transfer reagents—such as iodosobenzene or amine N-oxides for oxo transfer, and organic azides for nitrene transfer—typically react and form the appropriate transferred group on the transition metal species. The group transfer fragment is inherently a strong-field ligand: it generally participates significantly in π-bonding, and consequently forms a shorter metal-ligand interaction than a weaker field ligand. Shorter metal-ligand bonds will have greater orbital overlap, so the group transfer fragment will be a strong σ-donor.

Reaction of group transfer reagents with 3d or 4d/5d transition metals bound to strong-field ancillary ligands produces complexes with strong metal-ligand multiple-bonds.[14] The strong field ancillary ligands lead to large frontier orbital energy differences (d-orbital splittings), and thus low-spin complexes. With the proper d-electron count, low-spin complexes will fill only non-bonding orbitals, leaving the σ* and π* orbitals empty and allowing for triple bond character between the group transfer fragment and the metal. These multiply bonded species have proven to be remarkably stable in many cases.[14a,b,f]

When the transition metal resides in a weak-field ancillary ligand environment, however, group transfer complexes can be high-spin in spite of the strong-field nature of the group transfer fragment. In order to maintain metal-ligand bonding interactions in the high-spin regime, antibonding orbitals must not be fully filled. The geometry of the complexes becomes an important factor in determining the d-orbital splitting, spin-state, and

(14) (a) Mayer, J. M. *Acc. Chem. Res.* **1998**, *31*, 441. (b) Saouma, C. T.; Peters, J. C. *Coord. Chem. Rev.* **2011**, *255*, 920. (c) Mehn, M. P.; Peters, J. C. *J. Inorg. Biochem.* **2006**, *100*, 634. (d) Mehn, M. P.; Brown, S. D.; Jenkins, D. M.; Peters, J. C.; Que, L. *Inorg. Chem.* **2006**, *45*, 7417. (e) Hu, X.; Meyer, K. *J. Am. Chem. Soc.* **2004**, *126*, 16322. (f) Spaltenstein, E.; Conry, R. R.; Critchlow, S. C.; Mayer, J. M. *J. Am. Chem. Soc.* **1989**, *111*, 8741.

maximum d-electron count—and by extension the bond orders and predicted stability—of complexes with weak-field ancillary ligands.

The effect of geometry on the frontier orbitals is summarized in Figure 1.2. In the weak-field limit, 4-coordinate species are attractive targets for synthesis, as their low overall d-orbital splitting (relative to 5- and 6-coordinate) provides the highest likelihood of fully high-spin configurations. The higher coordination number species are more highly split and thus more likely to pair electrons in lower lying d-orbitals, which would lead to intermediate- or low-spin compounds.

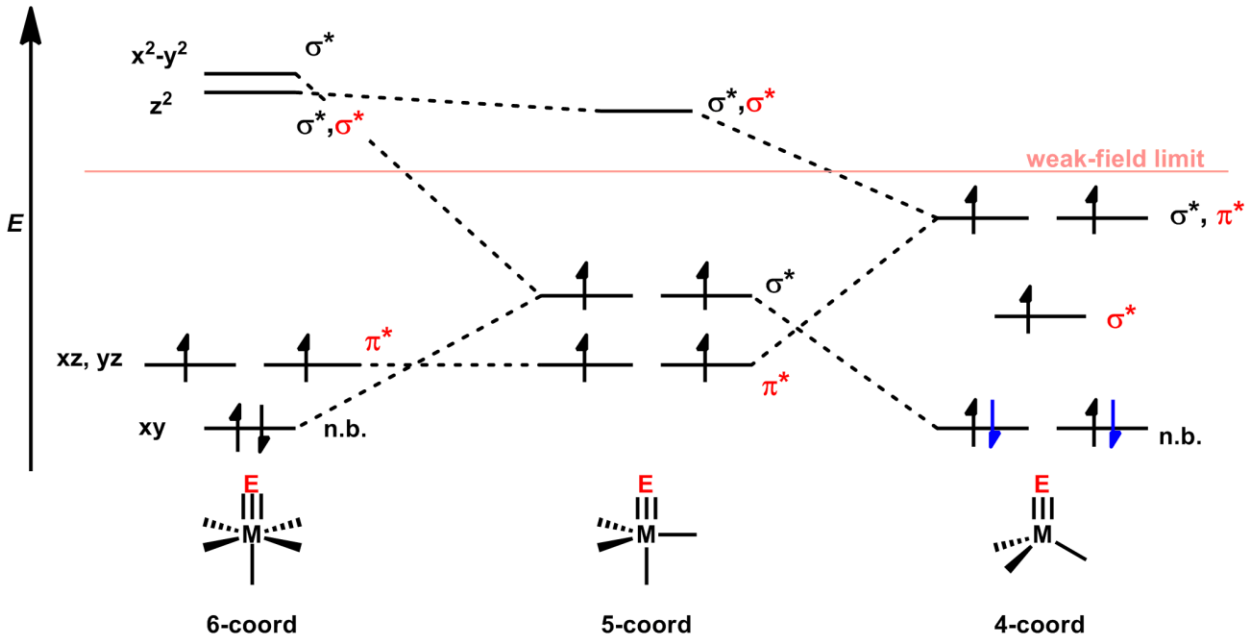

Figure 1.2. Effect of coordination number and local geometry on the d-orbital splitting of metal-group transfer complexes. E represents a generic group transfer fragment. The red orbital designations (e.g. σ*, π*) represent M-E interactions, and the black designations represent metal-ancillary ligand interactions. Electron populations represent the maximum number of d electrons to maintain metal-ligand interactions, with blue electrons representing additional acceptable electron population. The weak-field limit line represents the energy at which electron pairing becomes less energetically costly than population of d-orbitals.

1-4. Macrocyclic vs. Non-macrocyclic Pyrrole Ligands

Pyrrole-based ligands were chosen as candidates for the formation of high-spin metal complexes due to their weak σ- and π-basicity. A comparison of pyrrole and substituted pyrroles to other anionic ligands has demonstrated that they are similar in donor strength to carboxylates, and much less donating than alkoxides and amides.[15] Ligands based on pyrroles stand to be premier candidates for stabilizing maximally high spin complexes due to their weak ligand field.

Several macrocyclic tetraporphyrin ligands differing in the pyrrole linking groups—and thus differing in the extent of aromaticity and amount of anionic charge in their closed-shell forms—have been synthesized and their complexes well-studied (Figure 1.3).[16] Porphyrin is a tetrapyrrole ligand wherein all four pyrroles are linked by methine carbons, and as such is fully aromatic and dianionic when bound to a transition metal.. Porphyrins are ubiquitous in biological heme enzymes, and synthetically accessible forms exist that differ from biological porpyhrin only in their periphery and not at the metal binding sites. Porphyrinogen, a tetrapyrrole macrocycle lacking conjugation between pyrroles has also been reported, and is tetraanionic bound to metal. Corrole, a tetrapyrrole macrocycle which has one fewer meso carbon and two directly fused pyrroles, lies between porpyhrin and porpyhrinogen, binding as a trianionic tetradentate ligand.

(15) DiFranco, S. A.; Maciulis, N. A.; Staples, R. J.; Batrice, R. J.; Odom, A. L. *Inorg. Chem.* **2012**, *51*, 1187.

(16) Porphyrins: (a) Collman, J. P.; Arnold, H. J.; Arnold, J. *Acc. Chem. Res.* **1993**, *26*, 586. (b) Brothers, P. J.; Collman, J. P. *Accounts of Chemical Research* **1986**, *19*, 209. (c) Groves, J. T.; Nemo, T. E. *J. Am. Chem. Soc.* **1983**, *105*, 6243. Porphyrinogens: (a) Bachmann, J.; Nocera, D. G. *J. Am. Chem. Soc.* **2005**, *127*, 4730. (b) Bachmann, J.; Nocera, D. G. *J. Am. Chem. Soc.* **2004**, *126*, 2829. Corroles: (a) Ye, S.; Tuttle, T.; Bill, E.; Simkhovich, L.; Gross, Z.; Thiel, W.; Neese, F. *Chem. Eur. J.* **2008**, *14*, 10839. (b) Simkhovich, L.; Goldberg, I.; Gross, Z. *Inorg. Chem.* **2002**, *41*, 5433. Porphyrinoids: Filatov, M. a.; Cheprakov, A. V.; Beletskaya, I. P. *Eur. J. Org. Chem.* **2007**, 3468.

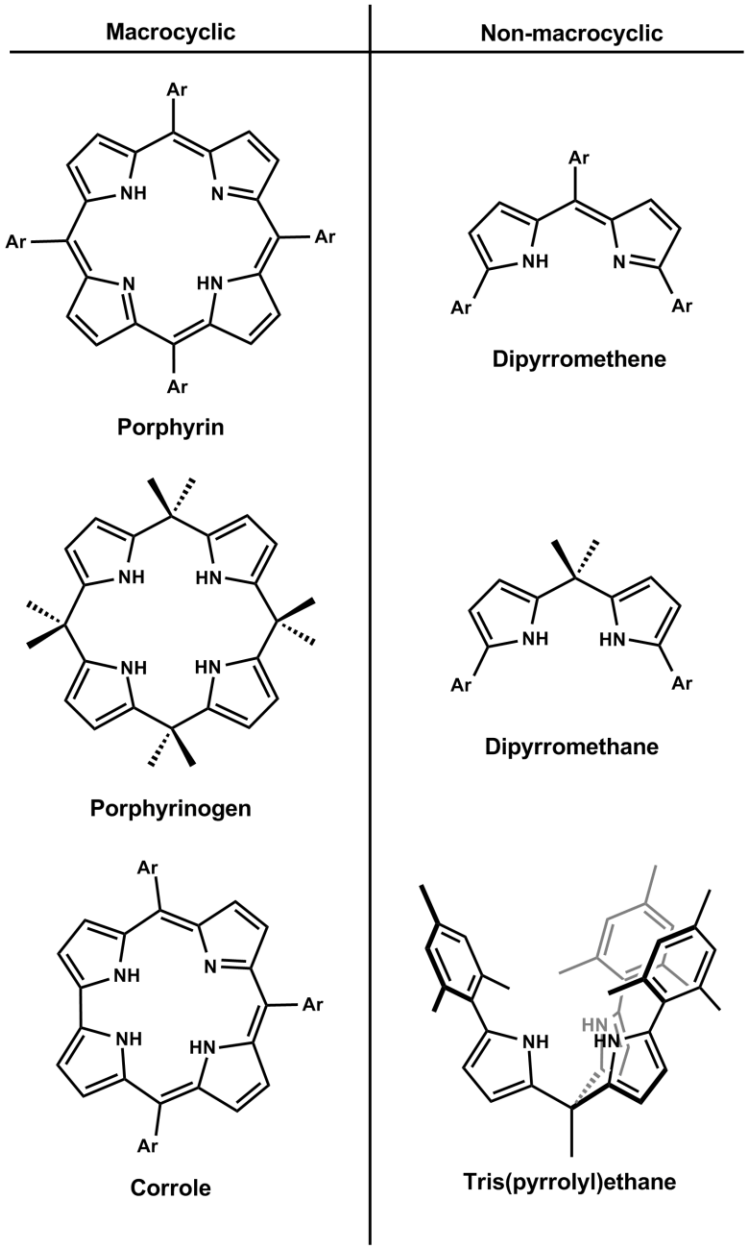

Figure 1.3. Selected macrocyclic multipyrrole ligands and proposed non-macrocyclic derivatives.

The syntheses of macrocyclic pyrrole ligands are non-trivial: pyrrole is condensed with the appropriate aldehyde in an oligomerziation reaction, and oxidations are carried out to aromatize the compound in the case of porphyrin.[17,18] Oligomerizations are generally

(17) Koszarna, B.; Gryko, D. T. *J. Org. Chem.* **2006**, *71*, 3707.

difficult to control, and as such large amounts of pyrrole starting material must be oligomerized to form useful quantities of porpyhrin and porphyrinoid ligands. This oligomerization process requires dilute reaction conditions, and thus large quantities of solvent for scale preparations, and even under these conditions significant quantities of undesired side products are produced. Further purification decreases yields significantly, as these multidentate ligands are liable to adhere to silica gel during column chromatography.[18b] Porphyrins are also restricted to tetradentate equatorial binding and are modular only at the outer (pyrrole 3 and 4, and meso) carbons, which allows only limited control over the steric environment closer to the coordination sphere.

Our group and others[19] have targeted the synthesis and application of multipyrrole ligands with greatly simplified synthesis, presented in Figure 1.3. Acid-catalyzed condensation of pyrroles—which can be variably subsituted in the 2 position—with the appropriate methine or methylene precursor yields the dipyrromethane or tripyrroethane materials in good yields. The dipyrromethane can be further oxidized to the dipyrromethene using DDQ as an oxidant. Using these methods, multigram quantities of di- and tri-pyrrole ligands are readily accessible, with modularity of the 2-substitution allowing for fine control of sterics.

(18) (a) Adler, A. D.; Longo, F. R.; Finarelli, J. D.; Goldmacher, J.; Assour, J.; Korsakoff, L. *J. Org. Chem.* **1967**, *32*, 476. (b) Lindsey, J. S.; Schreiman, I. C.; Hsu, H. C.; Kearney, P. C.; Marguerettaz, A. M. *J. Org. Chem.* **1987**, *52*, 827.

(19) (a) Majumder, S.; Odom, A. L. *Organometallics* **2008**, *27*, 1174. (b) Reid, S. D.; Wilson, C.; Blake, A. J.; Love, J. B. *Dalton Trans.* **2010**, *39*, 418. (c) Novak, A.; Blake, A. J.; Wilson, C.; Love, J. B. *Chem. Comm.,* **2002**, *330*, 2796.

1-5. Aliphatic C-H Hydroxylation by Cytochrome P-450 Enzymes

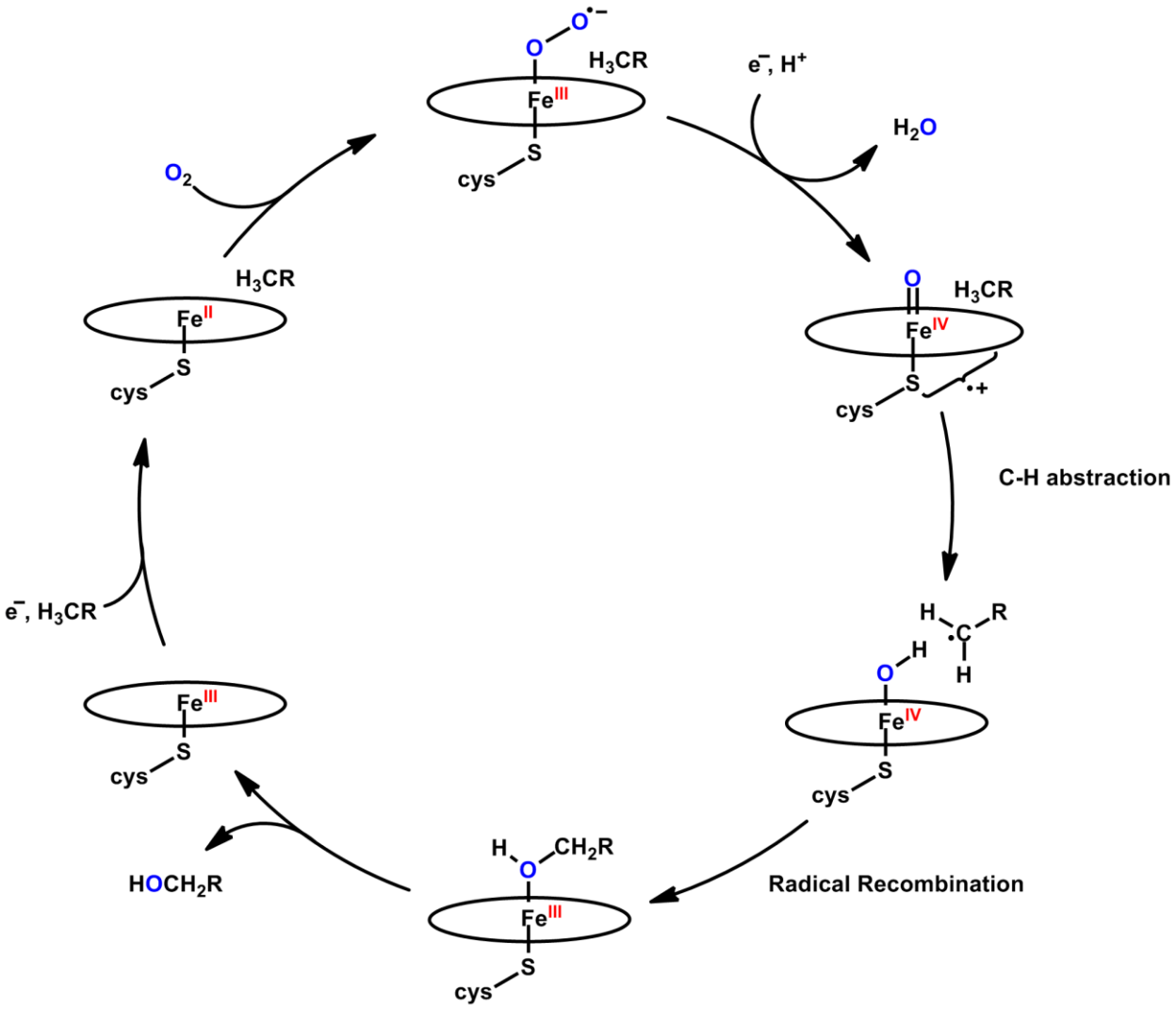

Figure 1.4. Proposed mechanism for the C-H hydroxylation of aliphatic substrates by cytochrome P-450, using dioxygen as a terminal oxidant.

Discovered in 1958,[20] Cytochrome P-450 is a ubiquitous heme-containing metalloenzyme capable of catalyzing a very large number of oxidative reactions,[21] including the functionalization of unactivated aliphatic C-H bonds. The catalytic cycle of the C-H

(20) (a) Garfinkel, D. *Arch. Biochem. Biophys.* **1958**, *77*, 493. (b) Klingenberg, M. *Arch. Biochem. Biophys.* **2003**, *409*, 2. (c) Sato, R.; Omura, T. *J. Biol. Chem.* **1964**, *239*, 2370.

(21) Sono, M.; Roach, M. P.; Coulter, E. D.; Dawson, J. H. *Chem. Rev.* **1996**, *96*, 2841.

functionalization pathway of P-450 has been studied heavily since the discovery that it oxidizes aliphatic C-H bonds in 1963,[22] and a current proposed mechanism, highlighting the intermediates of the C-H functionalization steps, is shown in **Figure 1.4**.[21,23]

The active species of P-450, known as "compound I" (Figure 1.5, A), is formed after oxidation of the resting state by a molecule of dioxygen. Compound I is an intermediate-spin heme ferryl species (Fe^{IV}-oxo) antiferromagnetically coupled to a delocalized ligand based radical present on the porpyhrin and proximal cysteine thiolate ligands.[24] The exact location of the radical cation is a matter of considerable debate, varying with particular enzymes and characterization techniques.[2,25,26] Regardless of where the radical cation resides, it is crucial for the reactivity of the enzyme. The ligand-borne radical accounts for one oxidizing equivalent, alleviating the oxidative burden borne by iron but still extending the overall oxidative capacity of the enzyme active site. Additionally, since the electron acquired upon H-atom abstraction fills the hole present on the ligand instead of populating one of the Fe-O π* orbitals, the spin density and bond strength of the Fe-O π bond is maintained through the abstraction process. The persistent radical density on the Fe-O π bond is critical to the radical rebound mechanism, as recombination with the transient

(22) Estabrook, R. W.; Cooper, D. Y.; Rosenthal, O. *Biochem. Z.* **1963**, *338*, 741.
(23) Groves, J. T. *J. Chem. Ed.* **1985**, *62*, 928.
(24) Rittle, J.; Green, M. T. *Science,* **2010**, *330*, 933.
(25) (a) Kim, S. H.; Perera, R.; Hager, L. P.; Dawson, J. H.; Hoffman, B. M. *J. Am. Chem. Soc.* **2006**, *128*, 5598. (b) Hocking, R. K.; Wasinger, E. C.; Yan, Y.-L.; Degroot, F. M. F.; Walker, F. A.; Hodgson, K. O.; Hedman, B.; Solomon, E. I. *J. Am. Chem. Soc.* **2007**, *129*, 113.
(26) Other heme iron enzymes (including cytochrome c peroxidase and ovine prostaglandin endoperoxide synthase-1) that become highly oxidized in their catalytic cycles also feature ligand based radicals on the proximal ligand or on more distant protein residues. See Stubbe, J.; van Der Donk, W. A. *Chem. Rev.* **1998**, *98*,705 and references therein.

alkyl radical species is then essentially barrierless, in comparison to the much higher barrier encountered when a spin-state crossing is necessary.[27]

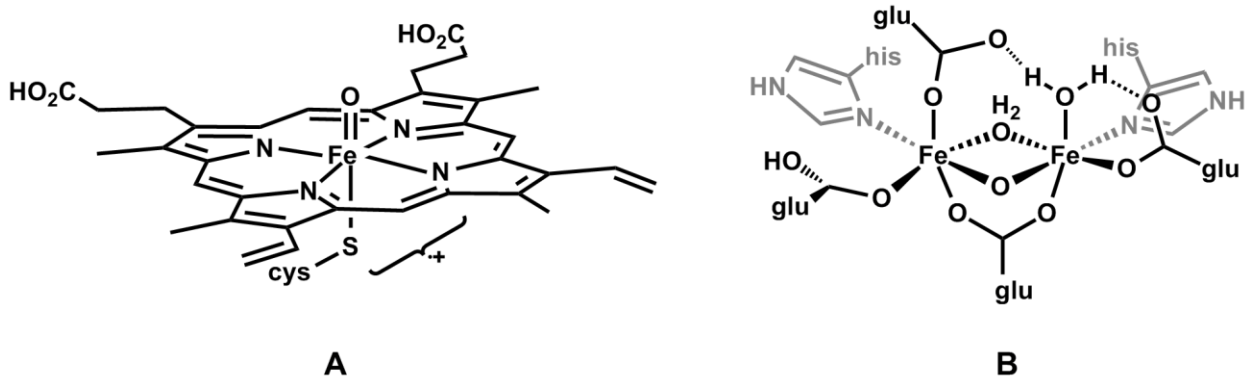

Figure 1.5. Active sites of metalloproteins Cytochrome P-450 (A) and soluble methane monooxygenase (sMMO, B).

1-6. Insight into C-H Abstraction from Soluble Methane Monooxygenase and a Synthetic Mimic

Soluble methane monooxygenase (sMMO) is a diiron hydroxylase enzyme that has been the subject of a barrage of spectroscopic, mechanistic, and computational studies.[2,28] The proposed active species, dubbed "intermediate Q" (Figure 1.5, B), has been proposed to be a diiron (IV) bis-μ-oxo diamond core species, based on Mossbauer and EXAFS data.[29] The Mössbauer spectroscopic parameters reveal that the diiron (IV) diamond core species is diamagnetic, due to anti-ferromagnetic coupling of two intermediate- or high-spin iron (IV) centers.[30] It is important to note that these data are recorded at cryogenic temperatures,

(27) Shaik, S.; Cohen, S.; Wang, Y.; Chen, H.; Kumar, D.; Thiel, W. *Chem. Rev.* **2010,** *110*, 949.
(28) (a) Baik, M.-H.; Newcomb, M.; Friesner, R. a; Lippard, S. J. *Chem. Rev.* **2003**, *103*, 2385. (b) Sazinsky, M. H.; Lippard, S. J. *Acc. Chem. Res.* **2006**, *39*, 558. (c) Tshuva, E. Y.; Lippard, S. J. *Chem. Rev.* **2004**, *104*, 987. (d) Merkx, M.; Kopp, D. a.; Sazinsky, M. H.; Blazyk, J. L.; Müller, J.; Lippard, S. J. *Angew. Chem. Int. Ed.* **2001**, *40*, 2782.
(29) Shu, L.; Nesheim, J. C.; Kaufmann, K.; Münck, E.; Lipscomb, J. D.; Que, L. *Science* **1997**, *275*, 515.
(30) Lee, S. K.; Fox, B. G.; Froland, W. A.; Lipscomb, J. D.; Münck, E. *J. Am. Chem. Soc.* **1993**, *115*, 6450.

and thus likely represent more closely the spin ground-states of intermediate Q and not necessarily the effective spin state of the active site at biologically relevant conditions.

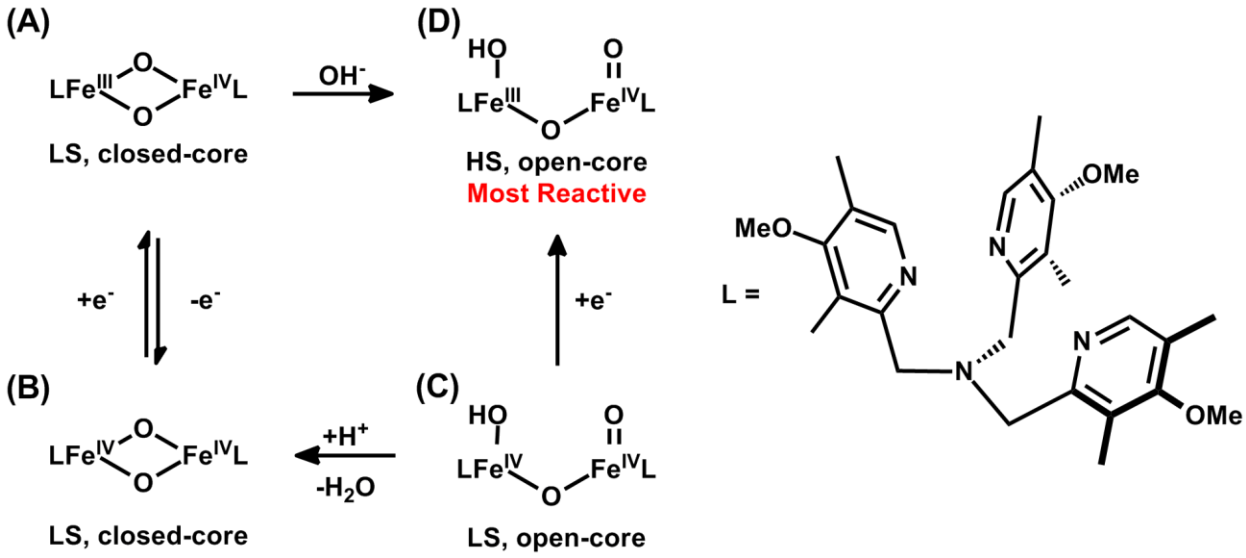

Figure 1.6. Series of four sMMO mimics synthesized by Que, et al,[31] based on the substituted tris(pyridylmethyl)amine ligand. Species A, B, and C all feature low-spin iron (Fe^{IV} is $S = 1$; Fe^{III} is $S = 1/2$), whereas species D contains a high-spin $S = 5/2$ Fe^{III} antiferromagnetically coupled to a high-spin $S = 2$ Fe^{IV}.

Model complexes of sMMO have brought to light some important discrepancies in the proposed bis-μ-oxo diiron (IV) active site and its reactivity.[31,32] A synthetic model of the diiron (IV) diamond-core (Figure 1.6, B) is capable of abstracting C-H bonds from 9,10-dihydroanthracene, a good H-atom donor, but abstraction from stronger C-H bonds more closely resembling sMMO substrates was not reported.[33] Indeed, it has been shown that the closed diamond-core species is far less reactive than an opened-core

(31) (a) Xue, G.; De Hont, R.; Münck, E.; Que, L. *Nature Chem.* **2010**, *2*, 400.

(32) (a) Foster, T. L.; Caradonna, J. P. *J. Am. Chem. Soc.* **2003**, *125*, 3678. (b) Stassinopoulos, A.; Caradonna, J. P. *J. Am. Chem. Soc.* **1990**, *112*, 7071. (c) Stassinopoulos, A.; Schulte, G.; Papaefthymiou, G. C.; Caradonna, J. P. *J. Am. Chem. Soc.* **1991**, *113*, 8686. (d) Mukerjee, S.; Stassinopoulos, A.; Caradonna, J. P. *J. Am. Chem. Soc.* **1997**, *119*, 8097.

(33) Xue, G.; Wang, D.; De Hont, R.; Fiedler, A. T.; Shan, X.; Münck, E.; Que, L. *Proc. Nat. Acad. Sci.* **2007**, *104*, 20713.

([HO−Fe^{IV}−O−Fe^{IV}=O]$^{3+}$) complex (Figure 1.6, C).[34] However, an even larger discrepancy in H-atom abstraction rate was observed upon reduction of the open-core diiron (IV) species. Although the core is structurally analogous, the reduced open-core diiron (III/IV) species (Figure 1.6, D) undergoes H-atom abstraction 1000 times faster than the diiron (IV/IV) species. Additionally, while both species are competent to abstract H-atoms from THF, only the III/IV compound is capable of doing so at low temperature. This result is initially counterintuitive, as one would expect the more oxidized species to undergo abstraction more readily. Since these two species differ only in the iron oxidation states and the overall spin state, the enhanced reactivity of the less oxidized species must be attributed to the higher spin state. Indeed, theoretical models of the protein active site have described a highly dissymmetric diamond core for compound Q in high-spin configurations, including one Fe^{III}-Fe^{IV} μ-oxyl radical site,[35] and another that approaches the valence localized Fe^{V}-Fe^{III} resonance form.[36] In all of these proposed models, the high-spin of sMMO compound Q is essential for maximal reactivity.

1-7. Nitrene Group Transfer from Iron Dipyrromethenes

Nitrene group transfer to unactivated C-H bonds represents an abiological variation of oxo transfer, but can be directly compared to the oxo-transfer reactivity due to the valence isoelectronicity of nitrenes and oxos. Nitrenes and oxos share similar electron configurations (namely 2^- formal charges and two accessible π–symmetry lone pairs), with the nitrene featuring an N-C bond in place of a lone pair found in the oxo group. Recently

(34) Xue, G.; Fiedler, A. T.; Martinho, M.; Münck, E.; Que, L. *Proc. Nat. Acad. Sci.* **2008**, *105*, 20615.
(35) Siegbahn, P. E. M. *J. Biol. Inorg. Chem.* **2001**, *6*, 27.
(36) Rinaldo, D.; Philipp, D. M.; Lippard, S. J.; Friesner, R. A. *J. Am. Chem. Soc.* **2007**, *129*, 3135.

our group has developed a methodology for C-H bond functionalization via nitrene group transfer from organic azides, mediated by iron complexes of substituted dipyrromethenes (dpme).[37,38] A kinetic isotope effect of 12.8 for the amination of toluene suggests that H-atom abstraction contributes to the rate determining step, which would then be followed by radical recombination. Similar KIEs were observed for hydroxylation by P-450, contributing to the development of the radical rebound mechanism.[39] Our methodology is made more compelling by our ability to stabilize and characterize the reactive intermediate in the group-transfer process (**Figure 1.7**, [(^{Ar}dpme)FeCl($NC_6H_4{}^tBu$)]), which we have identified as a ferric iron antiferromagnetically coupled to an iminyl radical monoanionic ligand (**Figure 1.7**, b and c).

(37) King, E. R.; Hennessy, E. T.; Betley, T. A. *J. Am. Chem. Soc.* **2011**, *133*, 4917.
(38) Hennessy, E. T.; Betley, T. A. *Science* **2013**, *340*, 591.
(39) Groves, J. T.; McClusky, G. A.; White, R. E.; Coon, M. J. *Biochem. Biophys. Res. Comm.* **1978**, *81*, 154.

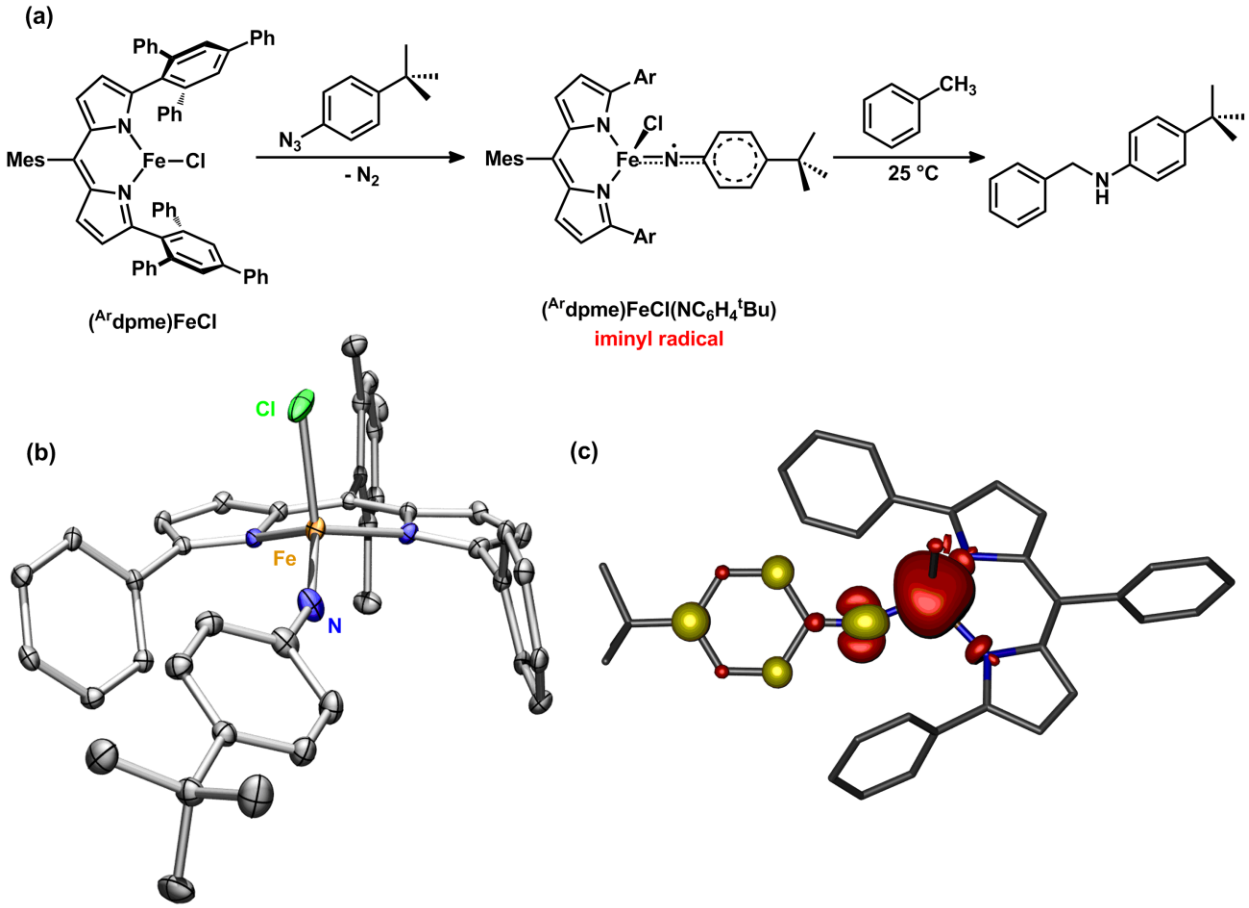

Figure 1.7. (a) Scheme depicting the reaction of a substituted dipyrromethene iron complex with aryl azide to produce an iminyl radical species and subsequent C-H bond amination of toluene. (b) ORTEP of crystal structure obtained of the iminyl radical intermediate, and (c) density functional theory spin polarization density plot obtained from a single point calculation of the iminyl radical intermediate species. Net alpha spin appears in red, and net beta spin yellow, clearly indicating the presence of an imide-localized beta electron. From reference 37.

Comparison of the electronic structure of the active iron iminyl radical species to the electronic structures proposed for the P-450 and sMMO active sites highlights some key commonalities. In all three cases, the ligand sphere is made up of weak-field ligands only, and the charge of the resting state ferrous complexes is balanced by anions. The resulting active sites all feature unpaired electron density on the iron center (low-spin , S = 1, in the case of P-450, and high-spin for sMMO and [(^{Ar}dpme)FeCl(NAr)]), which is distributed

along the metal-ligand bond of the transferred group. Finally, both P-450 compound I and the dipyrromethene active species feature organic ligands that are open-shell. P-450 features a delocalized radical cation on the porpyhrin and sulfur, whereas the dipyrromethene system contains an iminyl radical (as opposed to a closed shell imido ligand).

Although all three complexes are competent for C-H functionalization, several important differences deserve mention. All three complexes feature transition metals in different geometries: sMMO is a diiron unit, featuring two locally octahedral iron atoms bridged by two oxo ligands; P-450 is octahedral at iron; and the dipyrromethene is pseudo tetrahedral/trigonal monopyramidal. The different geometries of the active species affect the electronic structure of the frontier d-orbitals of these complexes, so they must have different d-orbital populations to maintain reactivity (see Figure 1.2). Even so, after reaction all three species still have radical character present at the Fe-E π-bond, reducing the barrier to recombination with the transient alkyl radical. The active sites of the two metalloenzymes both contain iron in the +4 oxidation state, whereas the iron in the diyprromethene complex is only trivalent, a factor that can be attributed to the geometry of the complexes (*vide supra*). Although both P-450 and the dipyrrin system feature open-shell organic ligands, the localization of that radical appears on fragments that serve different functions. P-450 has a radical equivalent on one of the ancillary ligands, whereas the iminyl radical antiferromagnetically coupled to the iron is both the actively transferred group as well as the radical reservoir.

1-8. Conspectus and Chapter Summaries

I have described the active species of several systems which introduce functionality into unactivated C-H bonds. Cytochrome P-450 and sMMO, their model complexes, and an iron dipyrromethene system developed by our group share a number of properties that have been proposed to be important for metal-mediated functionalization of C-H bonds. These properties include: 1) the oxidation state and geometry of the transition metal or, in the case of redox-active ligands, of the molecule as a whole; 2) the weak-field ligand environment, and thus the spin-state of the complex; 3) the metal-ligand multiple bond-like character between the metal and the transferred group. This thesis seeks to explore these factors in the context of a weak-field, tripodal, trianionic donor set.

Chapter 2 introduces the tris(pyrrolyl)ethane (tpe) ligand and probes the outer-sphere electron transfer chemistry exhibited by a series of its transition metal complexes. The manganese, iron, cobalt, nickel and zinc complexes are four coordinate anionic complexes, with pyridine occupying the fourth coordination site and an outer-sphere lithium countercation. All five metal complexes exhibit coincident first oxidation waves in cyclic voltammetry and differential pulse voltammetry experiments, suggesting no transition metal influence on the first oxidation potential. Chemical oxidation of the iron complex with the outer-sphere oxidant ferrocenium hexafluorophosphate results in the formation of a bis-ligated species, wherein one pyrrolide subunit of the tpe ligand has abstracted an adventitious H-atom to form a neutral pyrrole. The immediate product of oxidation can be observed by EPR spectroscopy of the zinc complex oxidized at low temperature, and displays a signal indicative of an organic, tpe-ligand based radical. Density functional

theory calculations confirm these results, and *in silico* oxidation of the complexes is entirely ligand-based. The results presented in chapter 2 establish how very little influence the tpe ligand has on bound transition metals.

Chapter 3 describes the metal-redox neutral chemistry of a more reactive variant of the tpe complexes, where pyridine has been replaced with a more labile THF molecule. The $[(tpe)Fe(THF)]^-$ anion exhibits rapid binding of three equivalents of *tert*-butyl isonitrile. Inspection of the crystal structure of the obtained product reveals rearrangement of the mesityl flanking units to accommodate the incoming isonitriles, inducing tautomerization of one pyrrolide unit from *N*-coordination to *C*-coordination to iron. Reaction with carbon monoxide induces ligand fragmentation to form a species wherein two molecules of carbon monoxide have been reductively coupled. The nucleophile in this reaction proves to be one pyrrolide subunit of the tpe ligand, and a mechanism based on the observed isonitrile species is proposed. The uncommon reduction of carbon monoxide presented speaks to the strong reducing power available in the tpe ligand, which, in view of the results presented in chapter 2, highlights how little metal-ligand communication is present in tpe complexes.

In spite of the outer-sphere oxidative liability observed in chapter 2, results acquired concomitantly urged us to examine the oxidative chemistry of tpe iron complexes. **Chapter 4** presents several species that are products of inner-sphere oxidation reactions. By choosing the appropriate oxidants—namely, those that bind to the transition metal prior to oxidation—several stable iron (III) complexes of tpe were isolated and characterized. Dialkyl peroxides and dialkyl disulfides form the corresponding alkoxide and alkyl sulfide tpe iron complexes. Reaction with organic azides, which are typically two-electron

oxidants, results in the formation of iron (III) amide species, likely through formation of an imido or iminyl radical species and subsequent H-atom abstraction. Finally, reaction with diphenyldiazomethane results in a reversible one-electron oxidation of iron. Careful spectroscopic and computational studies were undertaken to rigorously assign the physical oxidation state of iron in all cases. The reactivity presented in Chapter 4 exhibits the high propensity for forming high-spin iron (III) complexes in such a weak field ligand environment, to the extent that diphenyldiazoalkane, typically a carbene delivery agent, acts as a redox-active ligand and provides a one-electron reservoir to reveal a high-spin Fe^{3+}.

In relation to the highly-reactive complexes discussed in this introduction, the work presented here shows that high-valent transition metal species are not required for H-atom abstraction reactions. Indeed, if group transfer fragments can be deprived of enough electron density by the transition metal, that fragment itself can become capable of H-atom abstraction. A method of creating such electronic dissymmetry is to harness the inherent preference of a transition metal in a given geometry and oxidation state toward a particular spin state. Group transfer leads to metal-ligand multiply-bonded species in low-spin cases. In high-spin cases, spin density along metal-ligand bond vectors creates reactive fragments, and furthermore allows for recombination given the appropriate steric environment. This research highlights the potential of weak-field ligands as platforms for reactive high-spin complexes.

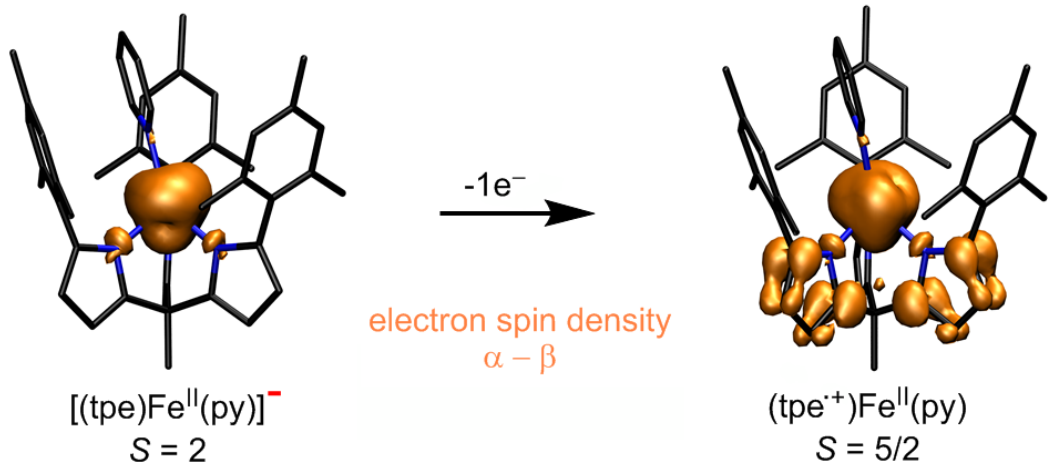

Chapter 2: Ligand-Centered Redox Activity: Redox Properties of 3*d* Transition Metal Ions Ligated by the Weak-Field Tris(Pyrrolyl)Ethane Trianion[1]

2-1. Introduction

Cooperative molecular redox comprised of metal and ligand contributions requires both energetic and angular overlap between the frontier ligand-based π orbitals and the metal-based *d*-orbitals.[2] Pyrrole-based, oligomeric ligand platforms are an important subclass of

(1) This chapter was adapted with permission from Sazama, G. T.; Betley, T. A. *Inorg. Chem.* **2010**, *49*, 2512–24. Copyright 2010 American Chemical Society.

(2) Common redox active ligands: *Catecholates*: (a) Haga, M.; Dodsworth, E. S.; Lever, A. B. *Inorg. Chem.* **1986**, *25*, 447-453. (b) Masui, H.; Lever, A. B. P.; Auburn, P. R. *Inorg. Chem.* **1991**, *30*, 2402-2410. *Dithiolates*: (c) Schrauzer, G. N.; Mayweg, V. *J. Am. Chem. Soc.* **1962**, *84*, 3221. (d) Stiefel, E. I.; Waters, J. H.; Billig, E.; Gray, H. B. *J. Am. Chem. Soc.* **1965**, *87*, 3016-3017. *Amido-phenolates*: (e) Chaudhuri, P.; Verani, C. N.; Bill, E.; Bothe, E.; Weyhermüller, T.; Wieghardt, K. *J. Am. Chem. Soc.* **2001**, *123*, 2213-2223. (f) Herebian, D.; Bothe, E.; Bill, E.; Weyhermüller, T.; Wieghardt, K. *J. Am. Chem. Soc.* **2001**, *123*, 10012-10023. (g) Blackmore, K. J.; Ziller, J. W.; Heyduk, A. F. Inorg. Chem. 2005, 44, 5559-5561. (h) Haneline, M. R.; Heyduk, A. F. *J. Am. Chem. Soc.* **2006**, *128*, 8410-8411. (i) Blackmore, K. J.; Lal, N.; Ziller, J. W.; Heyduk, A. F. *J. Am. Chem. Soc.* **2008**, *130*, 2728-2730. *Phenolates*: (j) Hockertz, J.; Steenken, S.; Wieghardt, K.; Hildebrandt, P. *J. Am. Chem. Soc.* **1993**, *115*, 11222-11230. (k) Chaudhuri, P.; Hess, M.; Muller, J.; Hildenbrand, K.; Bill, E.; Weyhermüller, T.; Wieghardt, K. *J. Am. Chem. Soc.* **1999**, *121*, 9599-9610. *Imino-pyridines*: (l) Bouwkamp, M. W.; Bowman, A. C.; Lobkovsky, E.; Chirik, P.

the prototypical redox-active ligand platforms. Porphyrin[3] π-electrons in metal porphyrin complexes are typically inert with the exception of Compound I in cytochrome P450 wherein a single oxidizing equivalent is stored in the porphyrin macrocyle.[4] In the case of porphyrinogen systems,[5] the pyrrole subunits are unconjugated and thus have higher energy π-orbitals, which results in increased ligand participation in molecular redox events. Transition metal complexes of both of these tetra-pyrrole macrocycle systems feature transition metal and ligand π-orbital alignment such that coupling of the two reservoirs is permitted.

Our recent interest in pyrrole-based ligands stems from our desire to determine if the rich redox chemistry which features prominently in metal-porphyrin and porphyrinogen complexes would translate to more easily-synthesized truncated frameworks (Scheme 2.1). Dipyrromethenes (A, Scheme 2.1),[6] like their porphyrin analogs, exhibit reversible, ligand-based redox events which are almost entirely decoupled from metal-based redox activity.[7]

J. *J. Am. Chem. Soc.* **2006**, *128*, 13340-13341. (m) Bart, S. C.; Chlopek, K.; Bill, E.; Bouwkamp, M. W.; Lobkovsky, E.; Neese, F.; Wieghardt, K. *J. Am. Chem. Soc.* **2006**, *128*, 13901-13912. (n) Bart, S. C.; Lobkovsky, E.; Bill, E.; Wieghardt, K.; Chirik, P. J. *Inorg. Chem.* **2007**, *46*, 7055-7063.

(3) Kadish, K. M., Smith, K. M., Guilard, R., Eds. *The Porphyrin Handbook*; Academic Press: San Diego, CA, 2003; Vols. 15-20.

(4) (a) Watanabe, Y. In *The Porphyrin Handbook*; Kadish, K. M.; Smith, K. M.; Guilard, R., Eds.; Academic Press: New York, 2000; Vol. 4, pp 97-118. (b) Schulz, C. E.; Devaney, P. W.; Winkler, H.; Debrunner, P. G.; Doan, N.; Chiang, R.; Rutter, R.;Hager, L. P. *FEBS Lett.* **1979**, *103*, 102-105. (c) Groves, J. T.; Haushalter, R. C.; Nakamura, M.; Nemo, T. E.; Evans, B. J. *J. Am. Chem. Soc.* **1981**, *103*, 2884-2886. (d) Penner-Hahn, J. E.; Smith Eble, K.; McMurry, T. J.; Renner, M.; Balch, A. L.; Groves, J. T.; Dawson, J. H.; Hodgson, K. O. *J. Am. Chem. Soc.* **1986**, *108*, 7819-7825.

(5) (a) Floriani, C.; Floriani-Moro, R. In *The Porphyrin Handbook*; Academic Press: San Diego, CA, 2003; Vol. 3, pp 405-420. (b) Jubb, J.; Floriani, C.; Chiesi-Villa, A.; Rizzoli, C. *J. Am. Chem. Soc.* **1992**, *114*, 6571-6573. (c) Piarulli, U.; Solari, E.; Floriani, C.; Chiesi-Villa, A.; Rizzoli, C. *J. Am. Chem. Soc.* **1996**, *118*, 3634-3642. (d) Crescenzi, R.; Solari, E.; Floriani, C.; Chiesi-Villa, Rizzoli, C. *J. Am. Chem. Soc.* **1999**, *121*, 1695-1706. (e) Bachmann, J.; Nocera, D. G. *J. Am. Chem. Soc.* **2004**, *126*, 2829-2837. (f) Bachmann, J.; Nocera, D. G. *J. Am. Chem. Soc.* **2005**, *127*, 4730-4733.

(6) Wood, T. E.; Thompson, A. *Chem. Rev.* **2007**, *107*, 1831-1861.

(7) King, E. R.; Betley, T. A. *Inorg. Chem.* **2009**, *48*, 2361-2363.

Dipyrromethane complexes (B, Scheme 2.1),[8] in contrast, displayed surprisingly uniform electrochemical behavior despite differences in metal valence electron configuration, geometry, and spin state.[9] The energetically high-lying π-electrons from the dipyrromethane framework almost exclusively account for the observed redox behavior of the metal complexes studied; indicating that fully populated ligand-based orbitals from the dipyrromethane construct lie above partially-filled metal 3*d* orbitals. Whereas the macrocylic nature of porphyrinogens stabilize ligand-centered radicals through the reversible formation of C–C bonds within the macrocyle,[5] the dipyrromethane metal complexes did not exhibit similar reactivity. Chemical oxidation of the metal-dipyrromethane complexes did not yield stable ligand-based diradical/dicationic species or readily identified metal-containing products. Thus we sought to develop a similar pyrrole-derived ligand platform that would be more amenable to study of the resulting oxidation products.

(8) (a) Lee, C.-H.; Lindsey, J. S. *Tetrahedron* **1994**, *50*, 11427-11440. (b) Jones, D. J.; Gibson, V. C. *Heterocycles* **2006**, *68*, 1121-1127. (c) Swartz, D. L.; Odom, A. L. *Organometallics* **2006**, *25*, 6125-6133. (d) Novak, A.; Blake, A. J.; Wilson, C.; Love, J. B. *Chem. Commun.* **2002**, 2796-2797. (e) Love, J. B.; Salyer, P. A.; Bailery, A. S.; Wislson, C. ; Blake, A. J.; Davies, E. S.; Evans, D. J. *Chem. Commun.* **2003**, 1390-1391.

(9) King, E. R.; Betley, T. A. *J. Am. Chem. Soc.* **2009**, *131*, 14374-14380.

Scheme 2.1

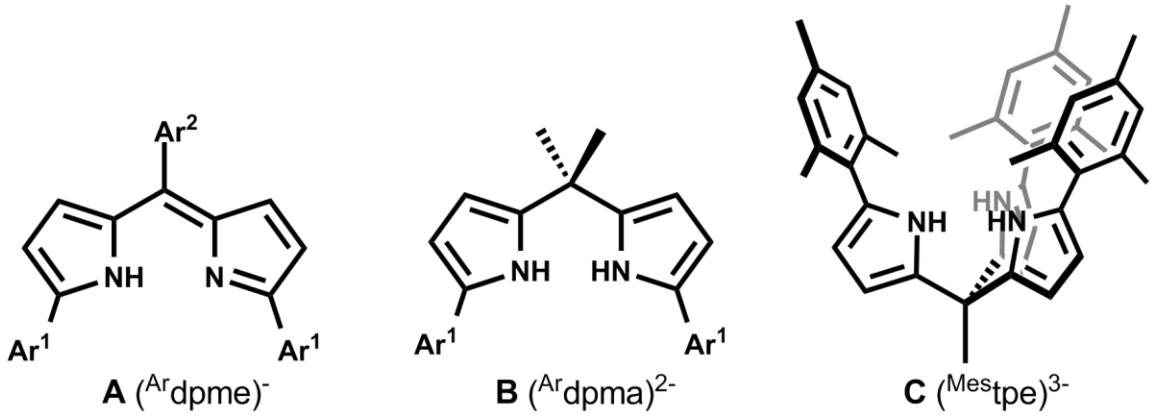

Sterically-encumbered, trianionic tris(pyrrolyl)ethane ligands (C, Scheme 2.1)[10] are potential candidates to circumvent the instability of the dipyrromethane analogues while maintaining the attractive attributes of these platforms (e.g., redox activity, attenuated *N* π-donicity). We hypothesized that a tris(pyrrolyl)ethane triply deprotonated and bound κ^3 to a divalent metal ion should be easier to oxidize than their neutral dipyrromethane analogues, and may confer greater stability to the oxidized products.[11] Furthermore, the tris(pyrrolyl)ethane platform, along with the dipyrromethene and dipyrromethane systems, relaxes the structural rigidity porphyrins and porphyrinogens require, opening the coordination sphere of the bound transition metal considerably.

(10) (a) Wang, Q. M.; Bruce, D. W. *Synlett* **1995**, 1267-1268. (b) Barnard, T. S.; Mason, M. R. *Inorg. Chem.* **2001**, *40*, 5001-5009. (c) Reese, C. B.; Yan, H. *Tet. Lett.* **2001**, *42*, 5545-5547. (d) Beer, P. D.; Cheetham, A. G.; Drew, M. G. B.; Fox, O. D.; Hayes, E. J.; Rolls, T. D. *Dalton Trans*. **2003**, *4*, 603-611. (c) Betley, T. A.; Surendranath, Y.; Childress, M. V.; Alliger, G. E.; Fu, R.; Cummins, C. C.; Nocera, D. G. *Phil. Trans. Royal Soc. B* **2007**, *363*, 1293-1303.

(11) (a) Byrne, E. K.; Theopold, K. H. *J. Am. Chem. Soc.* **1987**, *109*, 1282-1283. (b) Barner, C. J.; Collins, T. J.; Mapes, B. E.; Santarsiero, B. D. *Inorg. Chem.* **1986**, *25*, 4322-4323. (c) Collins, T. J.; Kotska, K. L.; Münck, E.; Uffelman, E. S. *J. Am. Chem. Soc.* **1990**, *112*, 5637-5639. (d) Collins, T. J.; Fox, B. G.; Hu, Z. G.; Kotska, K. L.; Münck, E.; Rickard, C. E. F.; Wright, L. J. *J. Am. Chem. Soc.* **1992**, *114*, 8724-8725. (e) Collins, T. J. *Acc. Chem. Res.* **1994**, *27*, 279-285.

2-2. Results

Scheme 2.2

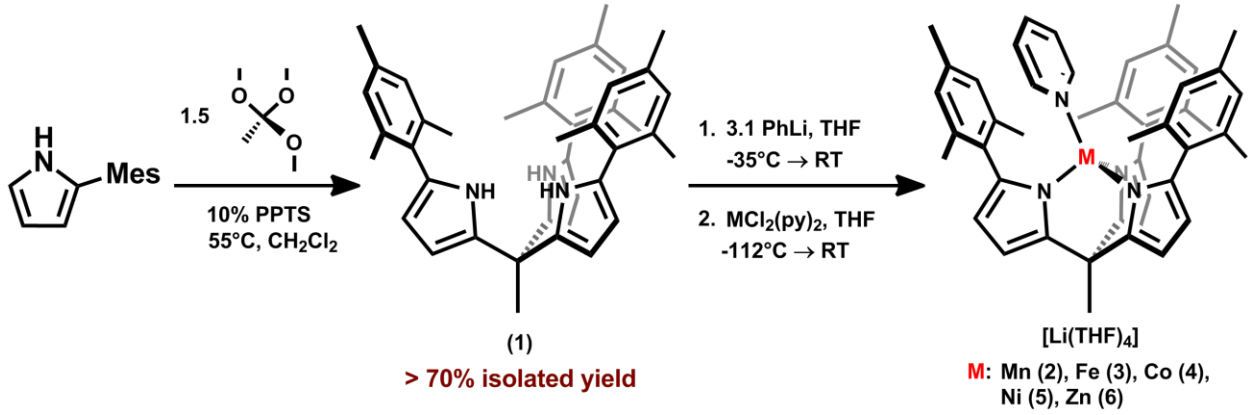

2.2.1 Synthesis and characterization of [tpe] and its metal complexes.

The synthesis of the tris(pyrrolyl)ethane ligand was accomplished using a modified acid-catalyzed[10a] condensation reaction between 2-mesityl pyrrole, 1.5 equivalents of trimethylorthoformate, and ~7% loading of pyridinium *p*-toluenesulfonate acid catalyst in two portions.[7,9] Refluxing this mixture in dichloromethane for several days, followed by flash chromatography and trituration with hexanes cleanly affords 1,1,1-tris(2-mesitylpyrrolyl)ethane ($tpeH_3$, **1**) as a pale yellow-white solid in greater than 69% isolated yield (Scheme 2.2). To assess the steric and electronic properties that **1** imparts, transition metal complexes of the tpe ligand were prepared in the following manner: reaction of **1** with 3.1 equivalents of phenyllithium ($LiN(SiMe_3)_2$ works equally well) in tetrahydrofuran generates the tri-lithio complex ($tpeLi_3$), which can be isolated but was typically prepared *in situ* for the following syntheses. The *in situ* generated tri-lithio species was then reacted with a stoichiometric amount of a divalent metal precursor (i.e., $MCl_2(py)_2$; M = Mn, Co, Fe, Ni, Zn; py = pyridine) in thawing THF solutions to afford the metalated salts of the type

[(tpe)M(py)][Li(THF)$_4$] upon isolation via crystallization (M = pale yellow Mn (**2**), bright orange Fe (**3**), blue Co (**4**), green Ni (**5**), and yellow-orange Zn (**6**)). The tpe ligand was found to uniformly bind in an η^1,η^1,η^1-coordination mode, strictly enforcing a four-coordinate geometry at the metal ion as confirmed by X-ray diffraction studies. The solid state molecular structures for the tetrahedral Mn (**2**), Fe (**3**), Co (**4**), Ni (**5**), and Zn (**6**) complexes are shown in Figure 2.1.

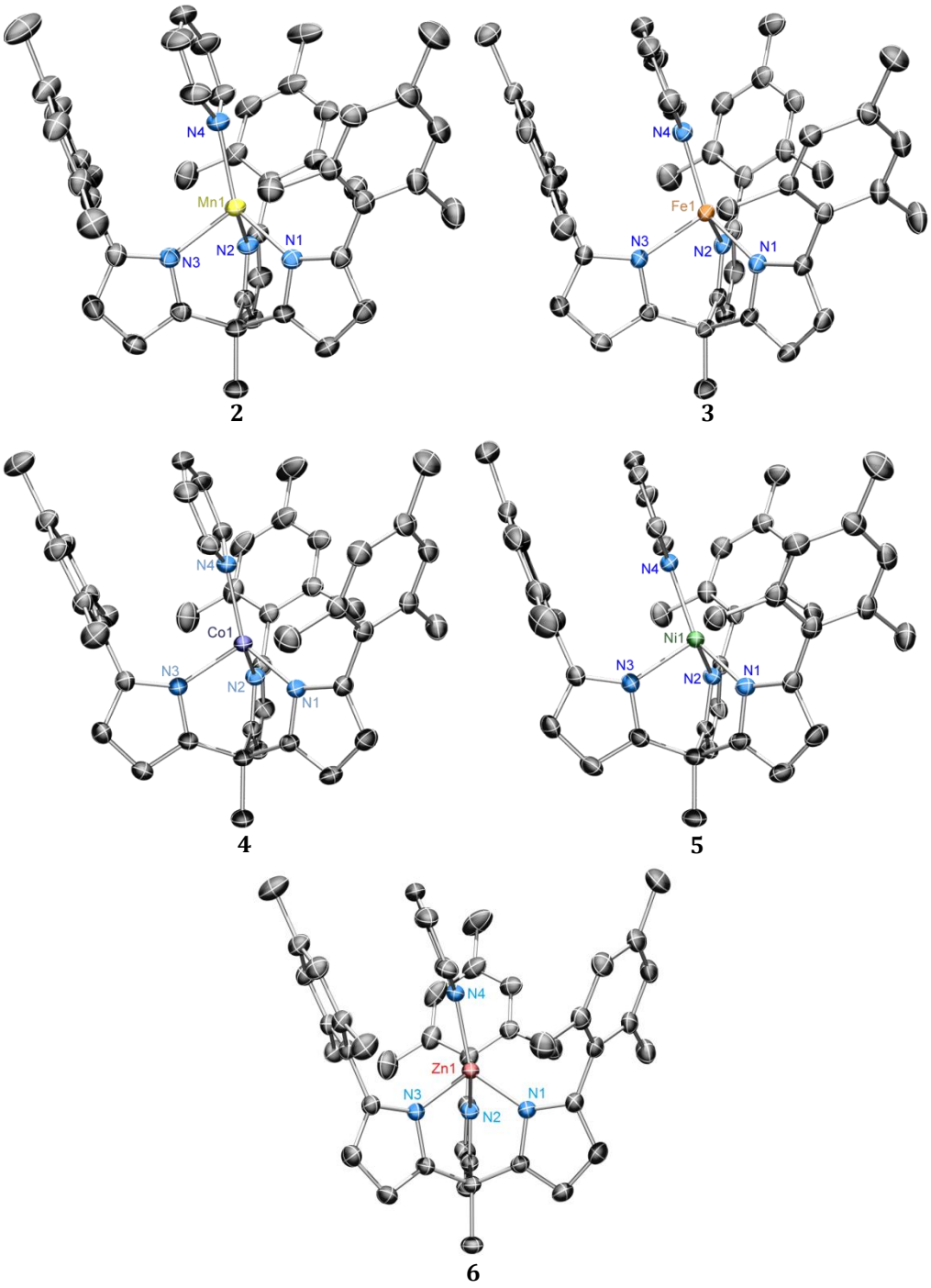

Figure 2.1. Solid-state molecular structure of the anions for complexes **2** - **6** with the thermal ellipsoids set at the 50% probability level (hydrogen atoms, solvated Li cations, and positional disorder in **5** are omitted for clarity).

Table 2.1. X-ray diffraction experimental details for **2** - **6**.[a,b]

	2	3	4	5	6
Empirical Formula	$C_{62}H_{79}LiMnN_4O_4$	$C_{62}H_{83}FeLiN_4O_4$	$C_{66}H_{87}CoLiN_4O_5$	$C_{62}H_{79}LiN_4NiO_4$	$C_{66}H_{87}LiN_4O_5Zn$
FW	1006.17	1011.11	1082.27	1009.94	1088.71
Space Group	$C2/c$	$C2/c$	$P\text{-}1$	$P2_1/n$	P-1
a (Å)	18.6178(9)	19.4776(12)	12.0728(7)	13.0737(17)	12.0972(8)
b (Å)	16.7236(8)	15.5448(10)	13.1443(7)	22.273(3)	13.2008(8)
c (Å)	38.7477(18)	38.314(2)	21.9752(12)	19.323(5)	21.9749(14)
α (°)	90	90	77.5480(10)	90	77.6430(10)
β (°)	102.5460(10)	102.561(2)	88.9730(10)	93.16(3)	89.1500(10)
γ (°)	90	90	63.4090(10)	90	62.8850(10)
V (Å^3)	11776.3(10)	11322.8(12)	3032.6(3)	5618.1(18)	3037.3(3)
Z	8	8	2	4	2
μ (mm^{-1})	0.271	0.316	0.334	0.395	0.455
Reflections	53543	49291	51355	78916	50961
Completeness (to θ)	99.8% (26.66°)	99.9% (27.48°)	100.0% (25.03°)	99.6% (27.31°)	99.7% (28.01°)
GOF on F^2	1.041	1.012	1.034	1.019	1.035
R1, wR2[b] [I>2σ (I)]	0.0534, 0.1508	0.0614, 0.1399	0.0433, 0.1187	0.0506, 0.1228	0.0526, 0.1464
$R_{indices}$ (all) (R1, wR2)	0.0663, 0.1597	0.1350, 0.1694	0.0496, 0.1253	0.0817, 0.1429	0.0634, 0.1579

[a] λ (Å) = 0.71073

[b] Collection temperature (T) = 193(2) K for **3**-**9**, 100(2) K for **10**.

[c] $R1 = \Sigma\big||F_o| - |F_c|\big|/\Sigma|F_o|$, $wR2 = \{\Sigma[w(F_o^2 - F_c^2)^2]/\Sigma[w(F_o^2)^2]\}^{1/2}$.

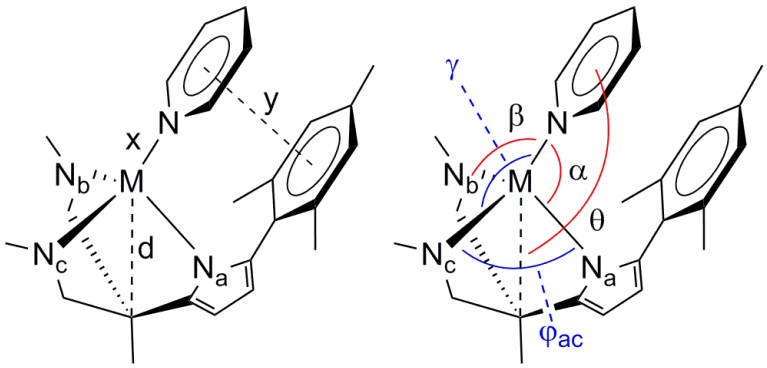

Table 2.2. Selected bond lengths (Å) and angles (°) for complexes **2 - 6.**

M	M-N_a	M-N_b	M-N_c	d (Å)	x (Å)	y (Å)
Mn (**2**)	2.070	2.078	2.073	2.996	2.147	4.040
Fe (**3**)	2.015	1.999	2.027	2.918	2.068	3.739
Co (**4**)	1.973	1.981	1.975	2.863	2.016	3.617
Ni (**5**)	1.960	1.955	1.989	2.935	2.040	3.528
Zn (**6**)	1.988	1.981	1.984	2.876	2.009	3.623

M	θ (°)	α (°)	β (°)	γ (°)	φ_{ab}	φ_{ac}	φ_{bc}
Mn (**2**)	168.13	114.18	134.84	120.77	92.10	93.48	90.93
Fe (**3**)	161.43	107.67	138.65	117.07	94.38	95.52	94.29
Co (**4**)	168.06	109.17	127.75	123.67	96.27	96.20	96.67
Ni (**5**)	157.95	105.74	115.20	143.96	94.33	94.76	91.87
Zn (**6**)	168.24	109.62	123.97	127.73	95.90	95.86	96.43

2.2.2 Structural Characterization of complexes 2-6.

Complexes **2**-**6** are nearly isostructural featuring an intermediate geometry between trigonal-monopyramidal and pseudo-tetrahedral at the metal center. The pyridine ligand and two of the tpe pyrrolide substituents (N_b, N_c) form the trigonal base with one pyrrolide ligand (N_a) capping the trigonal mono-pyramid. The sum of the angles of the mono-pyramidal base (N_{py}, N_b, N_c) $\alpha+\beta+\varphi_{bc}$, sum to nearly 360° for each complex ($\alpha+\beta+\varphi_{bc}$ (°): Mn 347, Fe 350, Co 348, Ni 351, Zn 348). The pyridine ligand is consistently positioned off the molecular three-fold axis (defined as vector *d* in the above illustration), positioning the pyridine ligand in a distinct π-stacking interaction with the N_a pyrrolide mesityl substituent (ranging from 3.5-4.0 Å separation between the pyridine centroid and the mesityl centroid).[12] The angle θ describes the orientation of the pyridine ligand with the molecular C_3 axis, such that a θ of 180° would describe a perfect C_3 symmetric orientation of the pyridine ligand. The θ angles listed in **Table 2.2** show a deviation from linearity (θ = 157-168°). For complexes **2**-**6**, the bond lengths within the tpe ligand framework do not vary considerably. The metal pyrrolide nitrogen bond lengths decrease across the series from Mn→Ni, with Zn being slightly elongated (d_{avg} (Å): Mn..N_{tpe} = 2.074, Fe..N_{tpe} = 2.014, Co..N_{tpe} = 1.976, Ni..N_{tpe} = 1.968, Zn..N_{tpe} = 1.984 (see **Table 2.2** for a more comprehensive comparison of bond lengths).

(12) (a) McGaughey, G. B.; Gagné, M. Rappé, A. K. *J. Biol. Chem.* **1998**, *273*, 15458-15463. (b) Meyer, E. A.; Castellano, R. K.; Diederich, F. *Angew. Chem. Int. Ed.* **2003**, *42*, 1210-1250.

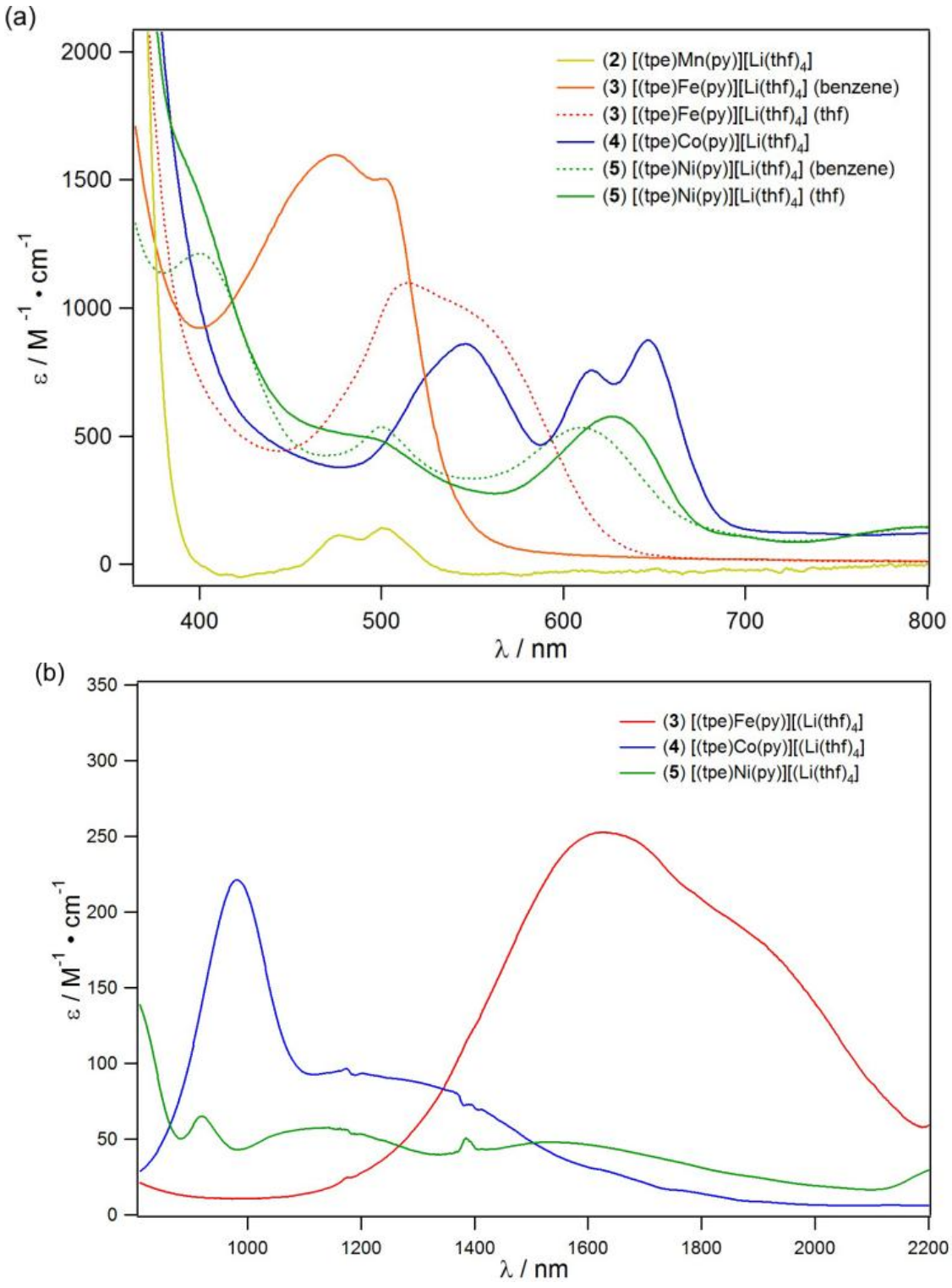

Figure 2.2. (a) UV/vis molar absorptivity spectra of **2**, **3** in benzene, **3** in THF, **4**, **5** in benzene, and **5** in THF; and (b) NIR molar absorptivity spectra of **3**, **4**, and **5** in THF. Spectra were taken in THF (unless otherwise noted), molar absorptivities are based on measurements at a minimum of 4 different concentrations.

Table 2.3. Magnetic and spectral properties of complexes **2**, **3**, **4**, and **5**.

Complex	*S*	μ_{eff} (BM)[a]	λ / nm (ε / M^{-1}·cm^{-1})	δ (ΔE_q) (mm/s)
[(tpe)Mn(py)][Li(thf)$_4$] (**2**)	5/2	6.2(1)	331 (11000), 502 (140), 477 (110)	--
[(tpe)Fe(py)][Li(thf)$_4$] (**3**)	2	5.1(1)	317 (16000), 516 (1100), 560 (920)^{sh}, 1636 (250), 1911 (180)^{sh}	0.84 (2.54)
[(tpe)Co(py)][Li(thf)$_4$] (**4**)	3/2	4.8(1)	325 (12000), 550 (850), 621 (730), 650 (860), 998 (200), 1250 (90)^{sh}	--
[(tpe)Ni(py)][Li(thf)$_4$] (**5**)	1	2.9(1)	319 (13000), 398 (1500)^{sh}, 504 (500)^{sh}, 631 (570), 800 (120), 928 (60)	--

[a] Room temperature (295 K) moment in solution by Evans method.[13]

2.2.3 Electronic and magnetic characterization of complexes 2-5.

The magnetic and spectral data for complexes **2-5** are provided in **Table 2.3**. All four complexes feature an intense absorption in the UV region centered around 320 nm (ε / (M^{-1} cm^{-1}): 11000-16000) which dominate all other transitions observed. The pale yellow, ^{1}H NMR silent, high spin d^5 (S = $^5/_2$, μ_B = 6.2(1)) Mn complex **2** has only two very weak transitions in the visible region (Figure 2.2a, λ_{max} / nm (ε / M^{-1} cm^{-1}): 502 (140), 477 (110)) and no transitions were observed in the near-infrared region (NIR). In benzene solutions, the high spin d^6 (S = 2, μ_B = 5.1(1)) Fe complex **3** maintains its bright orange hue (λ_{max} / nm (ε / M^{-1} cm^{-1}): 505 (1500), 477 (1600)), but turns an intense magenta color upon dissolution in THF (λ_{max} / nm (ε / M^{-1} cm^{-1}): 516 (1100), 560 (920)). This significant λ_{max} shift (55 nm) could be attributable to solvent binding in THF, but we have no evidence for accessing five-coordinate structures (in solution or the solid-state). The Mössbauer

(13) (a) Evans, D. F. *J. Chem. Soc.* **1959**, 2003-2005. (b) Sur, S. K. *J. Magn. Reson.* **1989**, *82*, 169-173.

spectrum of **3** (Figure 2.6a) is best modeled as a single quadrupole doublet and parameters consistent with the Fe^{II} assignment (δ = 0.84 mm·s^{-1}, $|\Delta E_Q|$ = 2.54 mm·s^{-1}) in a tetrahedral ligand field. The high spin d^7 ($S = {}^3/_2$, μ_B = 4.8(1)), dark blue Co complex **4** shows several transitions in the visible region (λ_{max} / nm (ε / M^{-1} cm^{-1}): 550 (850), 621 (730), 650 (860)), but no solvent dependence like complex **3**. While not as significant as **3**, the spectral features of the high spin d^8 (S = 1, μ_B = 2.9(1)), green Ni complex **5** sharpen considerably in benzene solutions, but the gross spectral features are consistent with THF solutions (λ_{max} / nm (ε / M^{-1} cm^{-1}): 504 (500), 631 (570), 800 (120)). All of the spectral features for complexes **2-5** are of the appropriate magnitude for spin-allowed d-d transitions for the high spin complexes in pseudo-tetrahedral ligand fields. The Fe (**3**), Co (**4**) and Ni (**5**) all show very weak absorptions in the NIR region (Figure 2.2b) with molar absorptivities (ε = 50-250 M^{-1} cm^{-1}) substantially less than expected for charge transfer bands (e.g. LMCT).

2.2.4 Electrochemical behavior of tris(pyrrolide)ethane complexes.

Cyclic voltammetry was performed on the mono-pyridine complexes, **2-6**, (0.3 M Bu_4NPF_6, Figure 2.3). Only the Fe complex **3** showed a quasi-reversible redox wave centered at −750 mV ($\Delta_{(EC-EA)}$ = 190 mV). Complexes **2**-**6** nearly exhibit the same onset of oxidation in the cyclic voltammetry experiments, with all of the complexes having the same peak anodic current at −655 mV (vs. Fc/Fc^+). Differential pulse voltammetry measurements scanning oxidatively over the potential range of −500 to −900mV (Figure 2.3b) shows that the peak anodic current for the Mn (**2**), Ni (**5**), and Zn (**6**) complexes is identical (-690mV), whereas the Fe (**3**; −770mV) and Co (**4**, −660mV) complexes are slightly shifted. We interpret the redox inactive Zn^{II} data to imply the observed oxidation step is ligand-

centered, originating from the tpe framework. Although the oxidations observed appear to be ligand-centered and vary little with divalent cation substitution, the onset of oxidation for metalated (tpe) shifts nearly 1.1 V from the free (tpe)H_3 (E_p = +375 mV).

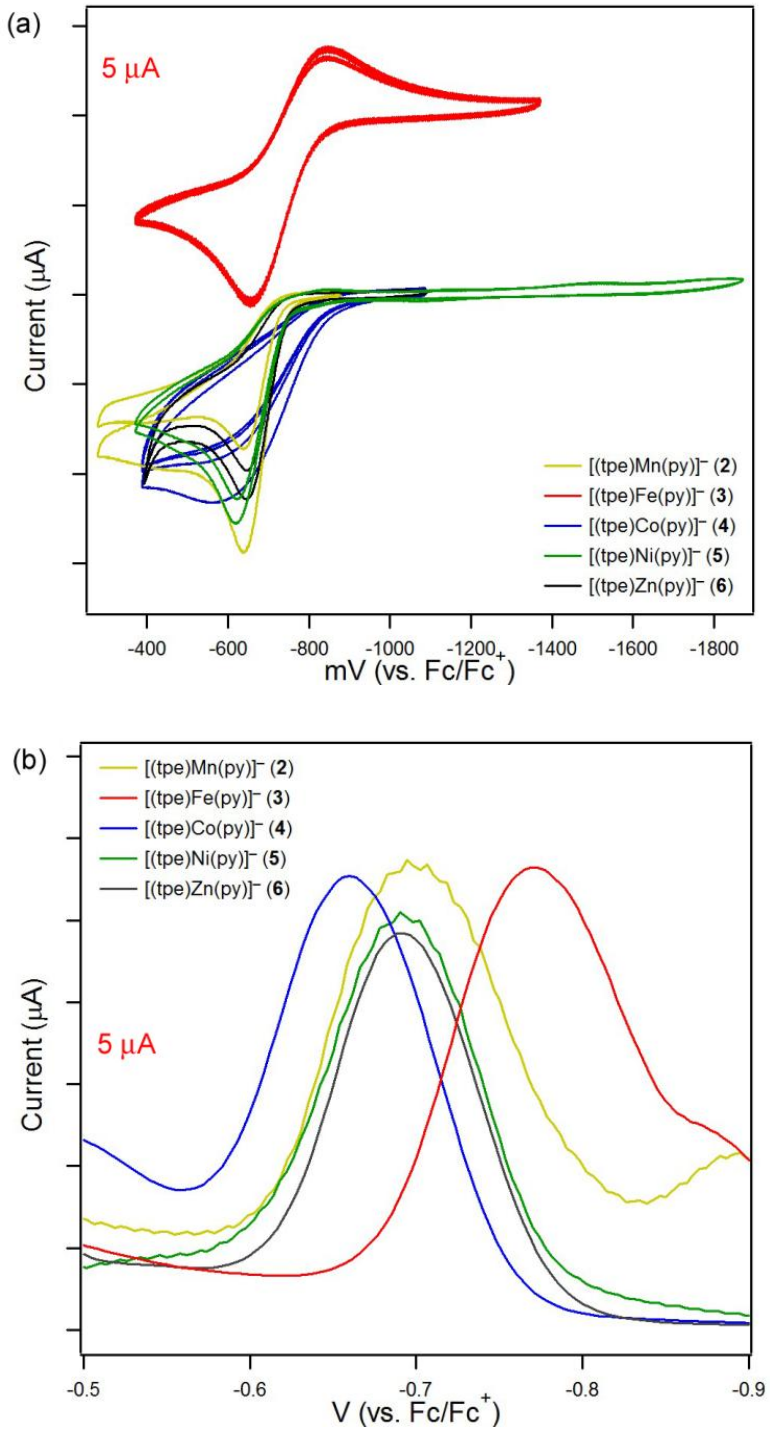

Figure 2.3. (a) Cyclic voltammograms of solutions in THF of 3 mM $[(tpe)M(py)]^-$ (M = Mn (**2**), Fe (**3**), Co (**4**), Ni (**5**), Zn (**6**); Bu_4NPF_6 (0.3 M); scan rate 25 mV/s on glassy C electrode; (b) differential pulse voltammograms for solutions in THF of 10^{-4} M $[(tpe)M(py)]^-$ (M = Mn (**2**), Fe (**3**), Co (**4**), Ni (**5**), Zn (**6**); Bu_4NPF_6 (0.3 M); scan rate 25 mV/s on glassy C electrode.

2.2.5 Chemical Oxidation Products.

Scheme 2.3

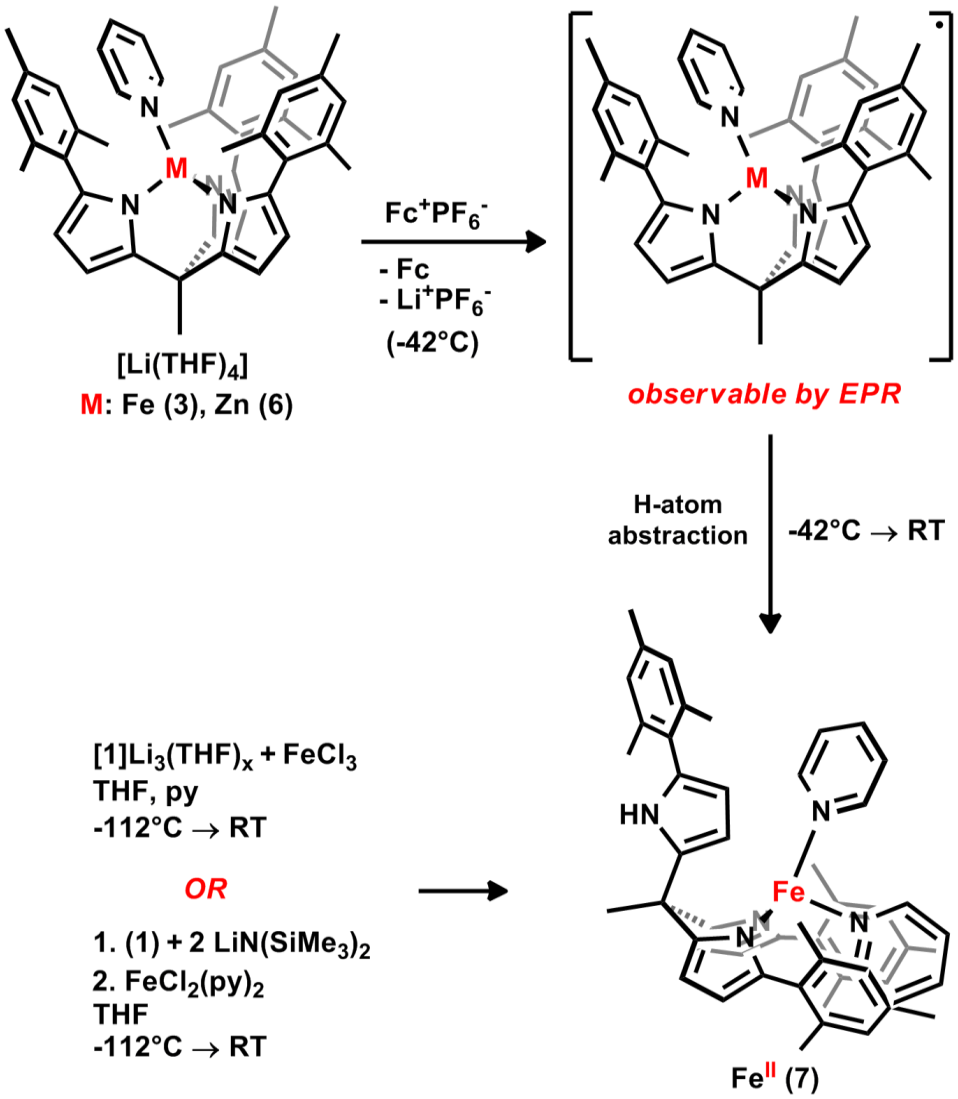

Chemical oxidation of [(tpe)Zn(py)][Li(THF)$_4$] (**6**) with $Fc^+PF_6^-$ did not lead to tractable products when warmed to room temperature (Fc = $(\eta^5\text{-}H_5C_5)_2Fe$). However, maintaining the reaction temperature at −42ºC in an acetonitrile/dry ice bath we were able to observe the consumption of the ferrocenium oxidant by ^{1}H NMR and a detectable oxidized species by EPR (Scheme 2.3). Consumption of the oxidant is also apparent as the pale yellow color

of **6** quickly gives way to an intense dark brown color of the oxidized product. The EPR spectrum for this oxidation product is shown in Figure 2.4, which shows an isotropic signal virtually unperturbed for an organic radical (g = 2.0023).

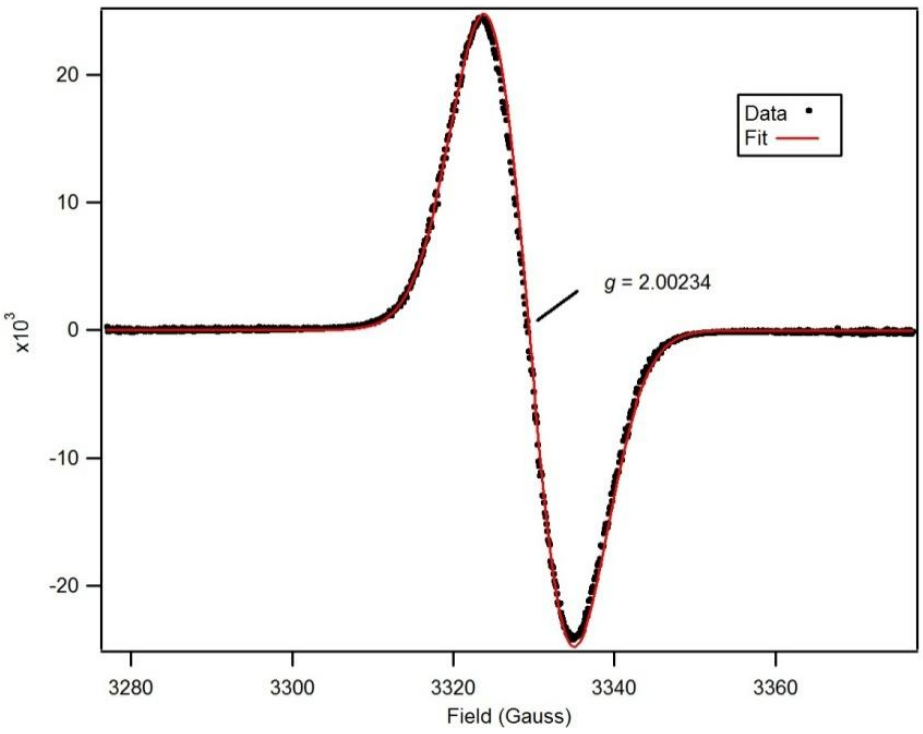

Figure 2.4. Toluene glass EPR of oxidation product of [(tpe)Zn(py)][Li(THF)$_4$] + $Fc^+PF_6^-$ (dotted line is experimental data and red line is data simulation: g = 2.0023, S = 1/2; 77 K, X-band, 9.3298 GHz; fit with Gaussian and Lorentzian functions).

Encouraged by the quasi-reversible nature of the electrochemical oxidation of the Fe complex **3**, we canvassed the reactivity **3** with a range of chemical oxidants. Low temperature oxidation of **3** with $Fc^+PF_6^-$ or $NO^+SbF_6^-$ (frozen THF → room temperature) gave rise to a new paramagnetic product(s) by ^{1}H NMR. As with the oxidation of **6**, oxidation of **3** quickly changes from orange (in arene solvents) to an intense brown color upon consumption of the oxidant. This product mixture was unaffected by temperature (thawing THF, −42ºC, or room temperature) or chemical oxidant employed during the

reaction. Following removal of volatiles *in vacuo*, extraction of the reaction mixture with diethyl ether and removal of the ferrocene by washing with copious amounts of hexanes separated the tpe-containing products. Storage of this material in diethyl ether at −35ºC gave crystals of a yellow brown material that was suitable for X-ray diffraction analysis. The molecular structure of this crystal is shown in Figure 2.5. In the product one of the pyrrolide donors is not bound to the Fe which now features two pyridine molecules giving the formulation (κ^2-tpe)Fe(py)$_2$ (**7**). The production of **7** could be maximized by running the oxidation of **3** in a mixture of THF and pyridine as a solvent (frozen THF→RT). Authentic samples of **7** were prepared by deprotonation of (tpe)H$_3$ (**1**) with two equivalents of LiN(SiMe$_3$)$_2$ in THF followed by addition of FeCl$_2$(py)$_2$. Comparing the ^{1}H NMR spectrum of the crude reaction mixture from the chemical oxidation **3** with an authentic sample of **7** confirms that **7** is the major species formed in that product mixture. Furthermore, reaction of *in situ* prepared (tpe)Li$_3$ with FeCl$_3$ in a mixture of pyridine and THF produced large quantities of **7** as the dominant product (Scheme 2.3).

Mössbauer spectroscopy on the reaction product of **3** with chemical oxidants indicated that a mixture of species was present (Figure 2.6b). The spectrum can be tentatively modeled as a three component mixture with one major species (δ, $|\Delta E_Q|$ (mm·s^{-1}): component 1: 0.81, *3.27* (56.9%); component 2: 0.71, *2.21* (33.5%); component 3: 1.02, *1.51* (9.6%)). The isomer shifts and quadrupole splitting parameters are similar in nature to those for complex **3**. Mössbauer analysis of an authentic sample of **7** is provided in Figure 2.6c and its isomer shift and quadrupole splitting (δ, $|\Delta E_Q|$ (mm·s^{-1}): 0.81, *3.47*) match the major product from the chemical oxidation of **3**, and are nearly identical for the related

dipyrromethane analogue (^{Mes}dpma)Fe^{II}(py)$_2$ (δ, $|\Delta E_Q|$ (mm·s^{-1}): 0.80, *3.46*).[9] The secondary component apparent in the Mössbauer spectrum of **7** (Figure 2.6c) is potentially due to geometric isomer of **7**,[14] similar to that observed in the related dipyrromethane analogue (^{Mes}dpma)Fe^{II}(py)$_2$, although the presence of two isomers could not be resolved by ^{1}H NMR spectroscopy.[9] The presence of two isomers for **7** in solution is readily apparent by ^{1}H NMR, with two sets of proton resonances obvious in analytically pure samples of **7** where the composition was ascertained by combustion analysis. The spectrum shown in Figure 2.6c was obtained quickly after preparation of **7**. Mössbauer analysis on samples of **7** where both isomers are present in equal quantities by ^{1}H NMR show both sets of quadrupole doublets that comprise the spectrum in Figure 2.6c.

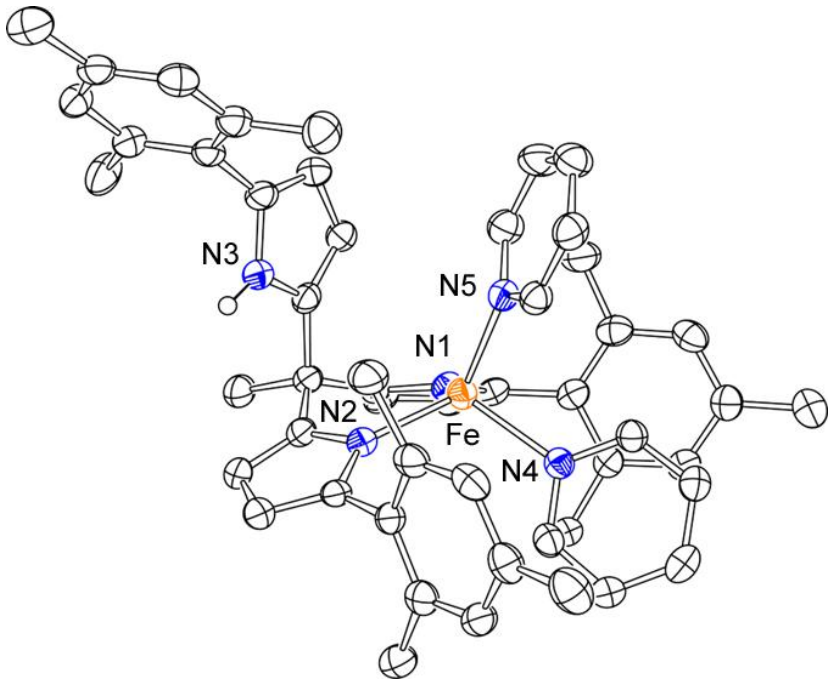

Figure 2.5. Solid-state molecular structure of **7** with the thermal ellipsoids set at the 50% probability level (hydrogen atoms are omitted for clarity).

(14) Long, G. J.; Whitney, D. L.; Kennedy, J. E.; *Inorg. Chem.* **1971**, *10*, 1406-1410.

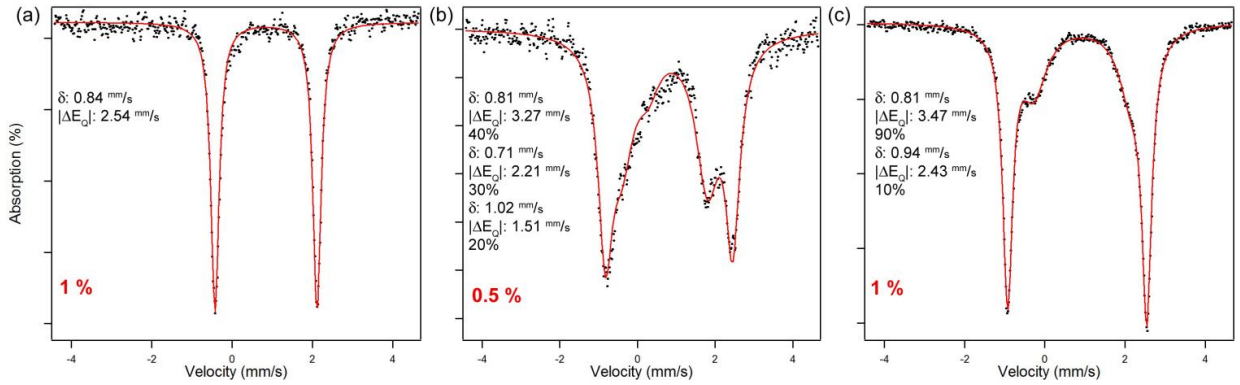

Figure 2.6. Mössbauer spectrum of (a) [(tpe)Fe(py)][Li(thf)$_4$] (**3**) at 77 K (δ, $|\Delta E_Q|$ (mm·s^{-1}): 0.84, *2.54*; (b) oxidation product of **3** with $Fc^+PF_6^-$, at 77 K (δ, $|\Delta E_Q|$ (mm·s^{-1}): component 1: 0.81, *3.27* (56.9%); component 2: 0.71, *2.21* (33.5%); component 3: 1.02, *1.51* (9.6%); (c) (κ^2-tpe)Fe(py)$_2$ (**7**) at 77 K (δ, $|\Delta E_Q|$ (mm·s^{-1}): component 1: 0.81, *3.47* (80.6%); component 2: 0.94, *2.43* (19.4%).

2.2.6 Density Functional Theoretical Considerations.

To further probe the electronic structure of the [(tpe)M(py)]$^-$ anions **2-6**, geometry optimization calculations were performed (M05-2X/6-31G).[15,16] Use of the M05-2x functional was necessary in order to reproduce the pyridine/mesityl π-stacking effect observed in each of the solid-state structures for complexes **2-6**. Upon satisfactory optimization of the molecular geometries, a single point population analysis was performed to compute the orbital energies for complexes **2-6** using standard functionals and larger basis sets (B3LYP/Fe,N: TZV(P); all other atoms: SV(P)).[17,18,19] The frontier orbital energies for complexes **2-6** are presented in Figure 2.7. The orbitals originating from the tpe ligand are shown in red, metal 3*d* orbitals in gray, and pyridine orbitals are shown in black. In every instance the Mulliken population analysis (MPA) calculations

(15) (a) Zhao, Y., Schultz, N. E., and Truhlar, D. G., *J. Chem. Theory Comp.* **2006**, *2*, 364-382. (b) Zhao, Y.; Truhlar, D. G. *Acc. Chem. Res.* **2008**, *41*, 157-167.
(16) R. Ditchfield, W. J. Hehre, and J. A. Pople, *J. Chem. Phys.* **1971**, *54*, 724-728.
(17) (a) Becke, A. D. *J. Chem. Phys.* **1993**, *98*, 5648-5652. (b) Vosko, S. H.; Wilk, L.; Nusair, M. *Can. J. Phys.* **1980**, *58*, 1200-1211. (c) Lee, C.; Yang, W.; Parr, R. G. *Phys. Rev. B* **1988**, *37*, 785-789.
(18) Schäfer, A.; Huber, C.; Ahlrichs, R. *J. Chem. Phys.* **1994**, *100*, 5829-5835.
(19) Schäfer, A.; Horn, H.; Ahlrichs, R. *J. Chem. Phys.* **1992**, *97*, 2571-2577.

indicate the highest lying occupied molecular orbitals (HOMO, HOMO-1) exclusively feature ligand π-character on the pyrrole subunits, illustrated for complex **3** in Figure 2.8. Across the series, the metal 3*d* orbitals do not significantly contribute to the frontier orbitals until HOMO-4, approximately 1.5 eV lower in energy than the ligand-based HOMO. Only the Fe complex **3** shows a significant component of metal 3*d* orbital contribution to the frontier orbitals in the β population. The spin density plot (α−β) for the Fe complex (Figure 2.9d) shows that all of the unpaired spin is localized on the metal ion, which is consistent for all the open-shell molecules examined (**2**, **4**, and **5**; Figure S2-S4).

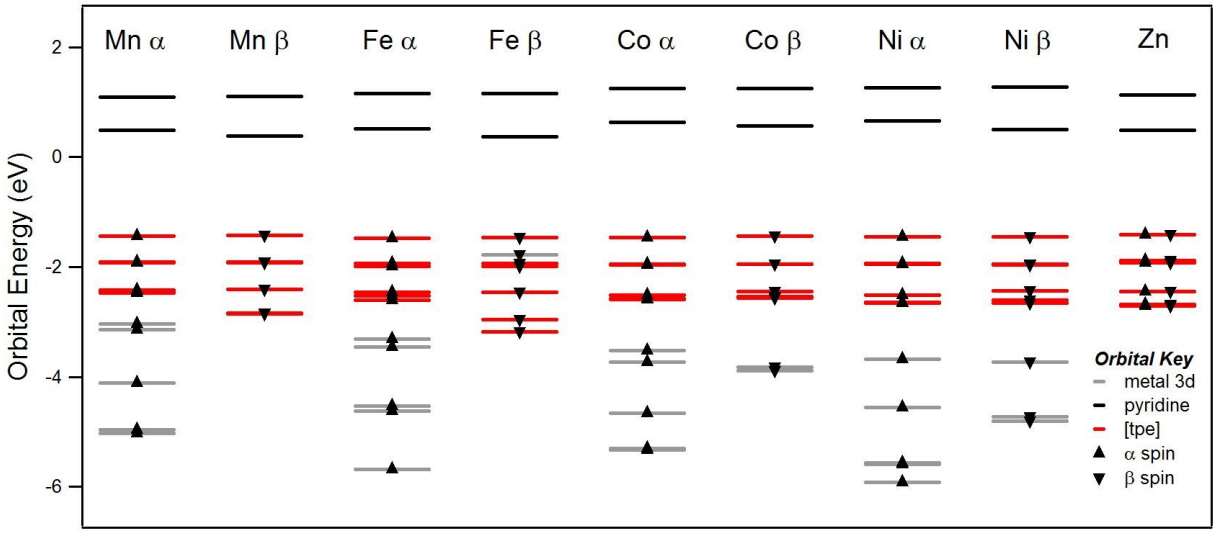

Figure 2.7. Calculated α (▲) and β (▼) orbital energies for [(tpe)M(py)]⁻ complexes: Mn (**2**), Fe (**3**), Co (**4**), and Ni (**5**). Calculated molecular orbitals for [(tpe)Zn(py)]⁻ (**6**). Metal-based orbitals are gray, tris(pyrrolyl)ethane ligand-based orbitals are red, and pyridine-based orbitals are black.

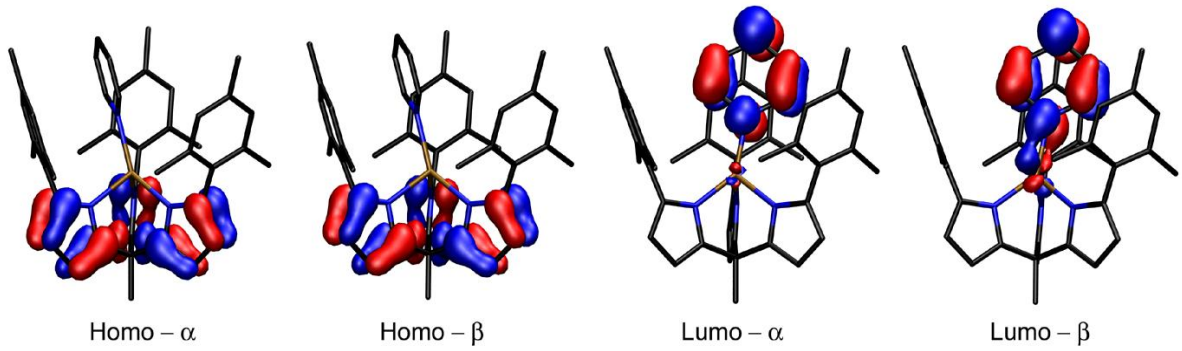

Figure 2.8. HOMO (α and β) and LUMO (α and β) from frontier orbital diagrams for complex **3** (Fe, *S* = 2) by DFT (B3LYP/TZV(P), SV(P); Gaussian 03).

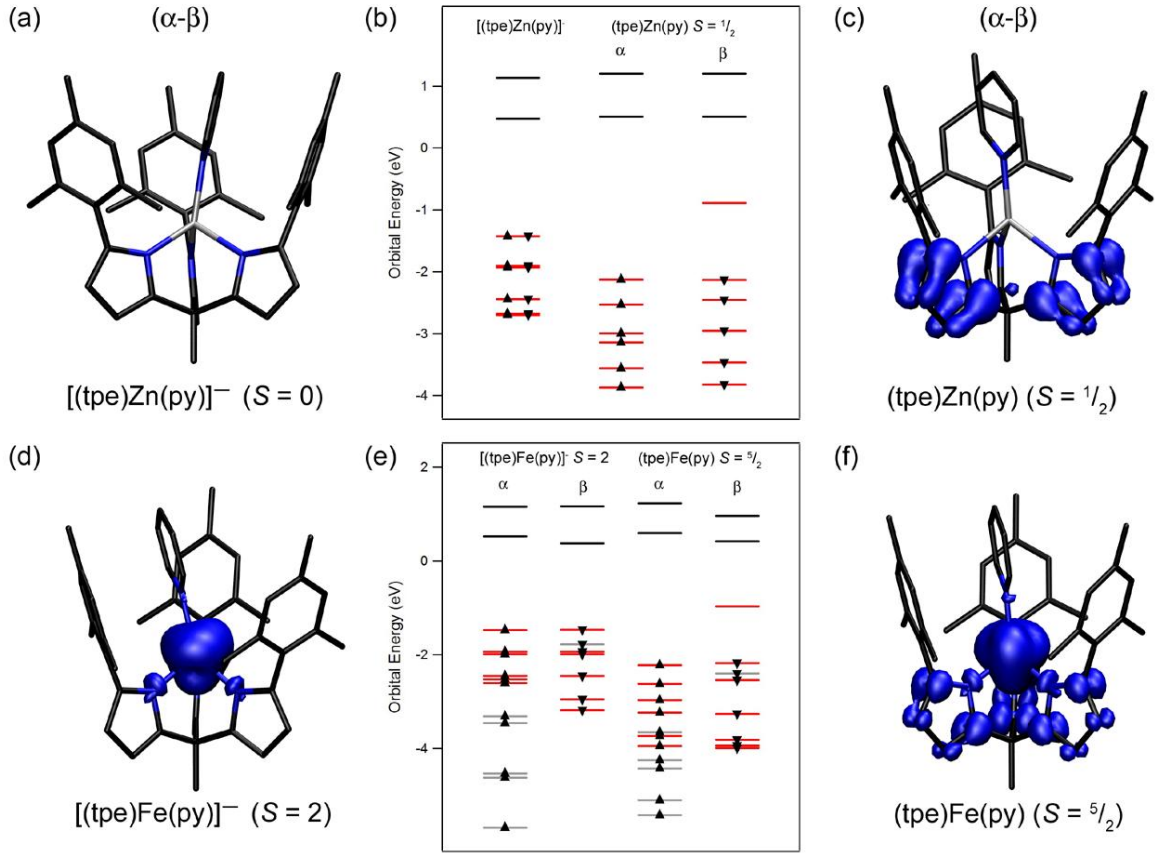

Figure 2.9. Calculated spin population (α – β) for (a) [(tpe)Zn(py)]⁻ (*S* = 0), (c) (tpe)Zn(py) (*S* = $^1/_2$), (d) [(tpe)Fe(py)]⁻ (*S* = 2), (f) (tpe)Fe(py) (*S* = $^5/_2$); (b) molecular orbitals for [(tpe)Zn(py)]⁻ and calculated α (▲) and β (▼) orbital energies for the oxidation product (tpe)Zn(py) (*S* = $^1/_2$); (e) calculated α (▲) and β (▼) orbital energies for [(tpe)Fe(py)]⁻ (*S* = 2) and the oxidation product (tpe)Fe(py) (*S* = $^5/_2$) by DFT (B3LYP/TZV(P), SV(P); Gaussian 03).

We also probed the structure of the oxidation products for the Zn and Fe anions by density functional methods. The geometries for the oxidized complexes (tpe)Zn(py) (S = ½, **8**) and (tpe)Fe(py) (S = $^5/_2$, **9**) were optimized using the optimized structure data **6** and **3** as starting points, respectively. The geometry optimization of (tpe)Fe(py) with S = $^3/_2$ was also examined, but failed to converge using standard convergence criteria. The total energy of both optimized structures for the oxidation products was higher in energy (**8**, +2.531 eV; **9**, +2.465 eV) than the geometry minimized structures for the corresponding anions. The calculated α and β orbital energies presented in Figure 2.9b and e were offset by these energy differences to correct for the overall structural zero-point energy differences. In both instances, the new HOMO-LUMO gaps (1.2 eV for oxidized Zn and Fe products) were substantially lower than those calculated for **6** (1.9 eV) or **3** (2.2 eV). The calculated spin densities (α − β) for the oxidation products of **6** and **3** are shown in Figure 2.9c and f, respectively. The resultant radical density for the S = $^1/_2$ (tpe)Zn(py) is contained entirely within the (tpe) framework, consistent with organic-radical like EPR spectrum (Figure 2.4) observed for the oxidation product. Similarly, the calculated spin density for the oxidation product (tpe)Fe(py), assuming a S = $^5/_2$ ground state, now shows considerable ligand contribution (Figure 2.9f), whereas the spin is localized completely on the Fe ion for **3** (Figure 2.9d).

2-3. Discussion

2.3.1 [(tpe)M(py)]⁻ Structural considerations.

The tpe ligand framework is a rigid, tripodal framework that sterically enforces a pseudo-tetrahedral coordination environment about the bound transition metal ion. Accordingly, this class of complexes is related to other "tetrahedral enforcer" ligands (e.g. tris(^{R}L)borates[20,21,22]), but differs in that it coordinates transition-metals as a trianionic species. The N_{tpe}–M bond lengths decrease across the series from Mn→Ni, which is consistent with the decreasing high-spin ionic radius for the series. The pyridine ligand is not bound along the three-fold axis of symmetry (i.e., axis depicted "d" in the diagram for **Table 2.2**) for any of the molecules reported, even for the d^5 Mn (**2**) and d^{10} Zn (**6**) complexes where steric minimization should dominate bonding. Instead the pyridine is bound well off-axis, positioned in a π-stacking orientation with one of the ligand mesityl fragments resulting in a trigonal monopyramidal geometry instead of a tetrahedral arrangement. The pyridine-mesityl separation (3.5-4.0 Å) is within π-stacking distances reported in the literature and is estimated to provide an additional 1-2 kcal/mol of energy to the stabilization of the ground state.[12] While the pyridine binding off-axis could maximize the π-overlap between the metal d-orbitals (i.e., 2e set for a ML_3 fragment) and

(20) (a) Trofimenko, S. *J. Am. Chem. Soc.* **1966**, *88*, 1842-1844. (b) Trofimenko, S. *Chem. Rev.* **1993**, *93*, 943-980.

(21) Byers, P. K.; Canty, A. J.; Honeyman, R. T. *Adv. Organometallic Chem.* **1992**, *34*, 1-65.

(22) (a) Tris(alkylthiol)borate: Ge, P.; Haggerty, B. S.; Rheingold, A. L.; Riordan, C. G. *J. Am. Chem. Soc.* **1994**, *116*, 8406-8407. (b) Schebler, P. J.; Mandimutsira, B. S.; Riordan, C. G.; Liable-Sands, L. M.; Incarvito, C. D.; Rheingold, A. L. *J. Am. Chem. Soc.* **2001**, *123*, 331-332. (c) Tris(alkylphosphino)borates: Peters, J. C.; Feldman, T. D.; Tilley, T. D. *J. Am. Chem. Soc*. **1999**, *121*, 9871-9872. (d) Barney, A. A.; Heyduk, A. F.; Nocera, D. G. *Chem. Commun*. **1999**, 2379-2380. (e) Betley, T. A.; Peters, J. C. *Inorg. Chem*. **2003**, *42*, 5074-5084. (f) Thomas, C. M.; Mankad, N. P.; Peters, J. C. *J. Am. Chem. Soc.* **2006**, *128*, 4956-4957. Tris(carbeno)borates: (g) Nieto, I.; Cervantes-Lee, F.; Smith, J. M. *Chem. Commun.* **2005**, 3811-3813. (h) Cowley, R. E.; Bontchev, R. P.; Duesler, E. N.; Smith, J. M. *Inorg. Chem.* **2006**, *45*, 9771-9780.

the pyridine π-accepting orbitals,[23] the π back-bonding contribution to the M–pyridine binding should be quite minimal for the high-spin, 3*d* M^{2+} ions examined, and therefore the π-stacking interaction is the most likely cause for deviation from the expected C_{3v} geometry.

2.3.2 Electronic structure.

In our studies of the redox properties of the related dipyrromethane metal complexes of the type (^{Mes}dpma)M(py)$_2$, we observed matching of the ligand based orbitals with the frontier metal orbitals similar to the tpe system presented here.[9] We considered three possible scenarios regarding potential intramolecular redox for those systems which are relevant to consider when evaluating the electronic structure of the current tpe frameworks: (1) high-energy pyrrole-based electrons reduce the bound metal ion with *n* e^-, leaving *n* holes on the ligand platform (i.e., $(L^0)M^{2+} \rightarrow (L^{n+})M^{2-n}$); (2) the ligand and metal 3*d* orbitals are close enough in energy such that spin-state tautomerism is possible;[24] and (3) no intramolecular redox occurs, leaving each metal in the divalent state and the ligand in a fully reduced, closed-shell configuration.

Scenario 1: If scenario 1 was operative we would anticipate a stepwise elongation of the pyrrole subunits within the tpe framework across the 3*d* series from oxidation of the ligand framework. No ligand metrical perturbations to suggest this are apparent when comparing the structural data for complexes **2**→**6**. In addition, the UV-vis absorption spectra do not

(23) (a) Albright, T. A.; Burdett, J. K.; Whangbo, M.-H. *Orbital Interactions in Chemistry*. John Wiley & Sons, Inc: New York; 1985, pp 381-389. (b) Detrich, J. L.; Konečnỳ, R.; Vetter, W. M.; Doren, D.; Rheingold, A. L.; Theopold, K. H. *J. Am. Chem. Soc.* **1996**, *118*, 1703-1712.

(24) Storr, T.; Verma, P.; Pratt, R. C.; Wasinger, E. C.; Shimazaki, Y.; Stack, T. D. P. *J. Am. Chem. Soc.* **2008**, *130*, 15448-15459.

reveal any readily assignable ligand-to-metal charge-transfer bands that would suggest the presence of excited states consistent with this scenario. The only absorption band of appropriate intensity ($\lambda \approx 320$nm, $\varepsilon > 10^4$ M^{-1} cm^{-1}) corresponds to a ligand-to-ligand charge transfer band that is present in the deprotonated ligand (tpe)Li_3 (λ_{max}: 313 nm, ε: 9000 M^{-1} cm^{-1}). Furthermore, calculations on the oxidation product of **6** ((tpe)Zn(py), **8**) provides an estimate of the energetic cost in excess of 2 eV ($\Delta E = E_{tot}(\mathbf{6}) - E_{tot}(\mathbf{8})$) towards oxidation of the tpe framework, suggesting an intramolecular redox transfer should be energetically disfavored.

Scenario 2: Each of the complexes from Mn (**2**) to Ni (**5**) feature high-spin configurations which are evident by the low temperature X-ray diffraction studies (193K), low temperature Mössbauer for **3** and **7**, and the room temperature solution magnetic moment determinations for complexes **2**-**5** (**Table 2.3**). This is especially notable for M = Ni (**5**), which in the dipyrromethane system is found to be square planar and diamagnetic.[9] The DFT spin density analyses of **2-5** suggest that all spin is localized on the corresponding 3*d* ion without significant contribution from the ligand (Figure 2.9). These data imply that no spin-state tautomerism is occurring. If the oxidation of the tpe framework is as energetically disfavored as estimated by DFT, this suggests a considerable barrier for spin-state tautomerism.

Scenario 3: Based on the evidence we have collected, we have determined that metal complexes of the tpe trianion fall into scenario 3 where the available redox reservoirs (i.e., tpe, 3*d* metal ion) are well separated and do not show any evidence for intramolecular redox transfer in the outer-sphere electron transfer reactions, as also observed in the

dipyrromethane system we previously reported.[9] This feature is most obvious in the electrochemical behavior of complexes **2**-**6**, both in the cyclic and differential pulse voltammetry experiments (Figure 2.3), which suggest that the $[(tpe)M(py)]^-$ species traverse a similar oxidation pathway regardless of the metal ion present or its spin-multiplicity. The commonality of the electrochemical oxidations, EPR on the oxidation product of **6** and the DFT results indicate the kinetic products of the one-electron oxidation reactions are ligand-centered radicals, rather than metal-centered oxidations (Equation 1):

$$[(tpe)M^{II}(py)]^- \xrightarrow{-e^-} [(tpe^{\bullet+})M^{II}(py)] \xrightarrow[+\,L]{\textit{H-atom abstraction}} [(\kappa^2\text{-}tpe)M^{II}(py)(L)] \quad (1)$$

Both cyclic and differential pulse voltammetry exhibit multiple oxidation events following the primary oxidation highlighted in Figure 2.3. Unlike the dipyrromethane analogues previously reported, we do not observe the multi-electron redox events attributable to a one electron oxidation of each of the pyrrolide subunits. The primary, irreversible oxidation of the $[(tpe)M(py)]^-$ anions produces a dipyrromethane-like product $(\kappa^2\text{-}tpe)M(py)(L)$ following H-atom abstraction from the $(tpe^{\bullet+})M(py)$ intermediate. The onset of oxidation for the dipyrromethane complexes of the formulation $(^{Mes}dpma)M(py)_2$ does not occur until -240 mV (vs. Fc/Fc^+).[9] Thus the secondary redox event for the $[(tpe)M(py)]^-$ anions is not anticipated to occur until a similar potential, separated from the initial oxidation by nearly 450 mV.

Chemical oxidation of both **3** and **6** initially produce highly colored intermediates consistent with the decreased HOMO-LUMO gap predicted for the oxidized products by DFT. The rapidity with which the unshielded tpe ligand radical abstracts $H^\bullet$ from solvent to produce the $(\kappa^2\text{-}tpe)M(py)(L)$ species (L = pyridine or solvent) prevented isolation of the

putative (tpe$^{\bullet+}$)M^{II}(py) oxidation product. The resulting coordination change at the metal accounts for the irreversibility of the cyclic voltammetry experiments. Attempted metallation of the tpe trianion with Fe^{III} sources leads to formation of the same κ^2 species in **7**. While we cannot definitively rule out intramolecular electron transfer from the tpe to Fe^{III} following ligation, the tpe trianion is a strong enough reductant to reduce the Fe^{III} precursor, and this process likely precedes halide metathesis. Extending our analysis of these observations to the dipyrromethane system, the ligand-centered oxidation processes we observed likely produced pyrrole-dissociated species, making identification of chemically oxidized materials impossible.[9]

The orbital analysis (Figure 2.7) for the tpe complexes shows that the energetically most accessible orbital density is localized on the tpe scaffold. The frontier orbitals consist entirely of the pyrrolide π-system. As shown by Floriani[5a] and Odom,[7c] more electrophilic, early transition metal complexes bind pyrrolide subunits through an η^5 π-association preferentially to terminal *N*-ligation, even in porphyrinogen complexes. For iron-porphyrinogens,[5c] these same π-electrons cause an intimate coupling between the metal and ligand oxidation states when orbitals of appropriate π-symmetry are allowed to mix, but become a liability due to their energetic accessibility when this conjugation is broken.[9] For dipyrromethane and tris(pyrrolyl)ethane systems, the highest-lying ligand orbitals do not feature any π-density on the pyrrole N, making the ligands poor candidates to function as π-donors to metals that could function as π-acceptors. This property, coupled with the high-spin, pseudo-tetrahedral nature of the dipyrromethane and tris(pyrrolyl)ethane complexes, functions to make the pyrrolide and 3*d* ions completely decoupled redox

entities. This does not rule out the two redox reservoirs engaging in cooperative redox transfer in oxidations involving 2 or more electrons, a process which plays a key role in stabilizing the high-valent ferryl species in cytochrome P450[25] and potentially in related tris(pyrrolyl)amine systems.[26] Work is currently underway to determine the ability of $[(tpe)ML_n]^-$ anions to function as atom or group transfer accepting platforms via metal-centered redox chemistry without being short-circuited by intramolecular redox transfer.

2-4. Conclusions

We have investigated transition metal complexes of the tris(pyrollyl)ethane ligand and found them to exhibit unusual electronic properties attributable to the pyrrolide ligand framework. Electrochemical investigations on the $[(tpe)M^{II}(py)]^-$ series reveal a common irreversible oxidation pathway that is entirely ligand-based, invariant to the divalent metal bound. This observation indicates that fully-populated, ligand-based π orbitals from the tpe construct are energetically most accessible, akin to their dipyrromethane analogues. DFT calculations on the anions suggest electrons pair preferentially in the higher-energy, delocalized ligand π-orbitals rather than pairing within the lower-energy metal-ion 3*d* orbitals (e.g., in the event of an intramolecular redox transfer). This can be attributed to larger electron-pairing energy costs for the metal-based 3*d* orbitals. While the energetic overlap between the tpe ligand-based π orbitals and the *d*-orbital manifold is favorable for cooperative redox, the two redox reservoirs display totally disparate redox behavior. A major criterion for coupling ligand and transition metal redox is to have a pathway by

(25) Shaik, S.; Kumar, D.; De Visser, S. P.; Altun, A.; Thiel, W. *Chem. Rev*. **2005**, *105*, 2279-2328 and references therein.

(26) Harman, W. H.; Chang, C. J. *J. Am. Chem. Soc.* **2007**, *129*, 15128-15129.

which the two reservoirs can communicate, typically through conjugation of the ligand π-orbital with *d*-orbitals of appropriate symmetry. DFT studies reveal the tpe platform, and by extension the dipyrromethane ligand systems, do not feature frontier π-orbital density on the ligand *N* termini, shielding the ligand-based, highest occupied molecular orbitals from conjugation with the metal 3*d* orbitals. As a result, the ligand redox behavior observed is devoid of transition metal influence. In the context of outer-sphere electron transfer chemistry, the pyrrolic π-electrons become a liability to the complex stability. These ligand platforms, however, could find significant utility in the stabilization of inner-sphere electron transfer reactivity and the resulting high-oxidation state metal complexes if L→M π contribution can be maximized.

2-5. Experimental Section

All manipulations were carried out in the absence of water and dioxygen using standard Schlenk techniques, or in an MBraun inert atmosphere drybox under a dinitrogen atmosphere. All glassware was oven dried for a minimum of 1 h and cooled in an evacuated antechamber prior to use in the drybox. Benzene, diethyl ether, dichloromethane, *n*-hexane, tetrahydrofuran and toluene were dried and deoxygenated on a Glass Contour System (SG Water USA, Nashua, NH) and stored over 4 Å molecular sieves (Strem) prior to use. Benzene-d_6 was purchased from Cambridge Isotope Labs and degassed and stored over 4 Å molecular sieves prior to use. Pyridinium *p*-toluenesulfonate, ferrocenium hexafluorophosphate, dihydroanthracene and anhydrous pyridine were purchased from Aldrich and used as received. Anhydrous manganese(II), iron(II), cobalt(II), and nickel(II) chlorides were purchased from Strem and used as received. Phenyllithium was prepared

by lithiation of iodobenzene with *n*-butyllithium. 2-(2,4,6-trimethylphenyl)-1H-pyrrole was synthesized according to literature procedures.[27] Metal precursors $MCl_2(py)_2$ (M = Mn, Fe, Co, Ni) were synthesized based on literature procedure.[14,28] Celite® 545 (J. T. Baker), silica gel 32-63 μ (Dynamic Adsorbents, Atlanta, GA), 4 Å molecular sieves, tetra-*n*-butylammonium hexafluorophosphate (Alfa Aesar) and zinc chloride (Aldrich) were dried in a Schlenk flask for 24 h under dynamic vacuum while heating to at least 150 °C.

Characterization and Physical Measurements. UV/Visible spectra were recorded on a Varian Cary 50 UV/Visible spectra, with a scan rate of 300 nm/min. NIR spectra were recorded on a Varian Cary model 5000 UV-vis-NIR spectrophotometer. ^1H and ^{13}C NMR spectra were recorded on Varian Mercury 400 MHz or Varian Unity/Inova 500 MHz spectrometers. ^1H and ^{13}C NMR chemical shifts are reported relative to $SiMe_4$ using the chemical shift of residual solvent peaks as reference. Solution magnetic susceptibilities were determined by Evans's method[13] using hexamethyldisiloxane as an internal reference. Mass spectrometry was performed at the Harvard University FAS Center for Systems Biology Mass Spectrometry and Proteomics Resource Laboratory on an Agilent 6210 TOF LC/MS with a dual nebulizer ESI source. Elemental Analyses were carried out at Complete Analysis Labs, Inc. (Parsippany, NJ).

Electrochemical experiments were carried out using a CH Instruments CHI660C Electrochemical Workstation. The electrolyte used was 0.3 M $(^nBu_4N)(PF_6)$ in THF. The concentration of all analytes was 3 mM. The working electrode was glassy carbon, a platinum wire was used as the counter electrode, and non-aqueous Ag/Ag^+ reference

(27) Rieth, R.; Mankad, N.; Calimano, E.; Sadighi, J. *Org. Lett.* **2004,** *6*, 3981-3983.
(28) Allan, J. R.; Brown, D. H.; Nuttall, R. H.; Sharp, D. W. A. *J. Chem. Soc. A,* **1966**, 1031-1034.

electrodes (10 mM $AgNO_3$ in THF) were used with the corresponding electrolyte solution. Cyclic voltammetry was performed with a scan rate between 500 mV/s and 25 mV/s.

X-band EPR spectroscopic measurements were performed using a Bruker EMX spectrometer equipped with 13 inch magnets, an ER 4102ST cavity, and a Gunn diode microwave source. Samples in a toluene glass were cooled using a liquid nitrogen cold finger dewar. Simulation and fitting of EPR data was done with the EasySpin 3.0.0[29] ToolBox for MATLAB® R2008a.[30] ^{57}Fe Mössbauer spectra were measured with a constant acceleration spectrometer (SEE Co, Minneapolis, MN). Isomer shifts are quoted relative to Fe metal at room temperature. Data was analyzed and simulated with Igor Pro 6 software (WaveMetrics, Portland, OR) using Lorentzian fitting functions.

X-Ray Crystallography Procedures. All structures were collected on either a Siemens or Bruker three-circle platform goniometer equipped with either a Bruker Apex I or Apex II CCD and an Oxford cryostream cooling device. Radiation was from a graphite fine focus sealed tube Mo Kα (0.71073 Å) source. Crystals were mounted on a cryoloop using Paratone-*N* oil. Structures were collected at 193 K (**2-6)**, and 100 K (**7**). Data was collected as a series of φ and/or ω scans. Data was integrated using SAINT (Bruker AXS) and scaled with a multi-scan absorption correction using SADABS (Bruker AXS) The structures were solved by direct methods or Patterson maps using SHELXS-97[31] and refined against F^2 on all data by full matrix least squares with SHELXL-97. All non-hydrogen atoms were refined anisotropically. Hydrogen atoms were placed at idealized positions and refined using a

(29) Stoll, S.; Schweiger, A. *J. Magn. Reson.* **2006**, *178*, 42-55.
(30) The MathWorks™, MATLAB R2008a (2008), Natick, MA.
(31) (a) Sheldrick, G. M. *Acta Cryst.* **1990,** *A46*, 467-473. (b) Sheldrick, G. M. *SHELX-97,* University of Göttingen, Göttingen, Germany, **1997**.

riding model. The isotropic displacement parameters of all hydrogen atoms were fixed to 1.2 times the *U* value of the atoms they are linked to (1.5 times for methyl groups). In all structures with a Li^+ counter-cation, the ligated solvent THF and ether often exhibited positional disorder and similarity restraints were used to refine the model. Except in certain cases (as noted below) the major component of the disordered THF refined to between 54% and 95%. Further details on several structures are noted below. **Note on 2:** Similarity restraints and distance and angle restraints were insufficient for refinement of residual electron density, most likely a heavily disordered free THF molecule, found in the crystal structure. The SQUEEZE function of PLATON[32] was used to remove the electron density. Details can be found in the .cif file for the structure of **2**. **Note on 5:** The pyridine bound to nickel exhibited positional disorder, which was modeled using similarity and flat restraints. The major component refined to 90%. **Notes on 6:** One THF-ligated to Li^+ was modeled using three positional disorders, with components of 40%, 37% and 23%, again using similarity restraints to aid in refinement. In addition, a free THF molecule was disordered over two positions and refined with the aid of similarity restraints, with the major contributor refining to 55%. **Note on 7:** The hydrogen atom bound to the nitrogen of the free pyrrole arm was explicitly located as a Q peak in the refinement and refined semi-freely using restraints.

5,5',5''-(ethane-1,1,1-triyl)tris(2-mesityl-1H-pyrrole) (H_3tpe) (1): A 100 mL bomb flask was charged with 2-(2,4,6-trimethylphenyl)-1H-pyrrole (3.468 g, 18.72 mmol), trimethylorthoacetate (1.194g, 9.94 mmol), and 20 mL of CH_2Cl_2. After stirring for 5 min,

(32) http://web.mit.edu/platon_v40505/platon/docs/platon/pl000000.html

pyridinium *p*-toluenesulfonate (0.170 g, 0.675 mmol) was added resulting in a color change from tan to magenta. The reaction was stirred at 55°C for 41 h. Additional pyridinium *p*-toluenesulfonate (0.168 g, 0.668 mmol) was added, and the reaction was stirred at 50°C for an additional 72h. The reaction mixture was then filtered through a silica gel plug, washing with excess CH_2Cl_2 (~50 mL). Solvent and volatiles were removed *in vacuo*, and the resulting green-brown, sticky solid was redissolved in minimal CH_2Cl_2. Hexanes were added until a precipitate was observed, and the solution was placed into the freezer for 2h. The precipitate was collected on a glass frit. The recrystallization procedure was repeated twice, affording **1** as an off-white powder (2.5204 g, 70%). ^{1}H NMR (300 MHz, C_6D_6): δ/ppm 7.33 (br s, 3 H), 6.82 (s, 6 H), 6.17 (t, *J* = 3.2 Hz, 3 H), 6.05 (t, *J* = 2.9 Hz, 3 H), 2.19 (s, 9 H), 2.16 (s, 16 H), 1.81 (s, 3 H). ^{13}C {^{1}H} NMR (125 MHz, C_6D_6): δ/ppm 138.8, 137.7, 136.7, 131.8, 129.9, 128.8, 108.5, 107.1, 41.3, 28.5, 21.5, 21.2. HRMS (ESI^+) *m/z* for $C_{41}H_{46}N_3^+$ $[M+H]^+$: Calc. 580.36915, Found 580.36933.

$[(tpe)Mn(py)]^-[Li(THF)_4]^+$ (2): In separate 20 mL scintillation vials, **1** (448 mg, 0.772 mmol) and PhLi (202 mg, 2.413 mmol) were each dissolved in 3 mL of THF and cooled in a −35°C freezer. The cold solution of **1** was added to the PhLi solution and stirred at room temperature for 30 minutes. In another 20 mL vial $MnCl_2(py)_2$ (220 mg, 0.775 mmol) was slurried in 3 mL of THF with ~0.5 mL pyridine. The vials containing deprotonated **1** and $MnCl_2(py)_2$ were placed in a liquid nitrogen cooled cold well until frozen. The solution of **1** was thawed and added to the stirring slurry of $MnCl_2(py)_2$. The reaction mixture became a yellow solution as it warmed. The reaction was stirred at room temperature overnight.

Removal of the solvent *in vacuo* gave a dark yellow residue. The residue was extracted into 5 mL of benzene and filtered through a Celite plug to remove lithium chloride. Removal of the solvent *in vacuo* gave a yellow powder (522.4 mg, 67%). Crystals suitable for X-ray diffraction were grown from a vapor diffusion of Et_2O into a THF solution of **2** at room temperature. The compound gave no signal by ^1H NMR. UV/vis (THF) λ_{max}/nm ($\varepsilon/M^{-1}cm^{-1}$): 331 (11000), 502 (140), 477 (110). μ_{eff} (C_6D_6, 295 K) 6.2(1) μ_B. Comb. Anal. for $[C_{46}H_{47}MnN_4]^-[LiC_{16}H_{32}O_4]^+$: Calc: C, 74.01; H, 7.91; N, 5.57; Found: C 73.93, H 7.74, N 5.46.

$[(tpe)Fe(py)]^-[Li(THF)_4]^+$ (3): In separate 20 mL scintillation vials, **1** (246.2 mg, 0.425 mmol) and PhLi (114 mg, 1.36 mmol) were each dissolved in 3 mL of THF and cooled in a −35°C freezer. The cold solution of **1** was added to the PhLi solution and stirred at room temperature for 30 minutes. In another 20 mL vial $FeCl_2(py)_2$ (121.3 mg, 0.426 mmol) was slurried in 3 mL of THF. The vials containing deprotonated **1** and $FeCl_2(py)_2$ were placed in a liquid nitrogen cooled cold well until frozen. The solution of **1** was thawed and added to the stirring slurry of $FeCl_2(py)_2$. The reaction mixture became a dark red solution as it warmed. The reaction was stirred at room temperature overnight. Removal of the solvent *in vacuo* gave an orange residue, which was extracted with Et_2O. The Et_2O solution was filtered over Celite, approximately 20 drops of THF were added, and a precipitate formed. The bright orange solid **3** was collected on a glass frit (0.445 g, 103% yield due to remaining Et_2O). Crystals suitable for X-ray diffraction were grown from a vapor diffusion of Et_2O into a THF solution of **3** at room temperature. ^1H NMR (500 MHz, C_6D_6) δ/ppm

151.71 (s), 77.68 (s), 71.94 (s), 30.47 (s), 15.19 (s), 9.76 (s), 4.16 (s), 1.65 (s), 1.07 (s), 0.32 (s), −6.72 (br s). UV/vis (THF) λ_{max}/nm (ε/$M^{-1}cm^{-1}$): 317 (16000), 516 (1100), 560 (920, sh), 1636 (250), 1911 (180, sh). μ_{eff} (C_6D_6, 295 K) 5.1(1) μ_B. Comb. Anal. for $[C_{46}H_{47}FeN_4]^-[LiC_{16}H_{32}O_4]^+$: Calc: C, 73.94; H, 7.91; N, 5.55; Found: C, 73.80; H, 7.81; N, 5.79.

$[(tpe)Co(py)]^-[Li(THF)_4]^+$ (4): In separate 20 mL scintillation vials, **1** (482 mg, 0.831 mmol) and PhLi (220 mg, 2.61 mmol) were each dissolved in 3 mL of THF and cooled in a −35°C freezer. The cold solution of **1** was added to the PhLi solution and stirred at room temperature for 30 minutes. In another 20 mL vial $CoCl_2(py)_2$ (241 mg, 0.835 mmol) was slurried in 3 mL of THF. The vials containing deprotonated **1** and $CoCl_2(py)_2$ were placed in a liquid nitrogen-cooled cold well until frozen. The solution of **1** was thawed and added to the stirring slurry of $CoCl_2(py)_2$. The reaction mixture became a very dark purple-blue solution as it warmed. The reaction was stirred at room temperature 3h. Removal of the solvent *in vacuo* gave a black-blue residue, which was dissolved in benzene. The benzene solution was filtered over Celite and lyophilized. The resulting dark blue solid was dissolved in Et_2O, 10 drops THF was added, and the solution was cooled to −35°C. A dark blue precipitate, **4**, formed and was collected on a glass frit (0.581 g, 69% yield). Crystals suitable for X-ray diffraction were grown from a vapor diffusion of hexanes into a THF solution of **4** at room temperature. ^{1}H NMR (500 MHz, CD_2Cl_2): δ/ppm 165.25 (s), 93.99 (s), 46.56 (s), 24.55 (s), 7.04 (br s), 6.51 (s), 5.97 (s), 3.86 (s), 1.55 (s), 1.17 (s), −4.38 (s). UV/vis (THF) λ_{max}/nm (ε/$M^{-1}cm^{-1}$): 325 (12000), 550 (850), 621 (730), 650 (860), 998

(200), 1250 (90, sh). μ_{eff} (C_6D_6, 295 K) 4.84(5) μ_B. Comb. Anal. for $[C_{46}H_{47}CoN_4]^-[LiC_{16}H_{32}O_4]^+$: Calc: C, 73.72; H, 7.88; N, 5.55; Found: C 73.61, H 7.78, N 5.62.

[(tpe)Ni(py)]$^-$[Li(THF)$_4$]$^+$ (5): In separate 20 mL scintillation vials, **1** (27.9 mg, 0.0481 mmol) and PhLi (12.9 mg, 0.154 mmol) were each dissolved in 3 mL of THF and cooled in a −35°C freezer. The cold solution of **1** was added to the PhLi solution and stirred at room temperature for 30 minutes. In another 20 mL vial $NiCl_2(py)_2$ (14.4 mg, 0.0500 mmol) was slurried in 3 mL of THF with ~0.5 mL pyridine. The vials containing deprotonated **1** and $NiCl_2(py)_2$ were placed in a liquid nitrogen-cooled cold well until frozen. The solution of **1** was thawed and added to the stirring slurry of $NiCl_2(py)_2$. The reaction mixture became a green solution as it warmed. The reaction was stirred at room temperature overnight. Removal of the solvent *in vacuo* gave a dark grey residue. The residue was extracted into 5 mL of benzene and filtered through a Celite plug to remove lithium chloride. Removal of the solvent *in vacuo* gave a grey powder (37.0 mg, 76%). Crystals suitable for X-ray diffraction were grown from a vapor diffusion of hexanes into a THF solution of **5** at room temperature. ^{1}H NMR (500 MHz, C_6D_6): δ/ppm 118.62 (br s), 109.37 (s), 43.39 (s), 27.73 (s), 13.97 (s), 6.27 (s), 5.76 (s), 3.24 (s), 1.78 (s), 1.27 (s), −1.36 (s). UV/vis (THF) λ_{max}/nm (ε/$M^{-1}cm^{-1}$): 319 (13000), 398 (1500, sh), 504 (500, sh), 631 (570), 800 (120), 928 (60). μ_{eff} (C_6D_6, 295 K) 2.91(5) μ_B. Comb. Anal. for $[C_{46}H_{47}NiN_4]^-[LiC_{16}H_{32}O_4]^+$: Calc: C, 73.73; H, 7.88; N, 5.55; Found: C, 73.67; H, 7.72; N, 5.65.

[(tpe)Zn(py)]$^-$[Li(THF)$_4$]$^+$ (6): In separate 20 mL scintillation vials, **1** (0.288 g, 0.497 mmol) and PhLi (130 mg, 1.54 mmol) were each dissolved in 3 mL of THF and cooled in a −35°C freezer. The cold solution of **1** was added to the PhLi solution and stirred at room temperature for 30 minutes. In another 20 mL vial $ZnCl_2$ (70 mg, 0.51 mmol) was slurried in 3 mL of THF with ~0.5 mL pyridine. The vials containing deprotonated **1** and $ZnCl_2$ were placed in a liquid nitrogen cooled cold well until frozen. The solution of **1** was thawed and added to the stirring slurry of $ZnCl_2$. The reaction mixture became a bright yellow solution as it warmed. The reaction was stirred at room temperature 3 h. Removal of the solvent *in vacuo* gave a dark yellow residue. The residue was extracted into 5 mL of benzene and filtered through a Celite plug to remove lithium chloride and lyophilized. The resultant bright yellow powder was dissolved in Et_2O, 10 drops THF was added, and the solution was cooled to −35°C. A yellow precipitate, **6,** formed and was collected on a glass frit (0.234 g). The filtrate was dried *in vacuo*, dissolved in Et_2O and THF was added. A second crop of **6** was collected (32 mg; total yield 266 mg, 55%). Crystals suitable for X-ray diffraction were grown from a solution of **6** in a 1:1 mixture of Et_2O and THF solution with 10 drops of TMEDA at −35°C. ^{1}H NMR (500 MHz, C_6D_6): δ/ppm 6.70-6.68 (m, 2H, *o*-C_5H_5N), 6.61-6.58 (m, 4H, *p*-C_5H_5N, pyrrole C-*H*), 6.53 (s, 6H, −$C_6H_2(CH_3)_3$), 6.24 (br s, 3H, pyrrole C-*H*), 6.17-6.14 (m, 2H, *m*-C_5H_5N), 3.46 (m, 12H, $Li(OCH_2(CH_2)_2CH_2)_4$), 2.67 (s, 3H, $(CH_3)C(C_5H_2MesN)_3$), 2.15 (s, 18H, *o*-$C_6H_2(CH_3)_3$), 2.02 (s, 9H, *p*-$C_6H_2(CH_3)_3$), 1.35 (m, 12H, $Li(OCH_2(CH_2)_2CH_2)_4$). ^{13}C NMR (101MHz , C_6D_6) δ/ppm 149.3, 146.9, 138.4, 137.9, 136.5, 135.3, 124.3, 106.7, 102.5, 68.4, 43.3, 26.0, 22.0, 21.3. MS (ESI$^-$) *m/z* $C_{46}H_{47}N_4Zn^-$ [M]$^-$: Calc: 719.3, Found: 719.3 (observed isotope pattern matches predicted isotope pattern).

(tpeH)Fe(py)$_2$ (7): A thawing 3 mL THF solution of **1** (67.3 mg, 0.12 mmol) was added to solid LiN(TMS)$_2$ (38.6 mg, 0.23 mmol) and stirred 1.5 h at room temperature, during which time the solution turned from clear pale yellow to clear magenta. This solution was frozen in a liquid nitrogen cooled cold well. $FeCl_2(py)_2$ (33.1 mg, 0.12 mmol) was slurried in 5 mL THF and frozen. The thawing solution of deprotonated **1** was added to the thawing slurry, rinsing with room temperature THF, and was stirred for 4 hours. Solvent was removed *in vacuo* and the resulting residue was dissolved in Et_2O and filtered through a Celite plug. Volatiles were removed *in vacuo*, affording **7** (29.5 mg, 32%) as an orange-yellow powder. A sample containing 134.0 mg of **7** was analyzed by Mössbauer spectroscopy. Crystals suitable for X-ray diffraction were grown from an Et_2O solution of **7**. ^{1}H NMR (500 MHz, C_6D_6): δ/ppm 114.86, 100.30, 41.18, 34.46, 28.77, 24.87, 12.09, 9.99, 6.95, 5.20, 2.39, 1.43, −0.68, −8.40, −16.46. Comb. Anal. for $C_{51}H_{53}FeN_5$: Calc: C, 77.36; H, 6.75; N, 8.84; Found: C, 77.24; H, 6.67; N, 8.73.

Procedure for Oxidation of [(tpe)Fe(py)]$^-$[Li(THF)$_4$]$^+$. A solution of **3** (100.4 mg, 0.0997 mmol) in 5 mL toluene was cooled to −40°C in an acetonitrile/dry ice cooled cold well. The solution of **3** was added to cold, solid ferrocenium hexafluorophosphate (33 mg, 0.10 mmol) and stirred at −40°C for 2 hours. The solution was allowed to warm to room temperature and stirred overnight. Toluene was removed *in vacuo* and approximately 2.5 mL benzene was added. The solution was frozen and lyophilized, then triturated in hexane and collected and dried on a glass frit. The resultant powder (74.4 mg) was analyzed by

Mössbauer spectroscopy. X-ray quality crystals formed from an Et_2O solution stored at −35°C. The major product was identified as **7** by comparison with an authentic sample as prepared above.

Procedure for Oxidation of $[(tpe)Zn(py)]^-[Li(THF)_4]^+$ and EPR Sample Preparation. A sample of **6** (18.7mg, 0.0184 mmol) was dissolved in 5 mL toluene and cooled in an acetonitrile/dry ice cooled cold well (−40°C). The toluene solution was added to cooled solid ferrocenium hexafluorophosphate (6.1 mg, 0.018 mmol) and stirred at −40°C for 2 hours. A sample of the reaction mixture was added to a cooled EPR tube and frozen into a glass in liquid nitrogen.

Computational Methods. The electronic structures of **2-6** were examined using *Gaussian 03*.[33] Geometry optimizations were performed using the atomic coordinates of the crystal structures as a starting point. Removal of the mesityl methyl groups resulted in collapse of the ligand structure, and thus no truncations to the ligand system were made. No symmetry was imposed upon the molecules. All optimizations were carried out unrestricted with the M05-2X[2] hybrid functional, as the B3LYP[3] functional was insufficient for estimating the ligand π-stacking effects. The 6-31G Pople basis set[16] was used for all structures, and "tight" convergence criteria were employed. In cases where the SCF failed to converge to the "tight" criteria, more reliable but more computationally expensive

(33) Frisch, M. J.; et al. *Gaussian 03*, Revision E.01, Gaussian, Inc., Wallingford CT, **2004**.

quadratic convergence was employed. The zinc structure was optimized as a singlet, and the remaining paramagnetic systems were optimized with multiplicities based on their magnetic moments from solution NMR determination (Evans' Method[7]: Mn – sextet, Fe – quintet, Co – quartet, Ni – Triplet). Intermediate-spin calculations were also performed, but the high-spin structures were of lower energy in all cases. Single point population analyses were carried out on the optimized structures using the unrestricted B3LYP functional with "tight" convergence criteria for all complexes. The TZV(P) basis set[18] was used for transition metal atoms and the atoms within the first coordination sphere (all nitrogen), and SV(P) basis set[19] for all other main group atoms. The singlet $[(tpe)Zn(py)]^-$ structure optimization and population analysis calculations were performed using both restricted and unrestricted functionals, and the difference in energy was found to be negligible.

Spin density plots and molecular orbital pictures were generated from *Gaussian* cube files using Visual Molecular Dynamics 1.8.6.[34] and rendered using POV-Ray v3.6 for Windows.[35] Orbital parentage from Mulliken Population calculations were tabulated using *QMForge*.[36]

(34) Humphrey, W.; Dalke, A.; Schulten, K. "VMD - Visual Molecular Dynamics," *J. Molec. Graphics* **1996**, *14*, 33.

(35) *Persistence of Vision Raytracer (v3.6)*, Persistence of Vision Pty. Ltd., Williamstown, Victoria, Australia, **2004**.

(36) Tenderholt, Adam L. *QMForge*, Version 2.1. Stanford University, Stanford, CA, USA.

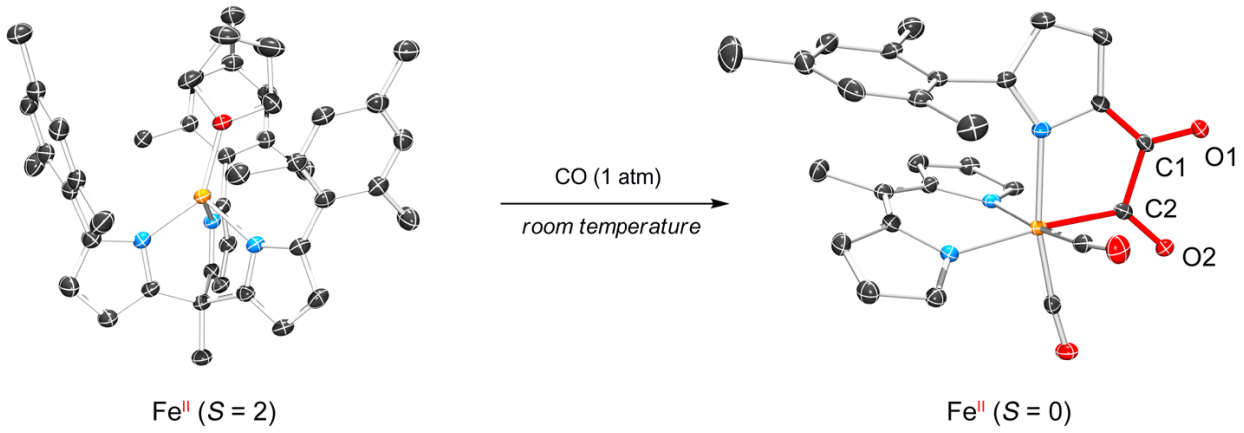

Chapter 3: Reductive coupling of CO templated by iron bound to the tris(pyrrolide)ethane scaffold[1]

3-1. Introduction

The reduction of CO to form C–C bonds is one of the two key steps involved in the Fischer-Tropsch (FT) process, in which a heterogeneous catalyst combines CO and H_2 to produce long-chain hydrocarbons.[2] Few homogeneous examples of FT-relevant transformations are known, but have provided insight into key challenges associated with FT chemistry: formation of C–C bonds from reduced carbonyl species, C–H bond formation from metal-coordinated CO, and the role of exogenous Lewis-acids in promoting CO reduction. The first reports of facile C–C coupling from metal-carbonyl species arose from carbene coupling following hydride or alkyl insertion into early transition metal or

(1) This chapter was adapted with permission from Sazama, G. T.; Betley, T. A. *Organometallics* **2011**, *30*, 4315–4319. Copyright 2011 American Chemical Society.
(2) Khodakov, Y.; Chu, W.; Fongarland, P. *Chem. Rev.* **2007**, *107*, 1692.

lanthanide carbonyls,[3,4] or by alkali reduction of metal carbonyl species followed by electrophilic trapping.[5] These reactions require the preparation of highly reducing transition metal hydride species or utilize alkali metal reductants (e.g. Na) to achieve carbonyl reduction. Two recent examples of FT relevant chemistry employ the formation of strong early transition-metal-oxygen bonds as a driving force to cleave the C-O bond and form new C-C bonds.[6] Moving away from strongly reducing early transition metal hydride or alkyl precursors, reductive coupling of metal carbonyls on a Re-based coordination complex was recently reported using a Lewis-acidic, pendant borane to facilitate carbonyl activation via hydride insertion.[7] From these precedents, a desirable reaction sequence would employ coordination complexes that template the construction of C–C bonds from carbonyl ligands without requiring strong chemical reductants. In this vein, we have

(3) (a) Manriquez, J. M.; McAlister, D. R.; Sanner, R. D.; Bercaw, J. E. *J. Am. Chem. Soc.* **1976**, *98*, 6733. (b) Calderazzo, F. *Angew. Chem., Int. Ed.* **1977**, *16*, 299. (c) Fachinetti, G.; Floriani, C.; Roselli, A.; Pucci, S. *J. Chem. Soc., Chem. Commun.* **1978**, 269. (d) Labinger, J. A.; Wong, K. S.; Scheidt, R. *J. Am. Chem. Soc.* **1978**, *100*, 3254. (e) Wood, C. D.; Schrock, R. R. *J. Am. Chem. Soc.* **1979**, *101*, 5421. (f) Wolczanski, P. T.; Bercaw, J. E. *Acc. Chem. Res.* **1980**, *13*, 121. (g) Barger, P. T.; Santarsiero, B. D.; Armantrout, R.; Bercaw, J. E. *J. Am. Chem. Soc.* **1984**, *106*, 5178. (h) Erker, G. *Acc. Chem. Res.* **1984**, *17*, 103. (i) Toreki, R.; LaPointe, R. E.; Wolczanski, P. T. *J. Am. Chem. Soc.* **1987**, *109*, 7558. (j) Hofmann, P.; Stauffert, P.; Frede, M.; Tatsumi, K. *Chem. Ber.* **1989**, *122*, 1559. (k) Miller, R. L.; Toreki, R.; LaPointe, R. E.; Wolczanski, P. T.; Van Duyne, G. D.; Roe, D. C. *J. Am. Chem. Soc.* **1993**, *115*, 5570. (l) Wolczanski, P. T. *Polyhedron* **1995**, *14*, 3335.

(4) (a) Manriquez, J. M.; Fagan, P. J.; Marks, T. J.; Day, C. S.; Day, V. W. *J. Am. Chem. Soc.* **1978**, *100*, 7112. (b) Marks, T. J. *Prog. Inorg. Chem.* **1979**, *25*, 224. (c) Fagan, P. J.; Manriquez, J. M.; Marks, T. J. In "Organometallics of the f-Elements"; Marks, T. J.; Fischer, R. D.; Eds.; Reidel Publishing Co.: Dordrecht, Holland, 1979, Ch. 4. (d) Fagan, P. J.; Manriquez, J. M.; Marks, T. J.; Day, V. W.; Vollmer, S. H.; Day, C. S. *J. Am. Chem. Soc.* **1980**, *102*, 5393. (e) Katahira, D. A.; Moloy, K. G.; Marks, T. J. *Organometallics* **1982**, *1*, 1723.

(5) (a) Lam, C. T.; Corfield, P. W. R.; Lippard, S. J. *J. Am. Chem. Soc*., **1976**, *21*, 91. (b) Bianconi, P. A.; Williams, I. D.; Engeler, M. P.; Lippard, S. J. *J. Am. Chem. Soc.* **1986**, *108*, 311. (c) Bianconi, P. A.; Vrtis, R. N.; Rao, Ch. P.; Williams, I. D.; Engeler, M. P.; Lippard, S. J. *Organometallics* **1987**, *6*, 1968. (d) Carnahan, E. M.; Protasiewicz, J. D.; Lippard, S. J. *Acc. Chem. Res.* **1993**, *26*, 90.

(6) (a) Matsuo, T.; Kawaguchi, H. *J. Am. Chem. Soc.*, **2005** *127* , 17198. (b) Shima, T.; Hou, Z. *J. Am. Chem. Soc.*, **2006**, *128*, 8124.

(7) (a) Miller, A. J. M.; Labinger, J. A.; Bercaw, J. E. *J. Am. Chem. Soc.* **2008**, *130*, 11874. (b) Miller, A. J. M.; Labinger, J. A.; Bercaw, J. E. *J. Am. Chem. Soc.* **2010**, *132*, 3301. (c) Miller, A. J. M.; Labinger, J. A.; Bercaw, J. E. *Organometallics* **2010**, *29*, 4499.

investigated the reactivity of the electron-rich [(^{Mes}tpe)Fe]$^-$ anion towards carbonyl and isocyanide substrates, leading to a metal-templated reductive coupling of CO initiated by the ligand framework.[8]

3-2. Results and Discussion

Formation of [(^{Mes}tpe)Fe(THF)][Li(THF)$_4$] (**1**), is accomplished by deprotonation of the (^{Mes}tpe)H$_3$ ligand using base (LiN(SiMe$_3$)$_2$, 3.05 equiv.) in THF followed by subsequent addition to a thawing slurry of divalent iron chloride in THF (Scheme 3.1 (a); THF = tetrahydrofuran). Recrystallization from THF and hexane affords a pale brown-yellow powder in 72% yield. The ^{1}H NMR spectrum reveals **1** to be paramagnetic (solution magnetic moment = 5.56(5) μ_B consistent with a spin-only value of S = 2),[9] with ten proton resonances apparent ranging from δ 80 to −6 ppm. The zero-field ^{57}Fe Mössbauer spectrum (δ = 0.85 $^{mm}/_s$, $|\Delta E_Q|$ = 2.55 $^{mm}/_s$) gives parameters consistent with a high-spin formulation for **1** that are very similar to the previously reported pyridine adduct, [(^{Mes}tpe)Fe(py)]$^-$.[8] X-ray diffraction quality crystals can be obtained from a THF-hexane solution stored for two weeks at −35°C. The crystal structure (Figure 3.1) shows the tpe ligand bound κ^3 to the Fe center (Fe–N distances: 2.005(3), 2.028(3), and 2.033(3) Å) with one THF molecule occupying a fourth coordination site (Fe–O bond length = 2.023(2) Å).[10] The Fe-bound THF

(8) Sazama, G. T.; Betley, T. A. *Inorg. Chem.* **2010**, *49*, 2512.
(9) Evans, D. F. *J. Chem. Soc.* **1959**, 2003.
(10) Compound **1**: $C_{61}H_{82}FeLiN_3O_5$, M_r = 1000.09, monoclinic, P2(1)/c, a = 13.875(5), b = 24.856(9), c = 15.973(6) Å, α = 90°, β = 94.945(8)°, γ = 90°, V = 5488(3) Å^3, Z = 4, ρ_{calcd} = 1.210 Mg/m^3, μ = 0.326 mm^{-1}, $R1(I>2\sigma(I))$ = 0.0630, $wR2$ = 0.1508, GOF = 1.107. Compound **2:** $C_{69}H_{86}FeLiN_6O$, M_r = 1078.23, triclinic, P-1, a = 10.7409(7), b = 12.5697(8), c = 23.8076(15) Å, α = 88.352(4)°, β = 84.975(4)°, γ = 72.407(4)°, V = 3052.1(3) Å^3, Z = 2, ρ_{calcd} = 1.173 Mg/m^3, μ = 0.294 mm^{-1}, $R1$ ($I>2\sigma(I)$) = 0.0536, $wR2$ = 0.1113, GOF = 1.016. Compound **3**: $C_{47}H_{57}Fe_3N_6P_3$, M_r = 966.45, monoclinic, C2/c, a = 25.163(4), b = 10.6991(16), c = 34.829(5) Å, α = 90°, β = 90.582(3)°, γ = 90°, V = 9376(2) Å^3, Z = 8, ρ_{calcd} = 1.278

molecule is parallel to two mesityl fragments and canted away from the third, and thus does not fall on the molecular-C_3 axis (defined by the vector containing the tpe ligand bridgehead and the Fe center), giving an overall pseudo-tetrahedral geometry at iron. A similar deviation from C_3 symmetry was also observed in the reported pyridine complexes, however in the pyridine complexes this can be attributed to a significant π-stacking interaction with a ligand mesityl unit not present in the THF complex.[8]

Mg/m^3, μ = 0.374 mm^{-1}, $R1(I>2\sigma(I))$=0.0566, $wR2$ = 0.1159, GOF = 1.035. CCDC-788652 (**1**), 788653 (**2**), 788654 (**3**) contain the supplementary crystallographic data for this paper. These data can be obtained free of charge from the Cambridge Crystallographic Data Centre via www.ccdc.cam.ac.uk/data_request/cif.

Scheme 3.1

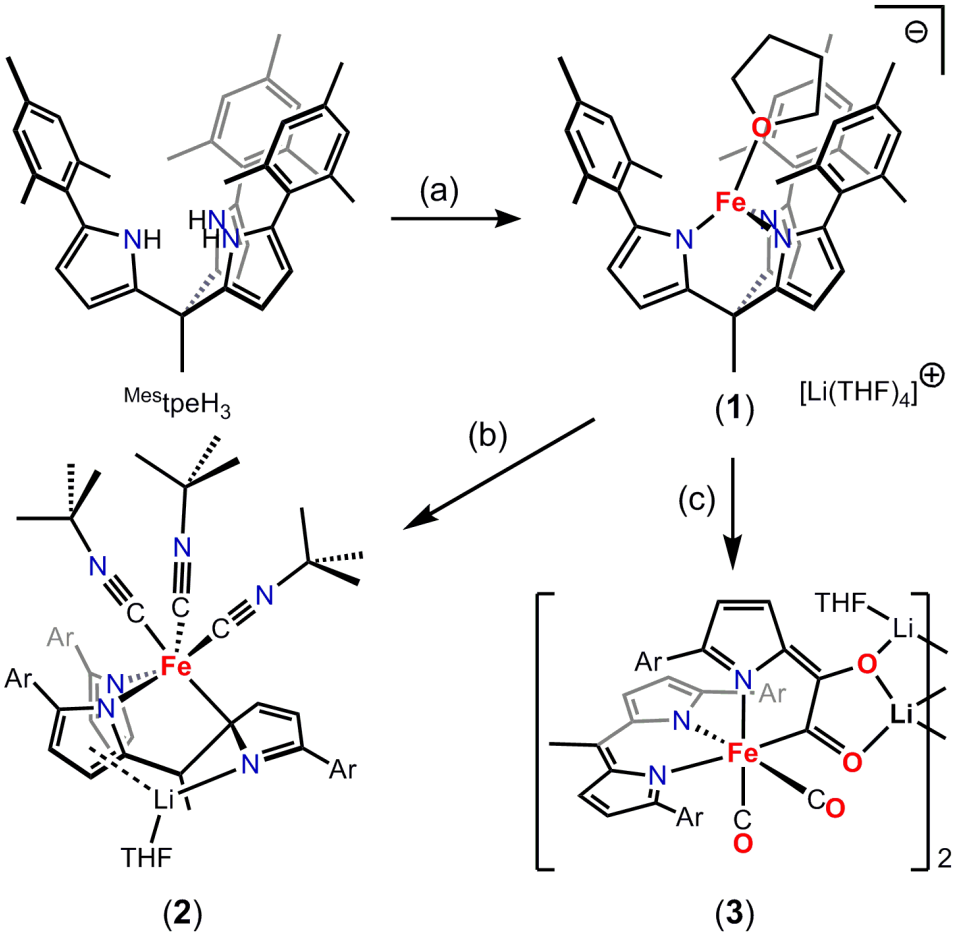

Reaction conditions: (a) 1. $LiN(SiMe_3)_2$ (3.05 eq.), THF, 25 ºC, 1.5 h; 2. $FeCl_2$ (1.1 eq.), thawing THF, 3h; (b) ^{t}BuNC (3.3 eq.), benzene, 25 ºC; (c) CO gas (1 atm), benzene, 25 ºC.

Reaction of **1** with *t*-butylisocyanide (^{t}BuNC, 3.3 eq) at room temperature in benzene immediately resulted in the precipitation of a bright orange powder (92% yield, Scheme 3.1(b)). The product, [(^{Mes}tpe)Fe(CN^{t}Bu)$_3$]Li(THF) (**2**) was sparingly soluble in benzene, but saturated solutions of **2** in C_6D_6 were sufficient for obtaining assignable ^{1}H NMR spectra. The ^{1}H NMR spectrum of **2** revealed a diamagnetic species, which was reflected in the marked shift of the spectral parameters obtained for **2** in the ^{57}Fe Mössbauer spectrum

(δ = 0.12 $^{mm}/_{s}$, $|\Delta E_Q|$ = 0.47 $^{mm}/_{s}$). The significant decrease in isomer shift results from a spin-state change (from S = 2 for **1** to S = 0 for **2**) and back-bonding from Fe to three π-acidic isonitrile ligands. The large decrease observed in the quadrupole splitting is likewise attributable to the change in spin-state, wherein the asymmetric population of the e set in the approximately tetrahedral **1** ($(e)^3(t_2)^3$) changes to the electronically symmetric, octahedral coordination in **2** $(t_{2g})^6(e_g)^0$.

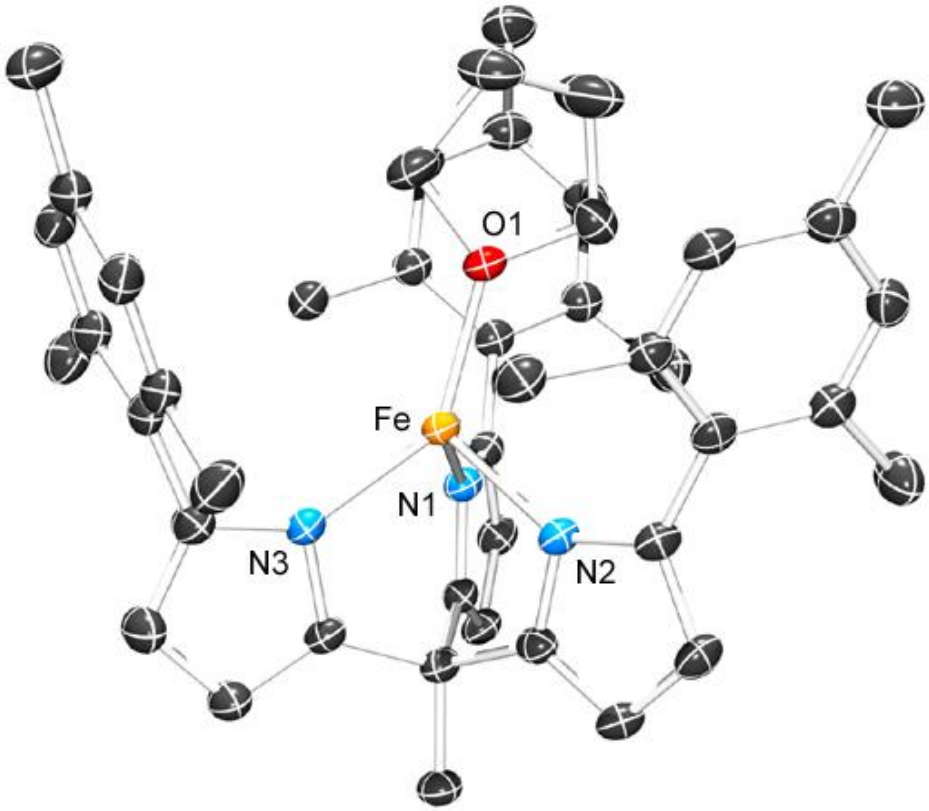

Figure 3.1. Solid-state molecular structure for [(^{Mes}tpe)Fe(THF)]$^-$ (**1**), (thermal ellipsoids shown at 50% probability and hydrogens and THF-bound lithium counterion omitted for clarity). Selected bond lengths (Å) and angles (°): Fe–N1 2.033(3); Fe–N2 2.028(3); Fe–N3 2.005(3); Fe–O 2.023(2); N1-Fe-N2 93.93(11); N1-Fe-N3 95.39(11); N2-Fe-N3 95.37(11)

Large, translucent, deep-red crystals of X-ray diffraction quality of **2** grew from saturated benzene solutions standing overnight at room temperature under an inert atmosphere. The X-ray diffraction crystal structure of **2** shows three bound isonitrile molecules (see Figure

3.2). The isonitrile C-N distances are between 1.162(3)-1.166(3) Å and a strong, broad FTIR absorbance ($\nu_{C\text{-}N}$) was observed at 2093 cm^{-1} (free isonitrile $\nu_{C\text{-}N}$ = 2137 cm^{-1}), indicative of weak π-backbonding from the high-spin iron (II). Most striking about the structure of **2** is the observed tautomerization of one pyrrolide unit, resulting in pyrrole *C*-ligation to Fe (Fe1–C30, 2.253(2) Å) and the now imino nitrogen (N3–C33: 1.333(3) Å, consistent with a C=N formulation) bound to lithium (N3–Li: 2.253(2) Å). The lithium cation is bound η^5 to a neighboring pyrrolide unit (C/N–Li distances range from 2.250(4) – 2.578(4) Å) and one molecule of THF. The pyrrole *C*-ligation to iron produces a bond contraction of 0.035 Å of two backbone-pyrrole bonds (C2-C10 and C2-C20, from 1.536(5) and 1.537(5) Å in **1** to 1.499(3) and 1.504(3) Å in **2**). This change suggests a strengthening of the pyrrole–backbone connection with two pyrroles, providing evidence that this mode of ligation is intermediate between the *N*,*N*,*N*-ligation and a dipyrromethene. The change in (^{Mes}tpe) ligand hapticity from *N*,*N*,*N*-ligation to *N*,*N*,*C*-ligation likely arises from the inability of the (^{Mes}tpe) to accommodate the three large isocyanide ligands. While the steric pressure caused by binding of the three *t*-butylisocyanide ligands is apparent from viewing the space-filling model of **2** (see Figure 3.3), a more subtle effect is consideration of the (^{Mes}tpe) trianion to enable octahedral coordination of the bound metal ion. The three N-Fe-N bond angles in high-spin **1** range from 93.93(11) to 95.39(11)°, but expand to an average of 96.05(7) in the diamagnetic [(^{Mes}tpe)Zn(py)]$^-$ anion.[0] Upon tautomerizing in **2** to the *N*,*N*,*C*-ligation, the (^{Mes}tpe) bond angles decrease (N1-Fe-N2 87.82(7), N1-Fe-C30 79.31(7), N2-Fe-C30 78.62(7)). This change in binding mode provides a greater volume to accommodate the three linear *t*-butylisocyanide ligands, facilitating the octahedral coordination at iron in **2**.

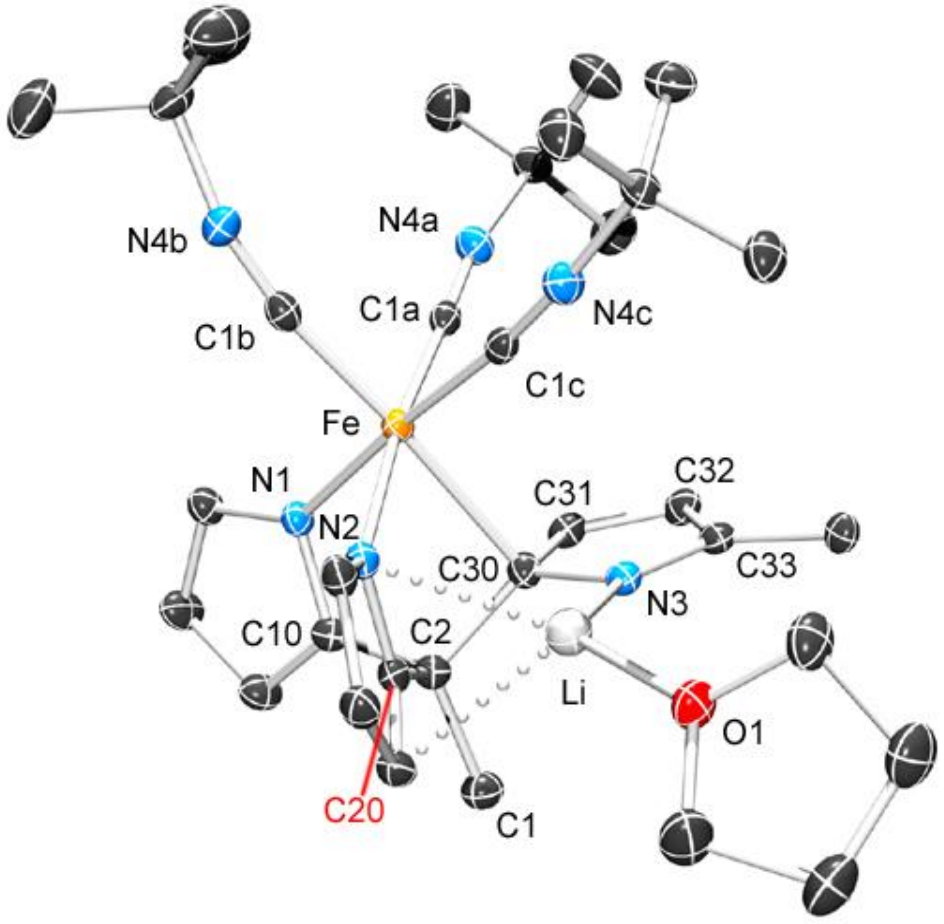

Figure 3.2. Solid-state molecular structure of [(*N*,*N*,*C*–^{Mes}tpe)Fe(CN^{t}Bu)$_3$]Li(THF) (**2**, thermal ellipsoids shown at 50% probability and hydrogens and mesityl groups omitted for clarity)**.** Selected bond lengths (Å) and angles (°) for **2**: Fe1–N1: 2.0180(16); Fe1–N2: 2.0538(17); Fe1–C30: 2.2531(19); C1a–N4a: 1.166(3); C1b–N4b: 1.166(3); C1c–N4c: 1.162(3); N3–C30: 1.421(3); C30–C31: 1.433(3); C31–C32: 1.376(3); C32–C33: 1.430(3); C33–N3: 1.333(3); C2–C10: 1.499(3); C2–C20: 1.504(3); C2–C30: 1.548(3); N1-Fe-N2 87.82(7), N1-Fe-C30 79.31(7), N2-Fe-C30 78.62(7). Dihedral angle C10–C2–C1–C20: 122.36°.

Exposure of **1** to one atmosphere of CO gas affords a markedly different product from **2** which is soluble in most organic solvents (Scheme 3.1 (c)). ^{1}H and ^{13}C NMR (C_6D_6 solution) and Mössbauer spectra of this product represent a clean diamagnetic material, with desymmetrization of the ligand environment apparent by ^{1}H NMR. FTIR spectroscopy

reveals four absorption bands at 1960, 1816, 1528, and 1480 cm^{-1}, where the first two are likely assignable to the C–O stretches of terminally bound carbonyl ligands (free CO ν_{CO} = 2143 cm^{-1}). The latter two stretching frequencies are consistent with ketone-like functionalities. The Mössbauer parameters obtained for **3** (δ = 0.06 $^{mm}/_{s}$ and $|\Delta E_Q|$ = 1.20 $^{mm}/_{s}$) are similar to those obtained for **2**. The low isomer shift (relative to that obtained for **1**, 0.85 $^{mm}/_{s}$) reflects a likely spin-state change analogous to that observed in **2**, with the addition of π-backbonding to CO ligands. Changes in the quadrupole splitting, while less pronounced than in **2**, again reflect a change from high-spin to low-spin Fe^{2+}.

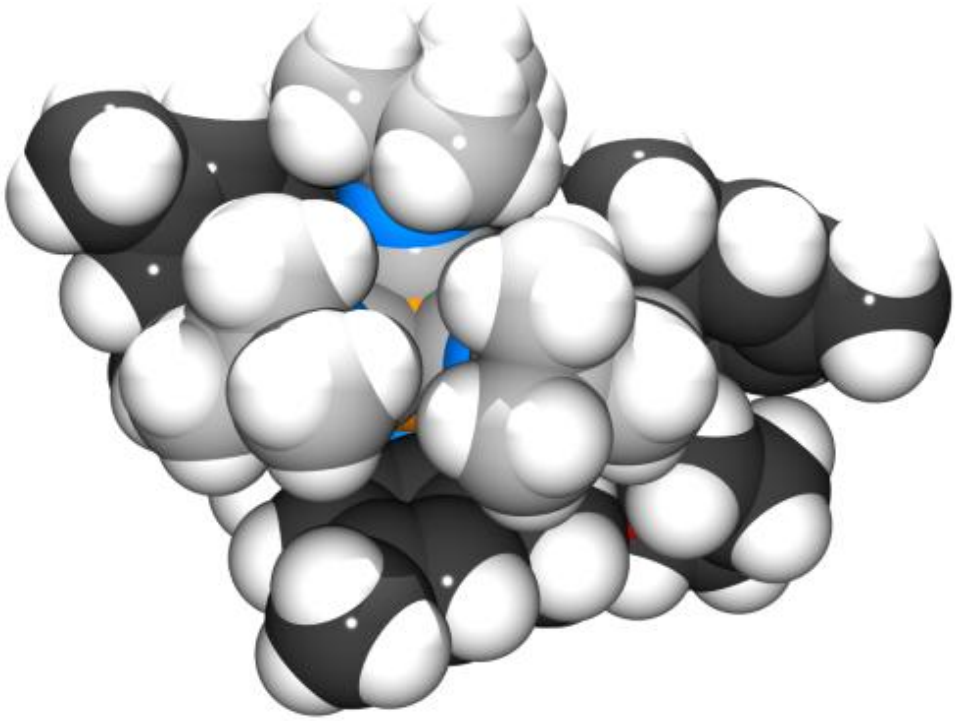

Figure 3.3. Space filling model of **2** where the 3 ^{t}BuNC carbon atoms are colored gray, and the (^{Mes}tpe) ligand carbon atoms are colored black.

Crystals suitable for X-ray crystallography can be grown from a C_6D_6 solution after standing for two weeks at room temperature under one atmosphere of CO. The crystal structure reveals that the product $\{[(^{Mes}dpme)Fe(CO)_2(^{Mes}NC_4H_2{-}C(O)C(O))]Li\}_2$ (**3**, Figure 3.4), is a dimer of mononuclear iron complexes in which the tpe ligand has undergone oxidative fragmentation to form a dipyrromethene fragment [11] and a separate, dicarbonylated pyrrole unit. The pyrrole unit has nucleophilically coupled two reactant CO molecules, forming a bidentate, oxalyl-imino moiety, giving rise to the two lower carbonyl stretching frequencies observed in the IR spectrum of **3**. The two mononuclear Fe complexes are bridged via lithium cations bound to the two oxalato-oxygens (O3 and O4 in Figure 3.4), with a crystallographic C_2 symmetry axis through the lithium atoms. Two molecules of THF complete the coordination sphere for the lithium bridging via only one oxalato oxygen (see full structure, available in SI). Bond lengths suggest an imino formulation of the pyrrole nitrogen (N3–C34 = 1.339(3) Å, consistent with a C–N double bond). This fragment contains π-bonds conjugated through the pyrrole-oxalyl fragment (see Scheme 3.1, **3**), terminating in an acyl carbon bound to iron (Fe1–C29 = 1.948(3) Å). The two unfunctionalized bound CO molecules display C–O bond lengths of 1.144(3) and 1.150(3) Å, similar to lengths seen for other low-spin Fe^{2+} dicarbonyl complexes reported in the literature.[12]

(11) King, E. R.; Betley, T. A. *Inorg. Chem.* **2009**, *48*, 2361.

(12) (a) Bart, S. C.; Chłopek, K.; Bill, E.; Bouwkamp, M. W.; Lobkovsky, E.; Neese, F.; Wieghardt, K.; Chirik, P. J. *J. Am. Chem. Soc.* **2006**, *128*, 13901. (b) Vendemiati, B.; Prini, G.; Meetsma, A.; Hessen, B.; Teuben, J. H.; Traverso, O. *Eur. J. Inorg. Chem.* **2001**, *2001*, 707.

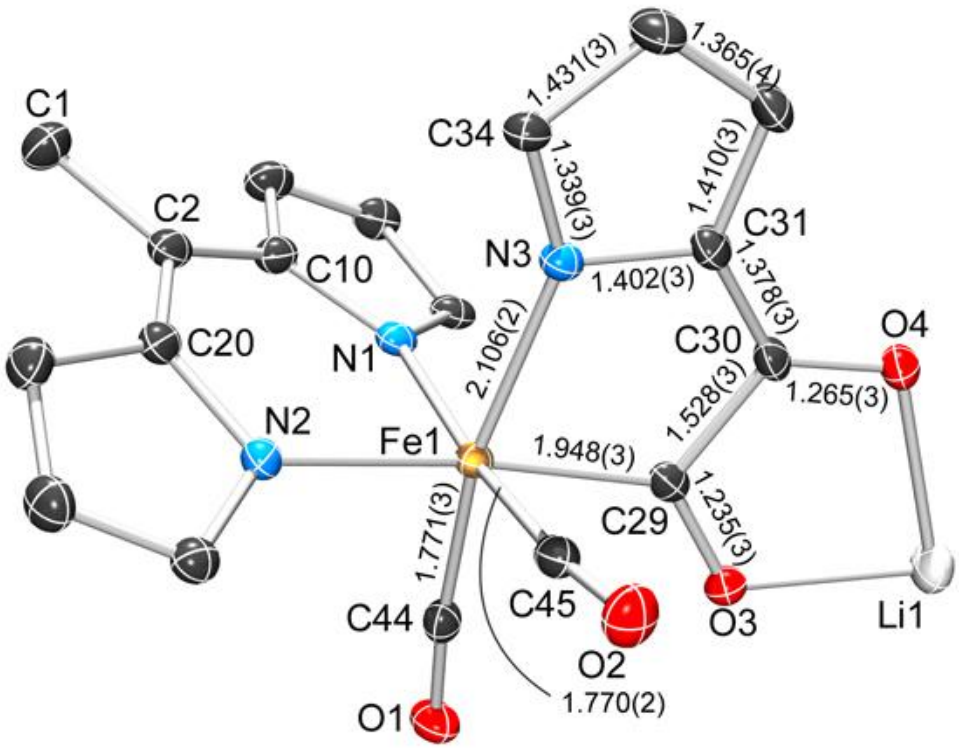

Figure 3.4. Solid-state molecular structure of one half of the dimeric structure for {[(Mesdpme)Fe(CO)$_2$(MesNC$_4$H$_2$–C(O)C(O))]Li}$_2$ (**3**) (thermal ellipsoids shown at 50% probability, hydrogens, mesityl groups, one bridging lithium and solvent molecules omitted for clarity). Selected bond lengths (Å) for **3**: Fe1–N1: 2.0267(17); Fe1–N2: 2.0823(17). N1–Fe1–N2 bond angle: 88.31(7)°. Dihedral angle C10–C2–C1–C20: 173.36°.

The information obtained from the crystal structure data for complexes **2** and **3** allow us to propose a reaction mechanism for the formation of **3** from **1** (Scheme 3.2). We propose that upon coordination of 3 equivalents of CO, **1** initially forms a tautomer intermediate analogous to the structure of **2** (Scheme 3.2, **2a**). The nucleophilic carbon-bound pyrrole subunit migrates to a bound carbonyl to form a four-membered aza-metallacyclobutene (**2b**).[13] The enolate-like structure of proposed intermediate **2b** migrates to a second bound carbonyl forming an α,β-diketo-azametallacyclopentane (**2c**), presumably to relieve steric

(13) Although we cannot rule out the formation of a metallocyclopropane followed by tautomerization, this transformation seems unlikely to occur due to the steric constraints of the Mestpe ligand.

strain from the aza-metallacyclobutene intermediate **2b**, which subsequently undergoes tautomerization to form the thermodynamically stable imino-acyl dimer product **3**. The steric bulk of the *t*-butylisocyanide ligands in **2** likely prevents the formation of C–C coupled product akin to **3**,[14] arresting the above reaction sequence at the ligand tautomer **2**.

Scheme 3.2. Proposed mechanism of CO reductive coupling reaction.

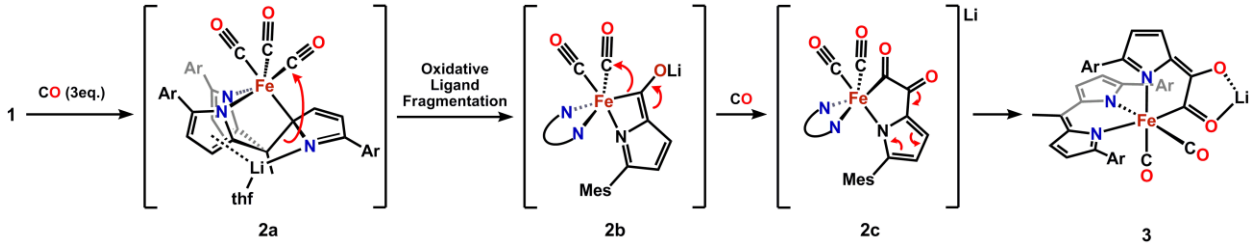

The proposed mechanism necessitates a closer inspection of the role of lithium in the reductive coupling process. Given the precedent for Lewis-acid activation of CO,[7,15,16] the lithium cation could bind and activate a bound CO toward nucleophilic attack. In opposition to this, however, the CO coupling reaction proceeds even in THF solutions, which should sequester the Li^+ and preclude Lewis-acid activation of a CO ligand. Alternatively, the presence of Li^+ may facilitate the formation of tautomer **2a**, priming the nucleophile for the observed reductive coupling. Substitution of the lithium for bulky, non-coordinating

(14) Berg, F. J.; Petersen, J. L. *Organometallics* **1991**, *10*, 1599.

(15) (a) Butts, S. B.; Holt, E. M.; Strauss, S. H.; Alcock, N. W.; Stimson, R. E.; Shriver, D. F. *J. Am. Chem. Soc.* **1979**, *101*, 5864. (b) Collman, J. P.; Finke, R. G.; Cawse, J. N.; Brauman, J. I. *J. Am. Chem. Soc.* **1978**, *100*, 4766.

(16) (a) Wong, A.; Atwood, J. D. *J. Organomet. Chem.* **1980**, *199*, C9. (b) Wong, A.; Atwood, J. D. *J. Organomet. Chem.* **1981**, *210*, 395. (c) Okazaki, M.; Ohtani, T.; Inomata, S.; Tagaki, N.; Ogino, H. *J. Am. Chem. Soc.* **1998**, *120*, 9135.

cations (e.g PPh_4^+, $[Ph_3P{=}N{=}PPh_3]^+$) results in highly insoluble species, but further examination may yet still elucidate the role of lithium in the coupling process.

3-3. Conclusion

We have observed the reductive coupling of two CO ligands under mild reaction conditions (1 atm of CO), without the use of strong exogenous reducing agents.[16] The hapticity change of the (^{Mes}tpe) trianion facilitates coordination environment changes at the metal ion, where *N*,*N*,*N*-ligation is preferred for tetrahedral complexes and *N*,*N*,*C*-ligation stabilizes an octahedral field preferentially. The facile interchange of the ligand coordination mode generates a metal-bound nucleophile to trigger migration to a metal bound carbonyl, giving rise to CO-reduction with concomitant (^{Mes}tpe) oxidative fragmentation in the absence of an alkali metal reductant. A second carbonyl coupling is likely facilitated by the strained four-membered azametallacycle formed via the initial carbonyl insertion, where incorporation of a second equivalent of CO results in a more stabilized five-membered oxalyl-imino pyrrole product. The results presented herein allude to more general reactions based on a ligand platform similar to that found in the final product and employing extant nucleophiles; this possibility is especially appealing given our group's concurrent research into the chemistry of dipyrromethene complexes. We are currently pursuing further investigation of generalization of this reactivity.

3-4. Experimental

All manipulations were carried out in the absence of water and dioxygen using standard Schlenk techniques, or in an MBraun inert atmosphere drybox under a dinitrogen

atmosphere. All glassware was oven dried for a minimum of 1 h and cooled in an evacuated antechamber prior to use in the drybox. Benzene, diethyl ether, *n*-hexane, tetrahydrofuran and toluene were dried and deoxygenated on a Glass Contour System (SG Water USA, Nashua, NH) and stored over 4 Å molecular sieves (Strem) prior to use. Benzene-d_6 was purchased from Cambridge Isotope Labs and degassed and stored over 4 Å molecular sieves prior to use. Pyridinium *p*-toluenesulfonate, ferrocenium hexafluorophosphate, dihydroanthracene and anhydrous pyridine were purchased from Aldrich and used as received. Anhydrous iron(II) chloride was purchased from Strem and used as received. Celite® 545 (J. T. Baker) and 4 Å molecular sieves were dried in either a Schlenk flask or a vacuum oven for 24 h under dynamic vacuum while heating to at least 150 °C.

Characterization and Physical Measurements. ^{1}H and ^{13}C NMR spectra were recorded on Varian Mercury 400 MHz or Varian Unity/Inova 500 MHz spectrometers. ^{1}H and ^{13}C NMR chemical shifts are reported relative to residual solvent peaks as reference. Elemental Analyses were carried out at Complete Analysis Labs, Inc. (Parsippany, NJ).

^{57}Fe Mössbauer spectra were measured with a constant acceleration spectrometer (SEE Co, Minneapolis, MN). Isomer shifts are quoted relative to Fe metal at room temperature. Data was analyzed and simulated with Igor Pro 6 software (WaveMetrics, Portland, OR) using Lorentzian fitting functions.

X-Ray Crystallography Procedures. All structures were collected on a Bruker three-circle platform goniometer equipped with either a Bruker Apex I or Apex II CCD and an Oxford cryostream cooling device. Radiation was from a graphite fine focus sealed tube Mo Kα (0.71073 Å) source. Crystals were mounted on a cryoloop using Paratone-*N* oil. All structures

were collected at 100 K. Data was collected as a series of φ and/or ω scans. Data was integrated using SAINT (Bruker AXS) and scaled with a multi-scan absorption correction using SADABS (Bruker AXS).[17] The structures were solved by direct methods or Patterson maps using SHELXS-97[18] and refined against F^2 on all data by full matrix least squares with SHELXL-97. All non-hydrogen atoms were refined anisotropically. Hydrogen atoms were placed at idealized positions and refined using a riding model. The isotropic displacement parameters of all hydrogen atoms were fixed to 1.2 times the *U* value of the atoms they are linked to (1.5 times for methyl groups). Further details on several structures are noted below. **Note on 2:** The structure of **2** contained a Li-bound THF which exhibited positional disorder. No restraints were necessary to refine the model. The major component of the disordered THF refined to 75%. **Note on 3:** A free benzene solvent molecule was disordered over two positions and refined with the aid of similarity restraints, with the major contributor refining to 68%. **Notes on 4:** The structure of **4** contained a Li-bound THF which exhibited positional disorder. EADP, SIMU and DELU restraints were used to refine the model, and the two parts refined to 50% each.

[(tpe)Fe(THF)][Li(THF)$_4$] (1): In separate 20 mL scintillation vials, tris(pyrrolyl)ethane (^{Mes}tpeH$_3$, 0.635 g, 1.10 mmol) and Li(N(SiMe$_3$)$_2$) (0.554 g, 3.31 mmol) were each dissolved in 4 mL of THF. The solution of Li(N(SiMe$_3$)$_2$) was added to the solution of tpeH$_3$ and stirred at room temperature for 1 hour. In another 20 mL vial FeCl$_2$ (0.166 g, 1.31 mmol) was slurried in 2 mL of THF. Both vials were placed in a liquid nitrogen cooled cold well until frozen. The ligand solution was thawed and added to the stirring slurry of FeCl$_2$. The reaction mixture became a translucent dark brown solution as it warmed. The reaction was

(17) Bruker AXS (2009). APEX II. Bruker AXS, Madison, Wisconsin.
(18) G.M. Sheldrick, (2008). Acta Cryst. A64, 112-122.

stirred at room temperature for 2 hours, after which removal of the solvent *in vacuo* gave a brown residue. The residue was extracted into 5 mL of diethyl ether and filtered through diatomaceous earth to remove lithium chloride. THF (5 drops) was added to the dark brown ether filtrate, and a yellow-brown precipitate (**1**) formed. The solution was cooled to −35°C overnight and the precipitate was collected on a medium fritted funnel. The solid was purified by precipitation from THF with hexane, and 0.729 g (72% yield) of yellow powder was collected and stored at −35°C. Crystals suitable for X-ray diffraction were grown from a mixture of THF and hexane at −35°C. ^{1}H NMR (400MHz, C_6D_6): δ/ppm: 78.84 (br. s.), 69.79 (br. s.), 48.22 (br. s.), 28.81 (br. s.), 26.69 (sh), 12.91 (br. s.), 4.10 (br. s.), 1.61 (br. s.), 1.02 (br.s.), -5.39 ppm (br. s.). Comb. Anal. for $[C_{45}H_{50}FeN_3O]^-[LiC_{16}H_{32}O_4]^+$: Calc: C, 73.25; H, 8.26; N, 4.20; Found: C, 73.19; H, 8.08; N, 4.31.

[(tpe)Fe(CN^{t}Bu)$_3$]Li(THF) (2): A benzene solution of *tert*-butyl isocyanide (28.3 mg, 0.340 mmol) was added to a benzene solution of **1** (103.7 mg, 0.1037 mmol) and stirred two hours at room temperature. A bright orange precipitate formed out of the dark red-orange solution and was collected and dried on a medium fritted funnel (91.4 mg, 92%). Crystals suitable for X-ray diffraction were grown from a solution of **2** in C_6D_6 at room temperature in an NMR tube. ^{1}H NMR (500 MHz, C_6D_6) δ/ppm 7.88 (d), 6.99 (s), 6.93 (s), 6.80 (m), 6.50 (s), 6.37 (s), 6.04 (s), 2.70 (s), 2.34 (m), 2.25 (s), 2.19 (s), 1.80 (s) 1.13 (s), 0.95 (s), 0.89 (s). Comb. Anal. for $C_{60}H_{77}FeLiN_6O$: Calc: C, 74.98; H, 8.08; N, 8.74; Found: C, 74.86; H, 8.01; N, 8.59.

[(dpme)Fe(COCOC$_4$H$_2$NMes)]$_2$[Li(THF)]$_2$ (3): A 100 mL recovery flask was charged with a 10 mL benzene solution of **1** (357.3 mg, 357.3 mmol) and sealed with a fresh rubber

septum under nitrogen. Carbon monoxide gas (35 mL at 1 atm, 1.43 mmol) was added via syringe to the flask and the reaction mixture was stirred for one hour at room temperature. The solution was frozen and lyophilized, and 343.2 mg dark red-brown powder was isolated. The resultant powder was purified by dissolving in hexane, filtering through diatomaceous earth to remove unreacted **1**, and collecting and evaporating the filtrate *in vacuo*, providing dark red-brown **3** as a powder. X-ray diffraction quality crystals were grown in saturated C_6D_6 solutions over a period of 2 weeks. ^{1}H NMR (500MHz, C_6D_6): δ/ppm: 7.38 (d, *J*=4.4 Hz, 1 H), 7.24 (br. s., 1 H), 7.03 (d, *J*=4.4 Hz, 2 H), 6.90 (br. s., 2 H), 6.75 (s, 1 H), 6.77 (s, 1 H), 6.51 (br. s., 1 H), 6.39 (d, *J*=3.9 Hz, 1 H), 6.27 (d, *J*=3.9 Hz, 1 H), 6.22 (d, *J*=4.4 Hz, 1 H), 3.53 (br. s., 9 H), 2.71 (s, 3 H), 2.40 (s, 3 H), 2.25 - 2.34 (m, 6 H), 2.13 - 2.24 (m, 9 H), 1.97 (s, 6 H), 1.80 (s, 3 H), 1.36 (br. s., 9 H). ^{13}C NMR (126MHz, C_6D_6) δ/ppm: 212.4, 211.8, 184.8, 171.3, 164.9, 163.2, 161.9, 149.2, 142.8, 142.1, 140.8, 139.2, 138.9, 138.2, 138.0, 137.5, 137.2, 136.8, 136.7, 136.4, 135.2, 130.1, 129.8, 129.3, 129.0, 128.9, 128.1, 127.9, 127.4, 124.8, 123.0, 120.3, 119.6, 68.5, 26.0, 22.9, 22.8, 22.2, 22.2, 22.1, 21.8, 21.7, 21.6, 21.5, 20.7, 3.0. Comb. anal. for $C_{49}H_{50}FeLiN_3O_5$: Calc: C, 71.45; H, 6.12; N, 5.10; Found: C, 71.33; H, 6.13; N, 5.19.

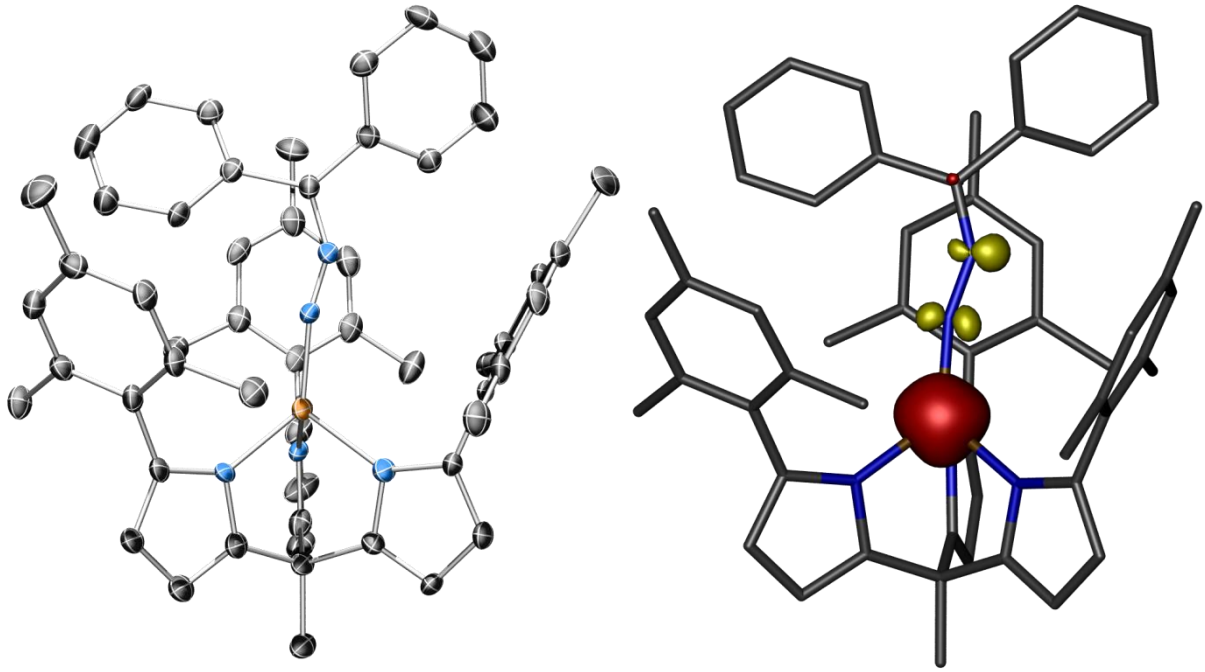

Chapter 4: Multiple, Disparate Redox Pathways Exhibited by a tris(pyrrolido)ethane Iron Complex

4-1. Introduction

Coordination complex mediated redox chemistry involves the addition or removal of electrons from accessible molecular orbitals. The bedrock of this discipline was established in the pioneering work by Taube and coworkers in the 1950s with the distinction between inner-sphere and outer-sphere electron transfer reactions.[1] In the 60 intervening years,

(1) (a) Taube, H.; Myers, H.; Rich, R. L. *J. Am. Chem. Soc.* **1953**, *75*, 4118. (b) Taube, H.; Gould, E. S. *Acc. Chem. Res.*, **1969**, *2*, 321. (c) Taube, H. *Science,* **1984**, *226*, 1028.

these two mechanisms continue to be satisfactory to describe the majority of redox behavior, but many developments have been made with regards to what molecular components are involved in redox chemistry. The suite of available redox-active moieties has been expanded from simple one-electron transfers to and from transition metals to include all the fragments of a given coordination complex, including the ligands and between metals in multinuclear complexes.

Molecular redox generally falls into one of the following categories, distinguished by the redox-active fragment(s). They are described below and in Scheme 4.1:

A. *Metal-localized redox with redox-inert ligands (Class I, Scheme 4.1a):* In this class, all oxidation and reduction events are localized on the transition metal, suggesting a large separation between transition metal and ligand-based frontier orbitals. For Class I complexes, changes in the d-orbital manifold of a given complex are readily observed spectroscopically, and thus were some of the first examples of well understood redox chemistry. Redox chemistry at the metal center can simply involve the gain or loss of electrons by outer-sphere or inner-sphere mechanisms,[1] or the inner-sphere redox chemistry can involve the making or breaking of substrate covalent bonds, as exemplified by oxidative addition and reductive elimination reactions. The prototypical example of this latter category is illustrated by oxidative addition of H_2 to Ir^{I} in Vaska's complex or the reductive elimination of H_2 from the Ir^{III} dihydride (Scheme 4.1a).[2] As illustrated by the following examples (class II–III), care must be taken to correlate formal redox assignment to spectroscopic measurements, as otherwise class I reactivity

(2) (a) Vaska, L.; DiLuzio, J. W. J. Am. Chem. Soc. 1962, 84, 679. (b) Johnson, C. E.; Eisenberg, R. *J. Am. Chem. Soc.* **1985**, *107*, 3148.

(transition metal-centered) may be invoked inappropriately when possible ligand redox is neglected.[3]

B. *Ligand-localized redox with redox-inert metals (Class II, Scheme 4.1b):* When the frontier orbitals of the coordination complex ligands are of sufficiently high energy (described as redox non-innocent), redox equivalents can be derived from both transition metal centers and the ligands themselves.[4] Class II complexes concern coordination complexes where redox equivalents are entirely localized on a ligand with minimal metal character contributing to the electroactive molecular orbital(s). The earliest examples of class II complexes include complexes of dithiolene ligands which may bind metals as closed-shell dianionic chelates or monoanionic radical anionic chelates.[5] Traversing an electron transfer series with Ni induces sequential ligand oxidations without a redox change of the bound Ni (*Scheme 4.1b*). The energetically high-lying dithiolate ligand π-electrons are accessible in this sequence of redox reactions and largely comprise the redox-accessible electron reservoir for their corresponding coordination complexes. Other common chelating ligands with delocalized π-electron systems (catecholates,[6] phenolate,[7] amido-phenolate,[3,8] and diimino-pyridine[9]) have been

(3) Chaudhuri, P.; Verani, C. N.; Bill, E.; Bothe, E.; Weyhermüller, T.; Wieghardt, K. *J. Am. Chem. Soc.* **2001**, *123*, 2213.
(4) Jørgensen, C. K. *Coord. Chem. Rev.* **1966**, *1*, 164.
(5) (a) Schrauzer, G. N.; Mayweg, V. *J. Am. Chem. Soc.* **1962**, *84*, 3221. (b) Gray, H. B.; Williams, R.; Bernal, I.; Billig, E. *J. Am. Chem. Soc.* **1962**, *84*, 3596. (c) Gray, H. B.; Billig, E. *J. Am. Chem. Soc.* **1963**, *85*, 2019. (d) Davison, A.; Edelstein, N.; Holm, R. H.; Maki, A. H. *Inorg. Chem.* **1963**, *2*, 1227. (e) Eisenberg, R.; Gray, H. B. *Inorg. Chem.* **2011**, *50*, 9741.
(6) (a) Haga, M.; Dodsworth, E. S.; Lever, A. B. P. *Inorg. Chem.* **1986**, *25*, 447. (b) Masui, H.; Lever, A. B. P.; Auburn, P. R. *Inorg. Chem.* **1991**, *30*, 2402.
(7) (a) Hockertz, J.; Steenken, S.; Wieghardt, K.; Hildebrandt, P. *J. Am. Chem. Soc.* **1993**, *115*, 11222. (k) Chaudhuri, P.; Hess, M.; Muller, J.; Hildenbrand, K.; Bill, E.; Weyhermüller, T.; Wieghardt, K. *J. Am. Chem. Soc.* **1999**, *121*, 9599.

shown to display similar ligand-based redox behavior. Recent work employing redox-neutral, d^0 tantalum bound to bis(phenoxide)amide ligands extends the use of redox-active ligands from stabilization of metal centers to chemical function, wherein the complexes undergo multi-electron processes with no observable change in the oxidation state of the bound metals.[10] Other examples include the use of non-d^0 transition metals with redox-active ligands to catalyze useful chemical transformations.[11]

C. *Redox delocalized over metal and ligand(s) (Class III, Scheme 4.1c):* Redox activity is not exclusively transition metal-mediated or ligand-borne, as multi-electron redox processes can be effected wherein multiple redox equivalents are stored on both the metal and the ligand. Successive redox events occur in the highest energy molecular orbitals, regardless of whether the orbitals are localized on the metal or ligand or delocalized across the whole molecule. Cytochrome P-450 is the paradigm for class III coordination complexes.[12,13] Initial binding of dioxygen

---

(8) (a) Herebian, D.; Bothe, E.; Bill, E.; Weyhermüller, T.; Wieghardt, K. *J. Am. Chem. Soc.* **2001**, *123*, 10012. (b) Blackmore, K. J.; Ziller, J. W.; Heyduk, A. F. *Inorg. Chem.* **2005**, *44*, 5559. (c) Haneline, M. R.; Heyduk, A. F. *J. Am. Chem. Soc.* **2006**, *128*, 8410. (d) Blackmore, K. J.; Lal, N.; Ziller, J. W.; Heyduk, A. F. *J. Am. Chem. Soc.* **2008**, *130*, 2728..

(9) (a) Bouwkamp, M. W.; Bowman, A. C.; Lobkovsky, E.; Chirik, P. J. *J. Am. Chem. Soc.* **2006**, *128*, 13340. (b) Bart, S. C.; Chlopek, K.; Bill, E.; Bouwkamp, M. W.; Lobkovsky, E.; Neese, F.; Wieghardt, K. *J. Am. Chem. Soc.* **2006**, *128*, 13901. (c) Bart, S. C.; Lobkovsky, E.; Bill, E.; Wieghardt, K.; Chirik, P. J. *Inorg. Chem.* **2007**, *46*, 7055.

(10) Zarkesh, R. A; Ziller, J. W.; Heyduk, A. F. *Angew. Chem. Int. Ed.* **2008**, *47*, 4715.

(11) (a) Small, B. L.; Brookhart, M. *J. Am. Chem. Soc.* **1998**, *120*, 7143. (b) Scarborough, C. C.; Sproules, S.; Weyhermüller, T.; DeBeer, S.; Wieghardt, K. *Inorg. Chem.* **2011**, *50*, 12446. (c) Lu, C. C.; DeBeer George, S.; Weyhermüller, T.; Bill, E.; Bothe, E.; Wieghardt, K. *Angew. Chem. Int. Ed.* **2008**, *47*, 6384. (d) Britovsek, G. J. P.; Gibson, V. C.; McTavish, S. J.; Solan, G. A.; White, A. J. P.; Williams, D. J.; Kimberley, B. S.; Maddox, P. J. *Chem. Comm.* **1998**, *311*, 849. (e) Smith, A. L.; Hardcastle, K. I.; Soper, J. D. *J. Am. Chem. Soc.* **2010**, *132*, 14358. (f) Tondreau, A. M.; Atienza, C. C. H.; Weller, K. J.; Nye, S. a; Lewis, K. M.; Delis, J. G. P.; Chirik, P. J. *Science,* **2012**, *335*, 567.

(12) (a) Schulz, C. E.; Devaney, P. W.; Winkler, H.; Debrunner, P. G.; Doan, N.; Chiang, R.; Rutter, R.; Hager, L. P. *FEBS Lett.* **1979**, *103*, 102. (b) Groves, J. T.; Haushalter, R. C.; Nakamura, M.; Nemo, T. E.; Evans, B. J. *J. Am. Chem. Soc.* **1981**, *103*, 2884. (c) Penner-Hahn, J. E.; Smith Eble, K.; McMurry, T. J.; Renner, M.; Balch, A. L.; Groves, J. T.; Dawson, J. H.; Hodgson, K. O. *J. Am. Chem. Soc.* **1986**, *108*, 7819.

oxidizes iron from the +2 to the +3 oxidation state. Upon O−O bond scission, two oxidizing equivalents are transferred: one oxidizes iron to the +4 state, and the other is delocalized about the porpyhrin ligand and the proximal cysteine thiolate (Scheme 4.1c).[14] This type of ligand and transition metal distributed redox reactivity is expressed most simply as *molecular* redox states, wherein the location of oxidation state changes are not assigned. Other coordination complexes that display significant ligand-metal redox interplay include complexes utilizing porphyrinogens,[15] diiminopyridines,[16] and catechol species.[17]

D. *Disparate metal- and ligand-localized redox (Class IV, Scheme 4.1d):* An additional coordination complex classification is possible wherein both ligand and transition metal redox reservoirs are present but are accessible via different redox mechanisms. This type of redox separation demands energetic matching of the frontier metal- and ligand-based orbitals—which minimizes the thermodynamic driving force for outer-sphere electron transfer between metal and ligand[18]—without an orbital pathway through which the two redox reservoirs can communicate via inner-sphere electron transfer. Despite the prevalence of class II and class III examples, well-defined examples of class IV which feature ligand and metal as separate but equally accessible redox entities have not been reported to

(13) Watanabe, Y. In *The Porphyrin Handbook*; Kadish, K. M., Smith, K. M., Guilard, R., Eds.; Academic Press: NewYork, 2000; Vol. 4, pp 97-118.
(14) Rittle, J.; Green, M. T. *Science*, **2010**, *330*, 933.
(15) (a) Floriani, C.; Floriani-Moro, R. In *The Porphyrin Handbook*; Academic Press: San Diego, CA, 2003; Vol. 3, pp 405-420. (b) Jubb, J.; Floriani, C.; Chiesi-Villa, A.; Rizzoli, C. *J. Am. Chem. Soc.* **1992**, *114*, 6571. (c) Piarulli, U.; Solari, E.; Floriani, C.; Chiesi-Villa, A.; Rizzoli, C. *J. Am. Chem. Soc.* **1996**, *118*, 3634. (d) Crescenzi, R.; Solari, E.; Floriani, C.; Chiesi-Villa, A.; Rizzoli, C. *J. Am. Chem. Soc.* **1999**, *121*, 1695. (e) Bachmann, J.; Nocera, D. G. *J. Am. Chem. Soc.* **2004**, *126*, 2829. (f) Bachmann, J.; Nocera, D. G. *J. Am. Chem. Soc.* **2005**, *127*, 4730.
(16) De Bruin, B.; Bill, E.; Bothe, E.; Weyhermüller, T.; Wieghardt, K. *Inorg. Chem.* **2000**, *39*, 2936.
(17) Kaim, W.; Schwederski, B. *Pure App. Chem.* **2004**, *76*, 351.
(18) Marcus, R. A. *Angew. Chem. Int. Ed.* **1993**, *32*, 1111 and references therein.

the best of our knowledge. The results presented herein describe how coordination complexes featuring the trianionic tris(pyrrolyl)ethane ligand display class IV type behavior as outer-sphere electron transfer is solely ligand-centered, whereas inner-sphere redox reactions are mediated by the transition metal bound (Scheme 4.1d).

Scheme 4.1. Classification of redox behavior by redox localization.

(a) Class I: Metal-centered redox

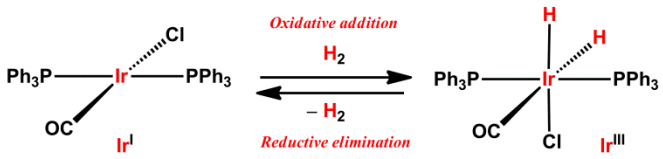

(b) Class II: Ligand-centered redox

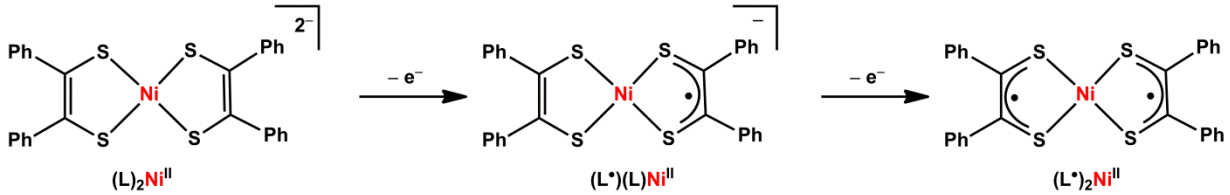

(c) Class III: Metal & Ligand delocalized redox

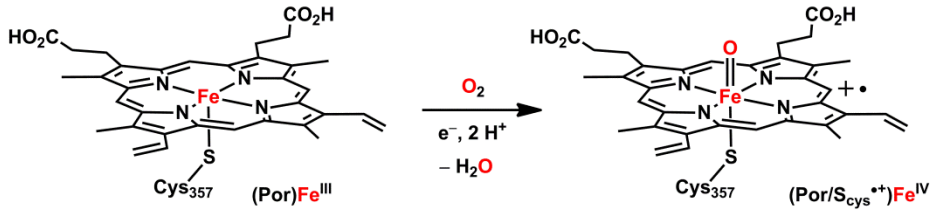

(d) Class IV: Disparate metal- or ligand-centered redox

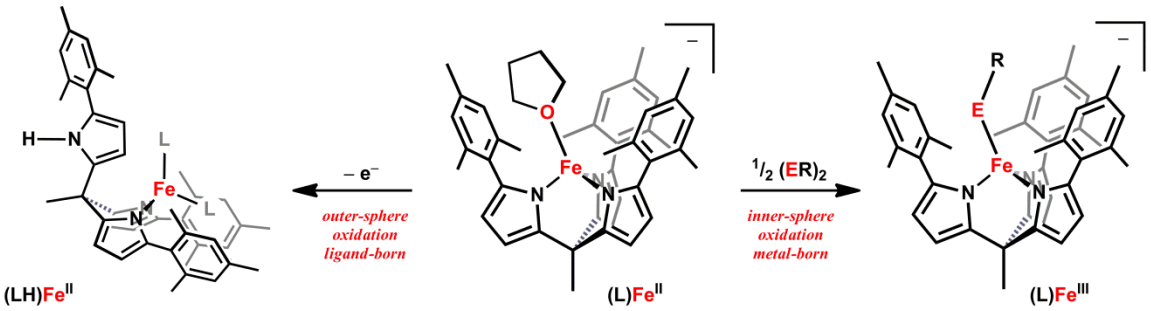

We previously reported the outer sphere oxidation of a series of $[(tpe)M^{2+}(py)]^{-}$ complexes (M = Mn, Fe, Co, Ni, Zn) via electrochemical or chemical methods (tpe = tris(2-mesitylpyrrolyl)ethane).[19] Examination of the electrochemical behavior of this series of complexes showed a common irreversible oxidative process (−655 mV vs. $[Cp_2Fe]^{+/0}$) that we proposed is ligand-based and unaffected by the identity of the bound transition metal. We attributed the observed oxidation process to removal of an electron from a tpe-derived

(19) Sazama, G. T.; Betley, T. A. *Inorg. Chem.* **2010**, *49*, 2512.

pyrrolide π orbital. The ligand pyrrollic π-electrons were shown to be highest in energy for the coordination complexes by DFT analysis akin to their dipyrromethane analogues.[20] Further inspection of the DFT and electrochemical results reveals a seemingly non-Aufbau arrangement of electrons, resulting in population of fully filled, delocalized ligand π-orbitals higher in energy than partially-filled metal 3d orbitals. This can be attributed to a combination of larger electron-pairing energy costs for the electrons in the metal-ion 3d orbitals and a lack of orbital overlap between the highest energy pyrrolide-based orbitals and metal orbitals of the appropriate symmetry. As a result of this orbital isolation between transition metal ion and tpe ligand, oxidation is localized on the more energetically accessible pyrrolide units of the tpe ligand. Chemical oxidation of the Zn- and Fe-bound species provided evidence for ligand oxidation, wherein a pyrrolide radical is formed leading to pyrrole dissociation and H-atom abstraction to result in a [(κ2-tpeH)Fe(py)2] product. Furthermore, attempts to metallate the tpe ligand with FeIII starting materials (i.e., FeCl3 and base, FeIII(N(SiMe3)2)3) resulted in outer-sphere electron transfer to the Fe moiety to produce only [(κ2-tpeH)Fe(py)2]. In light of this observed oxidative instability, we wanted to investigate if the tpe construct was incompatible with higher-valent states of the bound transition metal.

We present here our findings that while outer-sphere oxidation is ligand-borne, inner-sphere electron transfer reactions of the $[(tpe)Fe(THF)]^-$ anion result in metal-centered oxidation. The reaction of one- and two-electron oxidants with $[(tpe)Fe(THF)]^-$ form stable complexes which are spectroscopically revealed to contain a singly oxidized iron for both one- and two-electron oxidants. The reversible, one-electron reduction of a diazoalkane

(20) King, E. R.; Betley, T. A. *J. Am. Chem. Soc.* **2009**, *131*, 14374.

ligand by [(tpe)Fe(THF)]$^{-}$ is also observed to give a product containing a high-spin Fe^{3+} center antiferromagnetically coupled to a diazoalkane-borne radical. Each reaction demonstrates the viability of metal-centered redox activity on a ligand platform known to be redox unstable, qualifying the [(tpe)Fe]$^{-}$ construct as a unique example of a coordination complex of class IV.

4-2. Experimental

All manipulations were carried out in the absence of water and dioxygen using standard Schlenk techniques, or in an MBraun inert atmosphere drybox under a dinitrogen atmosphere. All glassware was oven dried for a minimum of 1 h and cooled in an evacuated antechamber prior to use in the drybox. Benzene, diethyl ether, *n*-hexane, tetrahydrofuran and toluene were dried and deoxygenated on a Glass Contour System (SG Water USA, Nashua, NH) and stored over 4 Å molecular sieves (Strem) prior to use. Benzene-d_6 (Cambridge Isotope Labs), *m*-xylene and bis(trimethyl)silyl ether (Sigma-Aldrich) were degassed and stored over 4 Å molecular sieves prior to use. Di-*tert*-butyl peroxide, dicumyl peroxide and dibenzyl disulfide were purchased from Aldrich and used as received. Anhydrous iron(II) chloride was purchased from Strem and used as received. Diphenyldiazomethane,[21] mesityl azide (2,4,6-$Me_3C_6H_2N_3$),[22] 4-^{t}Bu$C_6H_4N_3$,[23] and **1**[30] were synthesized according to published procedures. Celite® 545 (J. T. Baker) and 4 Å molecular sieves were dried in either a Schlenk flask or a vacuum oven for 24 h under dynamic vacuum while heating to at least 150 °C.

Characterization and Physical Measurements. ^{1}H and ^{13}C NMR spectra were recorded on Varian Mercury 400 MHz or Varian Unity/Inova 500 MHz spectrometers. 1H chemical shifts are reported relative to residual solvent peaks as reference. Elemental Analyses were carried out at Complete Analysis Labs, Inc. (Parsippany, NJ).

^{57}Fe Mössbauer spectra were measured with a constant acceleration spectrometer (SEE Co, Minneapolis, MN). Isomer shifts are quoted relative to Fe foil at room temperature.

(21) Miller, J. B. *J. Org. Chem.* **1959**, *24*, 560–561.
(22) Murata, S.; Abe, S.; Tomioka, H. *J. Org. Chem.* **1997**, *62*, 3055.
(23) Smith, P. A. S.; Hall, J. H. *J. Am. Chem. Soc.* **1962**, *84*, 480.

Data was analyzed and simulated with Igor Pro 6 software (WaveMetrics, Portland, OR) using Lorentzian fitting functions.

EPR spectra were obtained on a Bruker EleXsys E-500 CW-EPR spectrometer. All EPR samples were crystalline samples, washed 3 times with ~5 mL hexanes, and dissolved in ~0.5 mL toluene, affording 0.02–0.05 M solutions. Spectra were measured as frozen toluene glasses at non-saturating microwave powers of 0.6325–2 mW. The signals from the desired material could be distinguished from contaminant radical species by acquiring variable-power spectra. The signal from impurities saturates at a much lower microwave power, allowing the two species to be distinguished.

SQUID magnetometry was carried out using a Quantum Design MPMS-5S SQUID magnetometer. Measurements were obtained using material that was recrystallized from diethyl ether by addition of trace amounts of THF and cooling to −35 °C. Under a dry nitrogen atmosphere, the microcrystalline materials obtained were finely ground and packed in a polycarbonate capsule. Warm liquid eicosane was added to suspend the material in solid wax after cooling. DC susceptibility measurements were collected in the temperature range of 5-300 K in 5 degree increments under a DC field of 5000 or 10000 Oe. DC magnetization measurements were obtained in the temperature range of 1.8-10 K, under DC fields or 10, 20, 30, 40, 50, 60, and 70 kOe. The data collected were corrected for any diamagnetic contributions by comparison to an eicosane/capsule blank, and by the application of Pascal's constants to account for any core diamagnetism.[24] The reduced magnetization data were fit using the ANISOFIT package,[25] using a range of possible spin

(24) Bain, G. A.; Berry, J. F. *J. Chem. Ed.* **2008**, *85*, 532.
(25) Shores, M. P.; Sokol, J. J.; Long, J. R. *J. Am. Chem. Soc.* **2002**, *124*, 2279.

states (S = 3/2, 2, 5/2, and 3). Reasonable fitting parameter values were only obtained for the cases in which the spin state was set as S = 2.

X-Ray Crystallography Crystal structures of **2-8** were collected at 100 K. Data was collected as a series of φ and/or ω scans. Data was integrated using SAINT (Bruker AXS) and scaled with a multi-scan absorption correction using SADABS (Bruker AXS).[26] The structures were solved by direct methods or Patterson maps using SHELXS-97[27] and refined against F^2 on all data by full matrix least squares with SHELXL-97. All non-hydrogen atoms were refined anisotropically. Hydrogen atoms were placed at idealized positions and refined using a riding model. The isotropic displacement parameters of all hydrogen atoms were fixed to 1.2 times the U value of the atoms they are linked to (1.5 times for methyl groups). Lithium countercations were bound by diethyl ether or THF molecules, and generally showed some amount of disorder, which was treated using a disordered model and restraints and constraints as necessary. Further details on several structures are noted in the compiled CIF files. **Notes on 5**: The structure of **5** contains six molecules of [(tpe)Fe(NHC_6H_4tBu)][$Li(THF)_4$] in the asymmetric unit. The model was refined by separating the atom list into four equal sized parts and employing the BLOC command. The anilido hydrogen atoms were located in the difference map for all 6 molecules of the compound, and were refined using a riding model thereafter. **Notes on 6:** The structure of 6 was determined from data collected using a microcrystal sample and employing synchrotron radiation at the Argonne National Laboratory Advance Photon

(26) "Apex II". Bruker AXS, 2009. Madison, WI.
(27) Sheldrick, G. M. *Acta Cryst. A.* **2008**, *64*, 112.

Source, ChemMatCARS.[28] The hydrogen atom residing on the anilido nitrogen was located as a Q peak in the difference map, and then refined using a riding model. **Notes on 7:** The structure of **7** contains two molecules of [(tpe)Fe(N_2CPh_2)][Li(L)$_4$] in the asymmetric unit. One of the molecules shows positional disorder of the tpe mesityl units, and thus was refined using a disordered model.

[(tpe)Fe(OtBu)][Li(THF)$_4$] (2): A yellow-brown benzene solution (2 mL) of **1** (42.6 mg, 0.043 mmol) was added to a stirring benzene solution (1 mL) of di-*tert*-butyl peroxide (12.5 mg, 0..85 mmol) at room temperature and stirred. After approximately 2.5 hours, the solution turned a deep red. ^{1}H NMR monitoring of the reaction reveals disappearance of the peaks attributable to starting material **1** with the production of an NMR silent product. After 16 h, the solution was frozen and lyophilized and the residue rinsed with cold hexanes to remove excess oxidant. The residue was extracted with diethyl ether. In order to assess yield accurately, the material can be precipitated from diethyl ether with added 12-crown-4 or diglyme at −35 °C, collected on a fritted glass funnel and washed with hexanes, affording 38.8 mg (86%) dark red powder. If X-ray diffraction quality crystals are desired, crystals can be grown from saturated hexane solutions by avoiding crown ether, and instead extracting the residue into hexane, and allowing the solution to stand at room temperature. However, these crystals are not of sufficient quality to obtain high-quality X-ray crystallographic data, and the data obtained are useful only for connectivity. Alternatively, analytically pure material can be obtained by cooling concentrated diethyl

(28) We thank Dr. Yu-Sheng Chen at ChemMatCARS, Advanced Photon Source, for his assistance with single-crystal data. ChemMatCARS Sector 15 is principally supported by the National Science Foundation/Department of Energy under grant number NSF/CHE-0822838. Use of the Advanced Photon Source was supported by the U. S. Department of Energy, Office of Science, Office of Basic Energy Sciences, under Contract No. DE-AC02-06CH11357.

ether solutions from room temperature to −35°C. Comb. Anal. for the species containing THF bound lithium, [$C_{61}H_{83}FeLiN_3O_5$]: Calc: C, 73.16; H, 8.36; N, 4.20; Found: C, 72.89; H, 8.08; N, 4.30.

[(tpe)Fe(OC(Ph)Me$_2$][Li(THF)$_4$] (3): A yellow-brown benzene solution (1.5 mL) of **1** (35.1 mg, 0.035 mmol) was added to a stirring benzene solution (1 mL) of dicumyl peroxide (5.7 mg, 0.021 mmol) at room temperature and stirred. After about 3 hours, the material began to color noticeably to a brown hue, and after about 6 hours the solution was a deep red brown. ^{1}H NMR monitoring of the reaction reveals disappearance of the peaks attributable to starting material **1** with the production of an NMR silent product. After 12 hours, the solution was frozen and lyophilized. To assess the reaction yield, the residue was extracted into diethyl ether, and [(tpe)Fe(OC(Ph)Me$_2$][Li(12-C-4)$_2$] was precipitated from diethyl ether at −35 °C by the addition of 12-crown-4. The resultant dark red powder was collected on a glass fritted funnel, washed with hexanes and dried to yield 37.9 mg product (90%). Crystals suitable for X-ray diffraction can be grown by extracting the reaction product (from lyophilization) into minimal diethyl ether and cooled from room temperature to −35°C, affording red-purple needles. Comb. Anal. for the species containing THF bound lithium cation, [$C_{66}H_{85}FeLiN_3O_5$]: Calc: C, 74.53; H, 8.06; N, 3.95; Found: C, 74.29; H, 7.95; N, 4.01.

[(tpe)Fe(SBn)][Li(THF)$_4$] (4): A yellow-brown benzene solution (2 mL) of **1** (35.4 mg, 0.0354 mmol) was added to a stirring benzene solution (1 mL) of dibenzyl disulfide (4.7 mg, 0.019 mmol) at room temperature and stirred for 92 hours, during which the solution turned a deep brown-purple. ^{1}H NMR monitoring of the reaction reveals disappearance of the peaks attributable to starting material **1** with the production of an NMR silent product.

The solution was frozen and lyophilized. The residue was triturated with bis-trimethylsilyl ether (2 mL) and hexane (2 mL), and recrystallized from diethyl ether at −35 °C, affording 23.3 mg (63%) purple needles. Crystals suitable for X-ray diffraction can be grown from concentrated diethyl ether solutions cooled from room temperature to −35°C. Comb. Anal. for [$C_{64}H_{81}FeLiN_3O_4S$]: Calc: C, 73.10; H, 7.77; N, 4.00; Found: C, 72.84; H, 7.51; N, 4.11.

[(tpe)Fe(NHC$_6$H$_4$-4-*t*Bu))][Li(THF)$_4$] (5): A yellow-brown benzene solution (2 mL) of **1** (36.0 mg, 0.0360 mmol) was added to a stirring benzene solution (2 mL) of 4-^{t}BuC$_6$H$_4$N$_3$ (7.1 mg, 0.041 mmol) at room temperature and stirred for 15 minutes, during which the solution turned vibrant dark purple. ^{1}H NMR monitoring of the reaction reveals disappearance of the peaks attributable to starting material **1** with the production of an NMR silent product. Volatiles were removed from an aliquant, which was submitted for IR analysis (KBr), revealing consumption of azide via disappearance of the azide stretch (υ_{N3}). Volatiles were removed in vacuo and the resultant residue was washed with hexane (3 x 2 mL), dissolved in diethyl ether and recrystallized by cooling the solution from room temperature to −35 °C. Crystals suitable for X-ray diffraction can be grown concentrated diethyl ether cooled from room temperature to −35°C. Comb. Anal. for species with THF bound Li^+, [$C_{67}H_{88}FeLiN_4O_4$]: Calc: C, 74.74; H, 8.25; N, 5.21; Found: C, 74.42; H, 8.09; N, 4.99.

[(tpe)Fe(NHMes)][Li(THF)$_4$] (6): A benzene solution (1 mL) of 2,4,6-trimethylphenyl azide (15.7 mg, 0.095 mmol) was added to a stirring, yellow-brown benzene solution (2 mL) of **1** (80.0 mg, 0.080 mmol) at room temperature and stirred for 15 minutes, during which the solution turned vibrant dark purple. ^{1}H NMR monitoring of the reaction reveals disappearance of the peaks attributable to starting material **1** with the production of an

NMR silent product. Volatiles were removed from an aliquant, which was submitted for IR analysis (KBr), revealing consumption of azide via disappearance of the azide stretch (υ_{N3}). Volatiles were removed in vacuo and the resultant residue was washed with hexane (3 x 2mL), dissolved in diethyl ether and recrystallized by cooling the solution from room temperature to −35 °C. Microcrystals suitable for X-ray diffraction with synchrotron radiation can be grown from concentrated diethyl ether solutions cooled from room temperature to −35°C. Comb. Anal. for $[Li(THF)_4]^+$ containing species, $[C_{67}H_{88}FeLiN_4O_4]$: Calc: C, 74.60; H, 8.16; N, 5.28; Found: C, 74.42; H, 8.09; N, 4.99.

[(tpe)Fe(N_2CPh_2)][Li(THF)$_4$] (7): A yellow-brown benzene solution (2 mL) of **1** (38.8 mg, 0.039 mmol) was added to a stirring benzene solution (1 mL) of diphenyldiazomethane (8.1 mg, 0.042 mmol) at room temperature and stirred for 2.5 hours, during which the solution turned a deep greenish brown. ^{1}H NMR monitoring of the reaction reveals disappearance of the peaks attributable to starting material **1** with the appearance of a new paramagnetically-shifted ^{1}H NMR spectrum. IR analysis revealed a disappearance of the diazoalkane ($\upsilon_{N=N}$) stretching frequency. The solution was frozen and lyophilized. The residue was extracted into diethyl ether and crystallized by addition of a drop of THF and cooling to −35 °C, affording green plates. Crystals suitable for X-ray diffraction can be grown by addition of two drops of THF to a solution of crystallized product in *m*-xylenes and cooling to −35°C. The product crystallizes with a large amount of solvent disorder about the lithium cations, ranging in formulation from $[Li(THF)(OEt_2)_2]^+$ to $[Li(THF)_3(OEt_2)]^+$. Analytically pure material containing the $[Li(THF)_4]^+$ cation can be obtained by precipitation of the material from a diethyl ether solution by addition of a drop of THF, cooling to −35 °C, isolation on a frit, washing with hexanes (2 mL) and drying by

passing dry nitrogen through the material on the frit. ^{1}H NMR (500 MHz, C_6D_6): δ/ppm: 98.23 (br s), 55.49 (br s), 48.24 (br s), 39.95 (s), 27.94 (s), 10.56 (br s), 7.70 (s), 7.35 (s), 7.02 (s), 3.82 (br s), 2.19 (m), 1.59 (br s), 0.82 (br s), -5.32 (br s), -90.2 (br s). Comb. Anal. for [$C_{70}H_{84}FeLiN_5O_4$]: Calc: C, 74.89; H, 7.55; N, 6.24; Found: C, 74.79; H, 7.36; N, 6.27.

[(tpe)Fe(PMe$_3$)][Li(THF)$_4$] (8): One drop of trimethylphosphine (PMe_3, excess) was added to a stirring, yellow-brown THF (2 mL) solution of **1** (52.3 mg, 0.052 mmol, assuming $[Li(THF)_4]^+$ as solvated cation) at room temperature and stirred for 10 minutes. Volatiles were removed in vacuo and the resultant residue was dissolved in diethyl ether. A yellow-brown solid was precipitated by the addition of two drops THF and cooling the solution to −35 °C. The precipitate was collected on a medium porosity frit, washed with 5 mL of pentane and 55.0 mg of a tan powder was collected (105%; yield is assumed to be quantitative, as the solvation of the lithium cation of **1** may change over time). Crystals suitable for X-ray diffraction were grown from diethyl ether solutions with added THF cooled from room temperature to −35 °C. ^{1}H NMR (500 MHz, C_6D_6): δ/ppm: 80.08 (br s), 67.17 (br s), 58.22 (br s), 37.42 (br s), 25.82 (br s), 22.71 (br s), 14.40 (br s), 10.41 (br s), 9.19 (br s), 3.90 (br s), 1.49 (br s), −1.35 (br s), −9.37 (br s).

4-3. Results

4.3.1 Synthesis

In order to assess whether metal-based redox activity is observable for (tpe)Fe complexes, we canvassed the reactivity of the anion $[(tpe)Fe(THF)]^-$ with a variety of one- and two-electron oxidants for which $[(tpe)Fe(THF)]^-$ is not competent reductant,

necessitating metal coordination for electron transfer to occur, if at all.[29] Reaction of brown-yellow [(tpe)Fe(THF)][Li(THF)$_4$] (**1**)[30] with 0.6 equivalents of the single-electron oxidants di-*tert*-butyl peroxide, dicumyl peroxide and dibenzyl disulfide in benzene over the course of 12-92 hours results in formation of the ^{1}H NMR silent complexes of the type [(tpe)FeX][Li(THF)$_4$] (Scheme 4.2, X = OtBu (**2**), OCMe$_2$Ph (**3**), and SBn (**4**), respectively). The slow reaction times prohibit quantitative reaction, as both starting material and products are thermally sensitive and decompose at room temperature under a nitrogen atmosphere on the timescale of the reaction. Given the variability of THF solvation to the lithium countercation, accurate yields were determined by precipitating the product from diethyl ether by the addition of excess 12-crown-4. Displacement of THF from Li^+ with 12-crown-4 renders the complex insoluble in all relevant organic solvents to afford products with reliable [(tpe)FeX][Li(12-crown-4)$_2$] formulations. Yields for the peroxide reactions were found to be 84% (**2**) and 80% (**3**) by this method. Due to the slower reaction rate and competing thermal decomposition, a lower yield of 63% was found for compound **4**, but precipitation with 12-crown-4 was not necessary to obtain pure material. Crystals suitable for single crystal x-ray diffraction can be grown from concentrated hexanes or diethyl ether solutions cooled to −35 °C.

(29) Antonello, S.; Musumeci, M.; Wayner, D. D. M.; Maran, F. *J. Am. Chem. Soc.* **1997**, *119*, 9541.
(30) Sazama, G. T.; Betley, T. A. *Organometallics* **2011**, *30*, 4315–4319.

Scheme 4.2. Chemical oxidations of compound **1**.

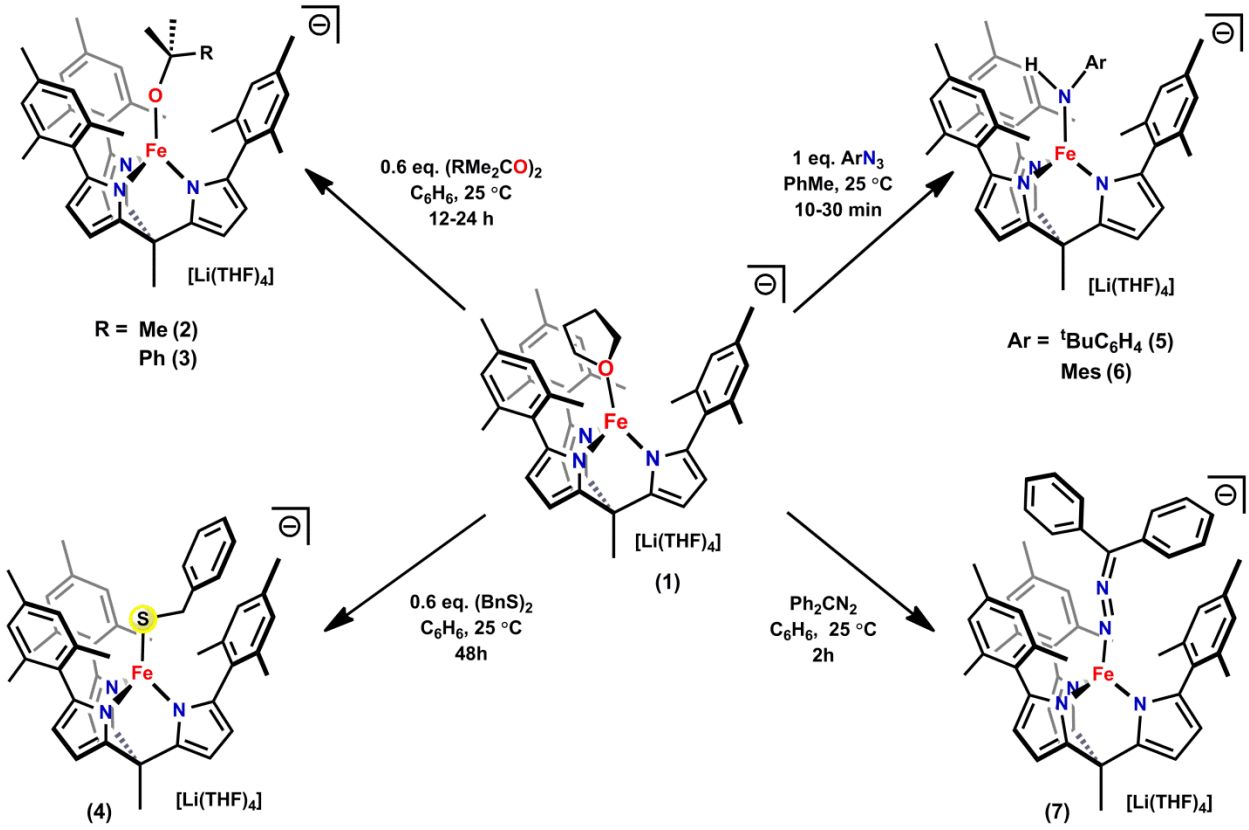

The addition of substituted aryl azides (4-^{t}BuC$_6$H$_4$N$_3$, MesN$_3$) to **1** in benzene at room temperature produces dark, inky purple solutions over the course of minutes. Consumption of the starting material (**1**) was ascertained by monitoring the disappearance of the ^{1}H NMR resonances for **1** to the resultant ^{1}H NMR silent products. Additionally, the frequencies corresponding to azide N−N stretching frequencies in the IR spectrum disappear following reaction with **1**. Crystals suitable for single crystal X-ray diffraction were grown from concentrated diethyl ether solutions with trace amounts of THF present at −35 °C. Solid-state structure determination via X-ray diffraction confirmed the identity of the products as the iron-anilido complexes [(tpe)Fe(NHAr)][Li(THF)$_4$] [Scheme 4.2, Ar = 4-^{t}BuC$_6$H$_4$ (**5**), Mes (**6**)].

The addition of diphenyldiazomethane to complex **1** in thawing benzene over the course of one hour results in a dark, inky green solution. Unlike the ^{1}H NMR silent species **2**-**6**, the reaction with diphenyldiazomethane exhibits a new paramagnetically shifted ^{1}H NMR spectrum distinct from **1** with 16 observable resonances. Furthermore, the resonant frequencies in the IR spectrum corresponding to the diazo stretching vibrations are no longer observable (free N_2CPh_2 $\upsilon_{N=N}$ = 2041 cm^{-1}).[21] Crystals suitable for single crystal X-ray diffraction were grown from a concentrated solution of the reaction product in *m*-xylene with trace amounts of THF, providing evidence for the formation of diazoalkane adduct $[(tpe)Fe(N_2CPh_2)][Li(L)_4]$ (**7**, L = THF, Et_2O, Scheme 4.3).

4.3.2 Identification of Oxidation Products via Structural Elucidation

Given the paucity of spectroscopic data for the reaction products **2**-**7**, reaction product identification was entirely dependent on molecular structure determination via X-ray diffraction analysis. The products of the above reactions, **2**-**7**, (Figure 4.1-Figure **4.3**) all maintain iron coordinated to the trianionic tpe ligand in a $\kappa^1,\kappa^1,\kappa^1$-fashion, with a fourth apical ligand completing the coordination sphere. The apical ligand is unequivocally anionic for products **2**-**6**: alkoxides (**2** and **3**), benzylsulfide (**4**), or monoanionic anilido (**5** and **6**) suggesting in each oxidation reaction examined the oxidant has been chemically altered concomitant with oxidation of the iron center. Despite the oxidation, each complex remains anionic with a lithium countercation present and solvated by THF or diethyl ether as identified in each of the solid state molecular structures.

The positional disorder present in the structure of **2** does not permit rigorous determination of the bond metrics within the anion. The data acquired, however, was

satisfactory to confirm the overall connectivity and identity of the anion. The crystal structures of **3** and **4** do not exhibit the same position disorder for the tpe ligand, aided by the asymmetric binding of alkoxide and thiolate ligands in the product which prevent positional variation in the tpe mesityl flanking units, permitting full refinement of the molecular structures. The solid state molecular structures of **3** and **4** are presented in Figure 4.1. The structures of the alkoxide products **2** and **3** confirm cleavage of the dialkyl peroxide O−O bond and formation of a new Fe−O bond in both cases, while the structure of benzyl sulfido **4** shows the analogous S−S bond breakage and Fe−S bond formation. The average Fe-N_{tpe} bond lengths are 1.975(5) Å for **3** and 1.969(5) Å for **4**, a shortening of ~0.05 Å compared to the bond lengths of the starting material, **1** (average *d*(Fe−N_{tpe}): 2.022(5)).[30] In addition, the oxygen atom of the cumyl alkoxide ligand in **3** is 0.245 Å closer to the iron (*d*(Fe−O): 1.778(3) Å) than the ethereal oxygen in the THF-adduct starting material, **1** (*d*(Fe−O): 2.023(3) Å), signifying increased π-donation between the alkoxide ligand and iron. The structural perturbations are summarized in Table 1.

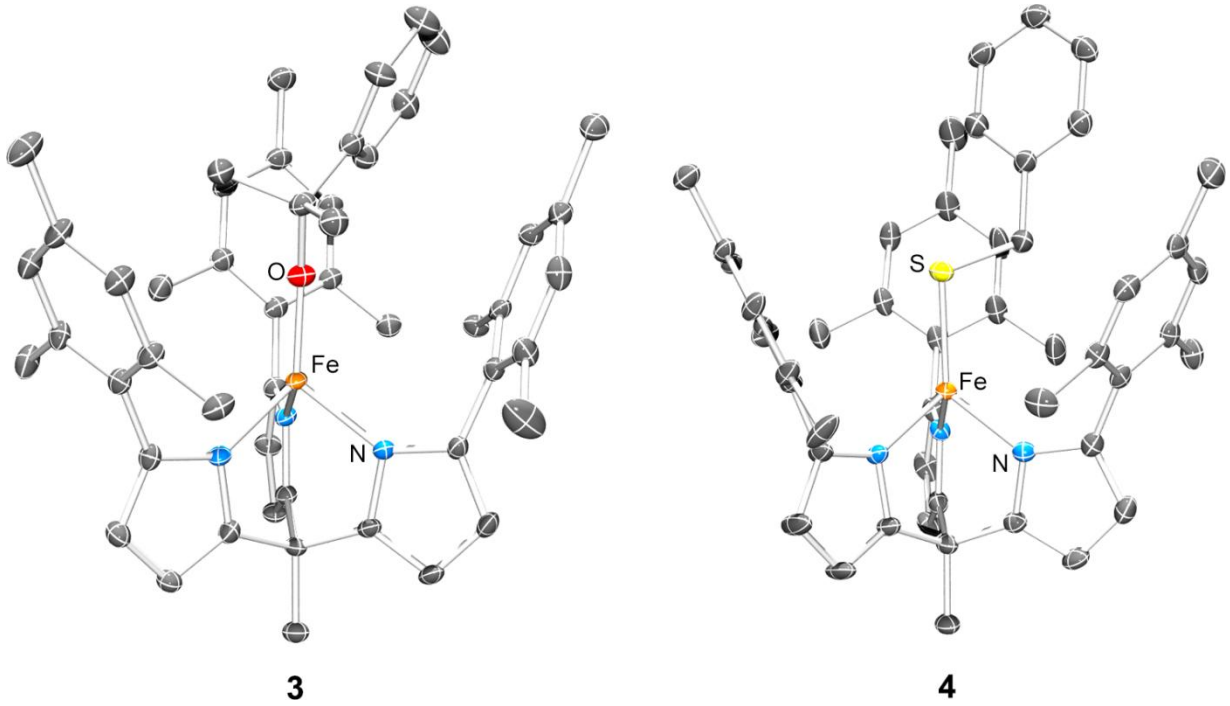

3 4

Figure 4.1. Solid state molecular structures of the anions in **3** and **4**. Thermal ellipsoids are shown at 30% probability, and hydrogen atoms and solvated lithium countercations are omitted for clarity. Relevant bond distances (Å) and angles (°) follow. For **3**, Fe–O: 1.778(3); Avg. Fe–N: 1.975(5); Fe–O–C_{cumyl}: 153.9(3). For **4**, Fe–S: 2.2381(11); Avg. Fe–N: 1.969(5); Fe–S–C_{benzyl}: 102.80(13).

Table 4.1. Important bond metrics for compounds **1**, and **3-7**. Compounds assigned as Fe^{2+} are listed first, for comparison to those assigned as Fe^{3+}. Structural details can be found in the text.

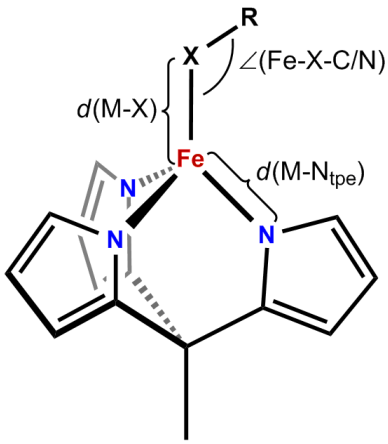

Compound		Avg. d(Fe–N_{tpe}) (Å)	Δd(Fe–N) from **1** (Å)	d(M–X) (Å)	∠(Fe–X–C/N) (°)
$[(tpe)Fe(THF)]^-$	(**1**)	2.022(5)	---	2.023(3)	---
$[(tpe)Fe(OCPhMe_2)]^-$	(**3**)	1.975(5)	−0.047	1.778(3)	153.9(3)
$[(tpe)Fe(SBn)]^-$	(**4**)	1.969(5)	−0.053	2.2381(11)	102.80(13)
$[(tpe)Fe(NHPhtBu)]^-$	(**5**)	1.9701(12)	−0.052	1.8836(7)	135.06(2)
$[(tpe)Fe(NHMes)]^-$	(**6**)	1.985(8)	−0.037	1.890(5)	141.9(4)
$[(tpe)Fe(N_2CPh_2)]^-$	(**7**)	1.955(29)	−0.067	1.781(9)	160.3(8)
$[(tpe)Fe(PMe_3)]^-$	(**8**)	1.9986(3)	−0.023	2.3796(4)	---
$[(tpe)Fe(py)]^{-}$[a]		2.014(3)	−0.008	2.068(2)	---

[a] From reference 19.

The solid state molecular structures of the reaction products **5** and **6** resulting from azide oxidation are provided in Figure 4.2. In both structures, the organic azide oxidant has been converted into an anilido ligand, confirmed by location of the anilido hydrogen atom in the difference map during both crystal structure refinements. Following the structural determination of these reaction products, direct evidence of H-atom abstraction by reaction of **1** with organic azides was obtained using ^{1}H NMR spectroscopy. Using 1,3,5-

trimethoxybenzene as an internal standard and 1,4-cyclohexadiene (CHD) as an H atom donor (73 kcal/mol),[31] the disappearance of the ^{1}H resonances corresponding to a stoichiometric amount of CHD was observed for reaction of **1** with both mesityl- and 4-^{t}BuC$_6$H$_4$-azide. This result suggests that in the absence of a weaker H-atom donor, THF or solvent is activated by a reaction intermediate (*vide infra*) to form products **5** and **6**.

The Fe-N$_{tpe}$ distances average 1.970(1) Å in **5**, and 1.985(8) Å in **6**, and are ca. 0.05 Å shorter than the 2.022(5) Å average Fe–N$_{tpe}$ distances of compound **1**, mirroring the change observed for the one electron oxidations observed in the structures for **3** and **4**. The Fe–N$_{anilido}$ bond lengths of 1.884(7) Å (**5**) and 1.890(5) Å (**6**) are shorter than the Fe–N$_{pyridine}$ distance of 2.068(2) Å found in the [(tpe)Fe(py)]$^-$ anion,[19] and are most similar to known Fe^{3+} amido species.[32] The average Fe-N-C$_{Ar}$ bond angle found for **5** is 135.06(2)° and the Fe-N-Ar bond angle for **6** is 141.9(4)°, values which are consistent with an anilido ligand featuring an sp^2 hybridized N bound to Fe.

(31) McMillen, D. F.; Golden, D. M. *Ann. Rev. Phys. Chem.* **1982**, *33*, 493.
(32) Eckert, N. A; Smith, J. M.; Lachicotte, R. J.; Holland, P. L. *Inorg. Chem.* **2004**, *43*, 3306.

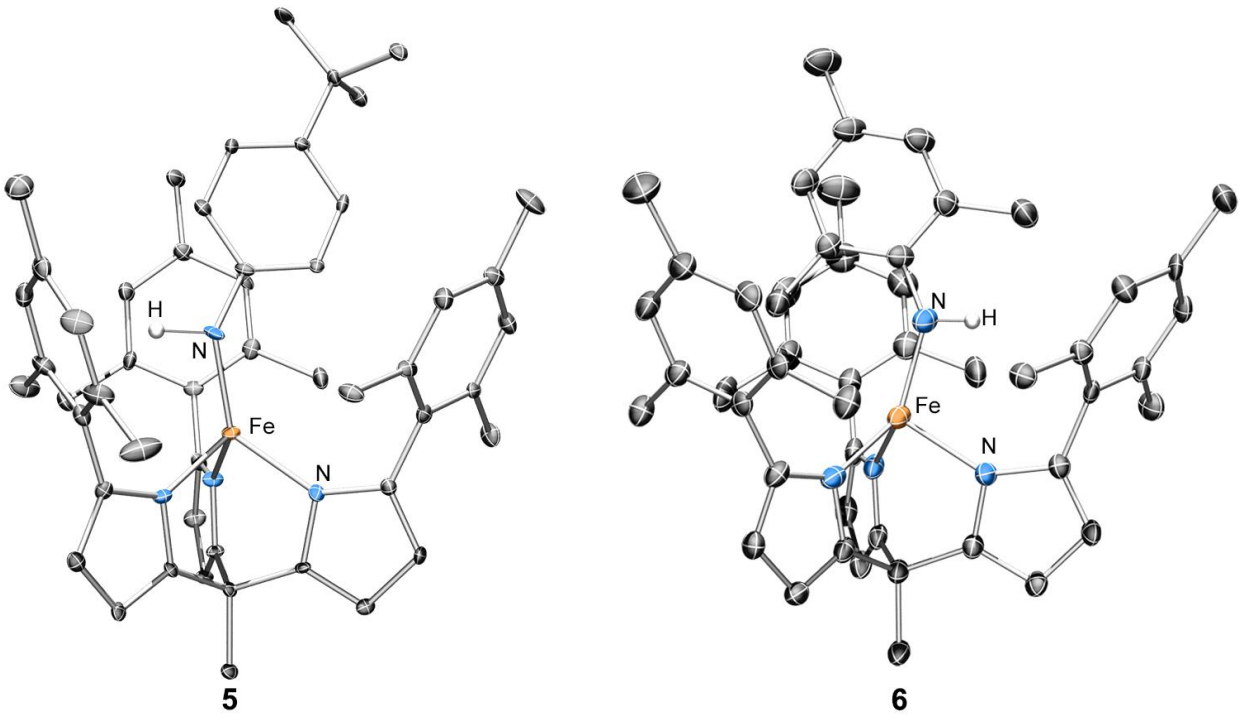

Figure 4.2. Solid state molecular structures of the anions in **5** and **6**. Thermal ellipsoids are shown at 30% probability, and hydrogen atoms and solvated lithium counterions are omitted for clarity. Amido hydrogen atoms are included. Relevant bond distances (Å) and angles (°) follow. For **5**, Fe−N_{amido}: 1.8836(7); Avg. Fe−N_{tpe}: 1.9701(12); Fe−N−C_{aryl}: 135.06(2). For **6**, Fe−N_{amido}:1.890(5); Avg. Fe−N_{tpe}: 1.985(8); Fe−N−C_{aryl}: 141.9(4).

Unlike the reactions of **1** with dialkyl peroxides, dialkyl disulfide, or aryl azides, the reaction of **1** with diphenyldiazoalkane results in the binding of the diazoalkane moiety without substantial chemical modification of the diazoalkane. The solid state molecular structure of the anion for **7** (Figure 4.3) features tpe-bound iron, with the diazoalkane ligand bound end-on completing the coordination sphere. While the diazoalkane moiety is bound intact, the Fe−N_{tpe} bond lengths average 1.95(3) Å across the three structures found in the asymmetric unit, comparable to the average Fe-N_{tpe} found for compounds **2-6**, suggesting a redox transfer event has indeed taken place. The Fe−$N_{diazoalkane}$ distances

average 1.781(9) Å, which is significantly shorter than known four-coordinate Fe–N_{amide} distances,[32,33] including those found for anilido complexes **5** and **6**.

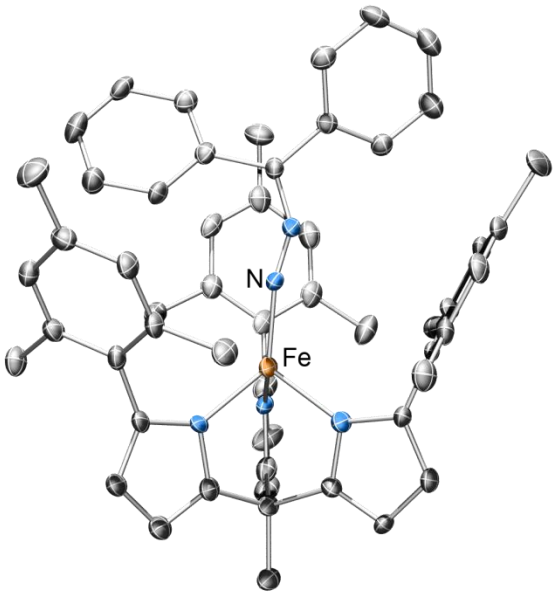

Figure 4.3. Solid state molecular structure of the anion in **7**. Thermal ellipsoids are shown at 30% probability, and hydrogen atoms and solvated lithium counterions are omitted from the crystal structure for clarity. Relevant bond distances (Å) and angles (°) for **7**: Fe–$N_{diazo:}$ 1.781(9); Avg. Fe–N_{tpe}: 1.95(3); Fe–N–N_{diazo}: 160.3(8).

To account for the tpe N–Fe bond contractions which signify iron oxidation in **7**, the diazoalkane moiety must be concomitantly reduced by one electron. Chemical transformation of the diazoalkane (i.e. H-atom abstraction to the N_2CPh_2 unit) was ruled out by examining the ability of **7** to undergo diazoalkane release. Treatment of complex **7** with excess PMe_3 in benzene resulted in an instantaneous change from dark, inky green to a pale brown-yellow color similar to the color of the THF adduct **1**. Tertiary phosphine ligand exchange is confirmed by ^{1}H NMR spectroscopy, as the paramagnetically shifted resonances of **7** disappear, giving way to a new paramagnetically shifted ^{1}H spectrum for the ferrous complex [(tpe)Fe(PMe_3)][Li(THF)$_4$] (**8**) (Scheme 4.3). An authentic sample of **8**

(33) Brown, S. D.; Peters, J. C. *J. Am. Chem. Soc.* **2004**, *126*, 4538.

can be obtained by simple addition of excess PMe_3 to starting material **1**, which features an identical ^1H NMR to the spectrum obtained from the diazoalkane displacement reaction above. If product **7** had undergone a chemical transformation following one-electron reduction (i.e. H-atom abstraction analogous to the azide oxidations), the diazoalkane ligand should not readily exchange with the neutral donor PMe_3.

Scheme 4.3. Reversible electron transfer activated by ligand exchange of [(tpe)Fe] complexes.

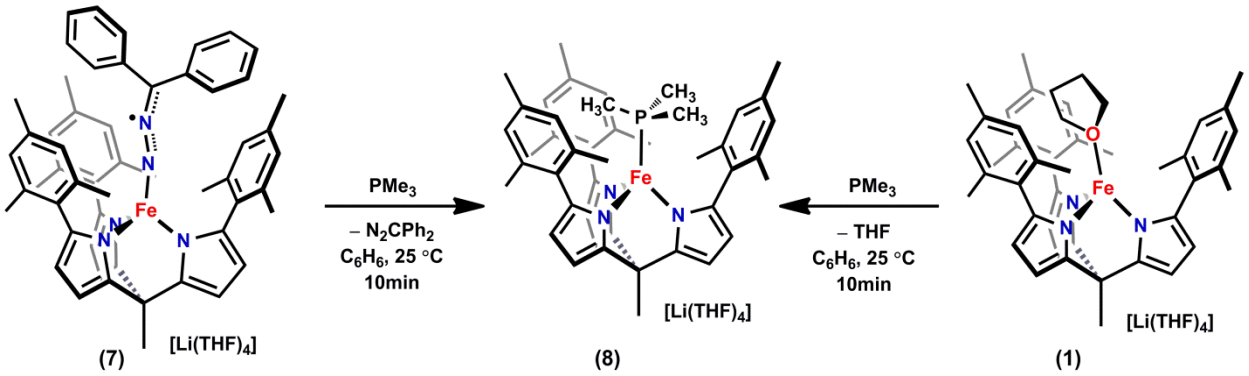

While the oxidation of the iron centers is demanded by charge balance in complexes **2**-**7** following the addition of the fourth anionic ligand to the iron coordination sphere, we sought to rigorously establish that the tpe ligand itself did not manifest changes signifying its participation in the observed redox event. If the pyrrolide subunits contribute to the observed redox event, we would anticipate substantial changes in the pyrrolic C–C and C–N bond distances. Similar bond length alterations in similar redox-active ligand platforms are hallmark redox signifiers.[3,6-9] Changes in pyrrole C–C and C–N distances after oxidation were all smaller than 3σ and thus considered insignificant. This observation supports that oxidation is primarily iron-centered and is not borne by the pyrrolides of the ligand. By way of comparison, the known redox-active ligand system α-iminopyridine exhibits successive C–C and C–N bond elongations of 0.06 Å per one-electron reduction of the

ligand.[11c] Aromatic C–C bond elongation of 0.027 Å is observed in the oxidation from phenylenediamine to the di(isobutyl)imino-semiquinone ligands.[34] All of these ligand alterations are readily observed and statistically significant.

4.3.3 Zero-field ^{57}Fe Mössbauer Spectroscopy

Complexes **2-4** exhibit single quadrupole doublets in the ^{57}Fe Mössbauer spectra at 90 K, with isomer shifts (δ) of 0.43, 0.38, and 0.36 mm/s, and quadrupole splittings ($|\Delta E_Q|$) of 0.88, 1.00 and 1.01 mm/s, respectively. Aryl anilide product **6** has an isomer shift of 0.26 mm/s and a quadrupole splitting of 1.83 mm/s. The isomer shift value is the lowest of the Fe^{3+} complexes we have isolated, but still well within the range of typical values for four-coordinate Fe^{3+} ions.[35] Finally, diphenyldiazomethane adduct **7** gives Mössbauer parameters remarkably similar to complexes **2-4**, with an isomer shift of δ = 0.37 mm/s and quadrupole splitting of $|\Delta E_Q|$ = 1.49 mm/s. Mössbauer data are summarized in Table 4.2.

(34) (a) Ketterer, N. A; Fan, H.; Blackmore, K. J.; Yang, X.; Ziller, J. W.; Baik, M.-H.; Heyduk, A. F. *J. Am. Chem. Soc.* **2008**, *130*, 4364. A. L. Balch and R. H. Holm, *J. Am. Chem. Soc.,* **1966**, *88*, 5201; (b) L. F. Warren, *Inorg. Chem.,* **1977**, *16*, 2814; (c) A. Anillo, M. R. Diaz, S. Garcia-Granda, R. Obeso-Rosete, A. Galindo, A. Ienco and C. Mealli, *Organometallics*, **2004**, *23*, 471; (d) E. Bill, E. Bothe, P. Chaudhuri, K. Chlopek, K. Herebian, S. Kokatam, K. Ray, T. Weyhermüller, F. Neese and K. Wieghardt, *Chem.–Eur. J.,* **2005**, *11*, 204; (e) K. Chlopek, E. Bill, T. Weyhermüller and K. Wieghardt, *Inorg. Chem*., **2005**, *44*, 7087.

(35) (a) H. Nasri, M. K. Ellison, C. Krebs, B. H. Huynh,W. R. Scheidt, *J. Am. Chem. Soc*. **2000**, *122*, 10795. (b) H. Nasri, M. K. Ellison, B. Shaevitz, G. P.Gupta, W. R. Scheidt, *Inorg. Chem*. **2006**, *45*, 5284.

Table 4.2. Measured spectroscopic parameters from low-temperature EPR (4.3-6.0 K) and zero-field ^{57}Fe Mössbauer spectroscopy (90K) for compounds **2-7**. Experimental details can be found in the text.

[(tpe)Fe(**X**)]$^-$		**Experimental (Calculated)**							
X		δ (mm/s)	$\|\Delta E_Q\|$ (mm/s)	g	D[a]	E[a]	E/D	ΔD[a]	ΔE[a]
THF	(**1**)	0.91	2.84						
O^{t}Bu	(**2**)	0.43 (0.42)	0.88 (–0.61)						
OCPhMe$_2$	(**3**)	0.38 (0.42)	1.00 (1.00)	1.99	0.380	0.063	0.17	0.06	0.013
SBn	(**4**)	0.36 (0.31)	1.01 (1.08)	1.99	0.747	0.123	0.16	.001	0.025
NHC$_6$H$_4$^{t}Bu	(**5**)			1.99	0.663	0.113	0.17	0.15	0
NHMes	(**6**)	0.26 (0.40)	1.83 (1.16)						
N$_2$CPh$_2$	(**7**)	0.37 (0.38)	1.49 (-1.57)	2.01[b]	-3.27[b]	0.041[b]	.01		
py		0.84	2.54						

[a] Reported in units of cm^{-1}. [b]Measured by SQUID magnetometry.

4.3.4 X-band EPR Spectroscopy

X-band EPR spectra at 3.1 K of complexes **3**, **4** and **5**, shown in Figure 4.4, exhibit features at g_{eff} = 8.72, 5.17, 3.41 and 2.31 (complex **3**); g_{eff} = 8.66, 5.27, 3.33 and 2.27 (complex **4**); and at g_{eff} = 8.69, 5.18, 3.41 and 2.30 (complex **5**). The spectra for alkoxide **3** and benzyl sulfido **4** can be simulated as S = 5/2 spin systems (Figure 4.4, Table 4.2) with isotropic g-values of 1.988 and 1.995, respectively. The complexes show appreciable zero-field splitting (ZFS), with axial ZFS (D) of 0.379 cm^{-1}and 0.748 cm^{-1}, respectively, and both show intermediate amounts of rhombicity, with values of E/D of 0.168 for **3** and 0.164 for **4**. The line-

breadth can be accounted for by including significant amounts of D- and E-strain (ΔD = 0.061 and 0.0012 cm^{-1}, ΔE = 0.013 and 0.025 cm^{-1}, respectively) in the simulations. The spectrum of aryl amide **5** bears a striking similarity to alkoxides **2** and **3** and alkylsulfide complex **4**, and can also be simulated as an S = 5/2 spin high spin Fe^{3+} system very similarly to complexes **3** and **4**. The simulation employs an isotropic g = 1.990 and an anisotropic zero-field splitting with D = 0.664 cm^{-1}, E = 0.115 cm^{-1}, resulting in an E/D of 0.173. In this case, only D-strain (ΔD = 0.154 cm^{-1}) is needed to simulate the line-broadening adequately. In all three cases, the features at roughly g_{eff} = 8.7 and 2.3 are transitions of components of the m_s = ±1/2 states, and the 5.2 and 3.4 g_{eff} features are m_s = ± 3/2 state transitions. It is likely the m_s = ±5/2 states are of high enough energy that they are unpopulated and unobserved.

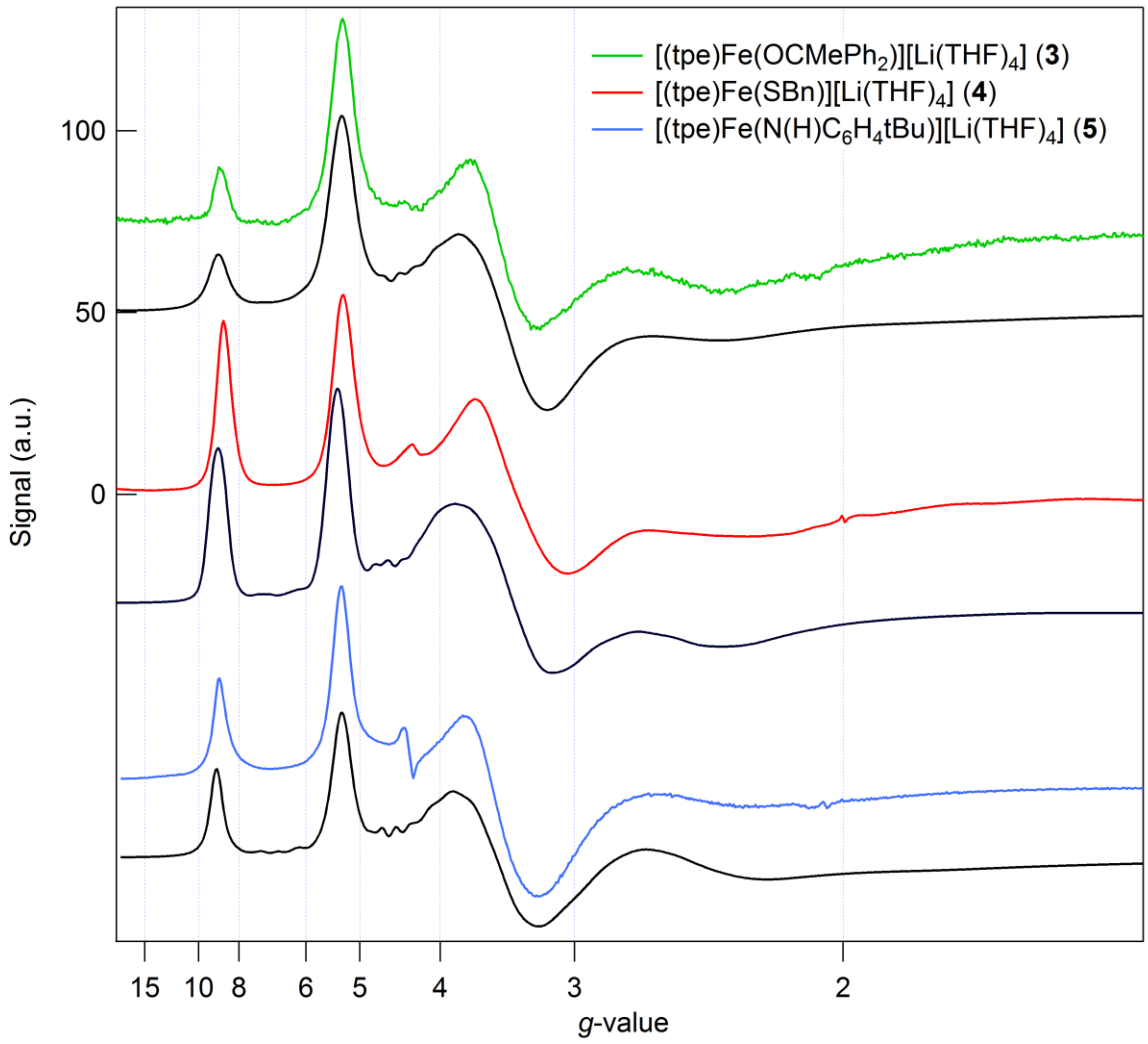

Figure 4.4. Normalized 3.1 K X-band EPR spectra of compounds **3** (green), **4** (red) and **5** (blue), with simulated spectra appearing below the experimental data as solid black lines. Experimental details: microwave power = 0.6325 to 2.0 mW; modulation amplitude = 10 G; approximately 5 mmol concentration as a toluene glass.

The X-band EPR spectrum of **7** at 4.3 K is shown in Figure 4.5, and does not resemble complexes **2-5**, instead displaying one major feature at g_{eff} = 8.34. This resembles S = 2 spin systems reported in the literature.[36] ^{1}H NMR spectroscopy corroborates this assignment, as a spectrum with distinct resonances is observed for complex **7**, whereas complexes **2-4**,

(36) Hendrich, M. P.; Gunderson, W.; Behan, R. K.; Green, M. T.; Mehn, M. P.; Betley, T. a; Lu, C. C.; Peters, J. C. *Proc. Nat. Acad. Sci.* **2006**, *103*, 17107.

simulated as $S = 5/2$ systems, are ^{1}H NMR silent. We hypothesized that the EPR spectrum observed for complex **7** represents an observable non-Kramers doublet of an integer spin system, and turned to magnetic measurements to interrogate this possibility.

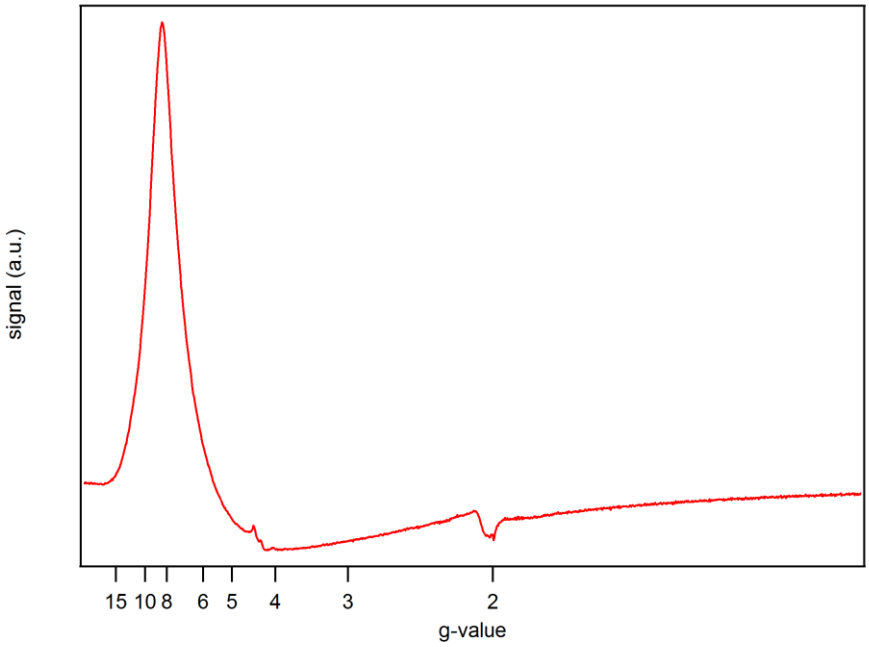

Figure 4.5. X-band EPR spectrum of **7** taken at 4.3K.

4.3.5 Magnetism

Variable temperature (VT) direct-current (DC) susceptibility data were collected from 5-300 K (Figure 4.6a). For complex **8** the average value of $\chi_M T$ in the temperature range of 50-300 K (the region for which we deem the Curie Law is applicable) was 3.43 cm^3 K/mol. The data for diphenyldiazomethane complex **7** do not differ greatly from the data for **8**, with an average $\chi_M T$ between 50 and 300 K of 3.44 cm^3 K/mol. The values obtained complex **8** are close to the value expected for a spin-only $S = 2$ system (3.00 cm^3 K/mol), as expected for a high-spin Fe^{2+} complex. Complex **7** exhibits strikingly similar values, suggesting that the overall spin ground state of **7** is $S = 2$.

A plot of reduced magnetization for **7** was obtained from VT data collected between 1.8-10 K at seven fields between 10-70 kOe (Figure 4.6b). The resulting plot shows non-superimposable isofield curves, indicative of zero-field splitting present in complex **7**. Using the Hamiltonian in equation 1, the reduced magnetization data was fit using the program ANISOFIT,[37] and reasonable values of g could only be obtained when fitting the system as an $S = 2$ ground state. The fitting parameters obtained are included in Table 4.2.

$$\widehat{H} = \mu_B g \boldsymbol{H} \cdot \widehat{\boldsymbol{S}} + D\hat{S}_z{}^2 + E(\hat{S}_x - \hat{S}_y)^2 \quad (1)$$

If the diazoalkane were to bind as a neutral donor ligand, an $S = 5/2$ ground state would be expected for the Fe^{3+} spin system, as determined by Mössbauer spectroscopy (*vide supra*). In order to satisfy the $S = 2$ ground state suggested by the magnetic data, we propose a system that features antiferromagnetic coupling of a diazoalkanyl radical ($S = 1/2$) to an $S = 5/2$ Fe^{3+}.

(37) Shores, M. P.; Sokol, J. J.; Long, J. R. *J. Am. Chem. Soc.* **2002**, *124*, 2279.

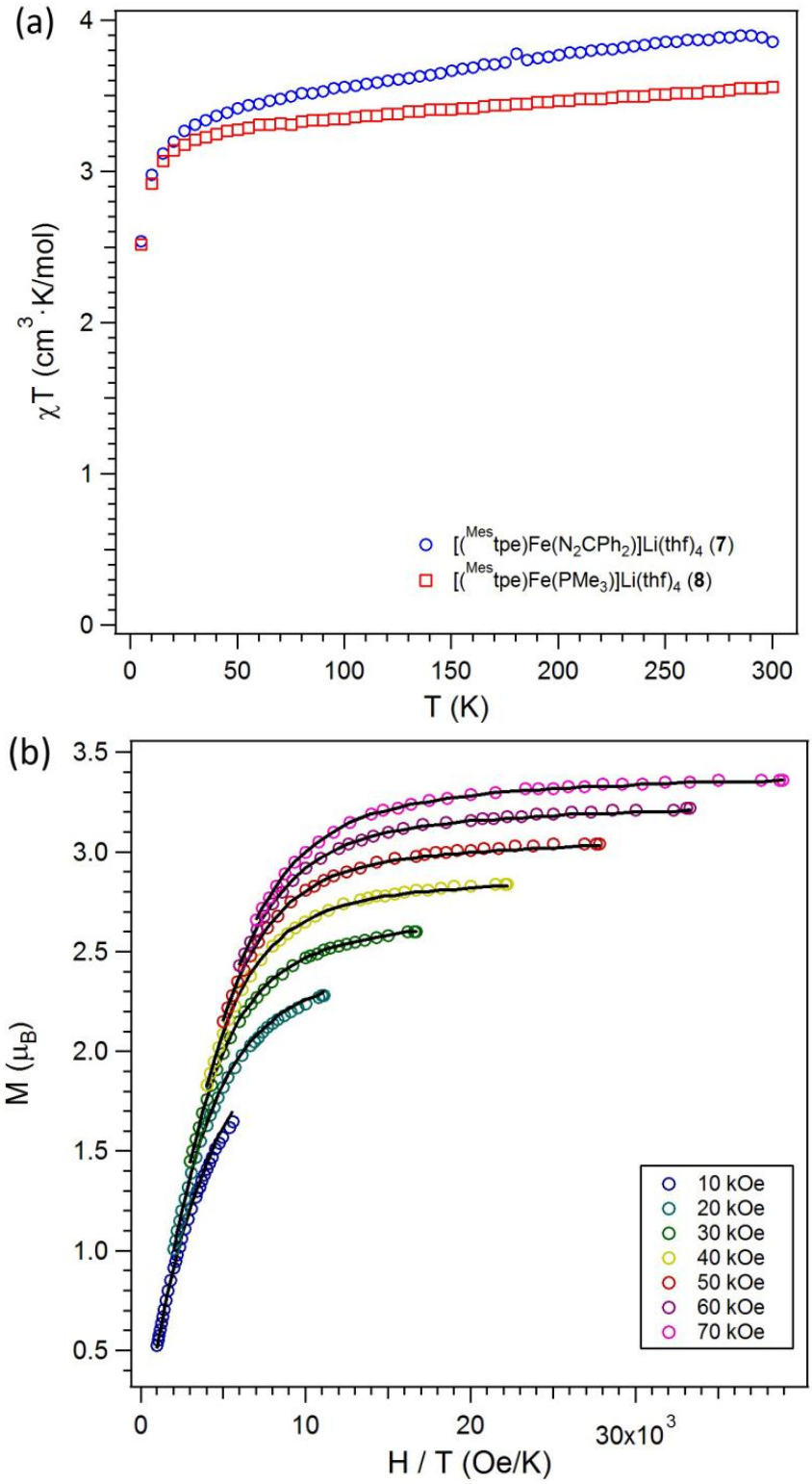

Figure 4.6. (a) Variable-temperature magnetic susceptibility data for **7** (blue circles) and **8** (red squares) collected in an applied dc field of 0.1 T. (b) Plot of reduced magnetization for **7** between 1.8 and 10 K at selected fields.

4.3.6 Density Functional Theory

DFT calculations were employed to establish the nature of the electronic spin ground states of complexes **2-7**. The crystal structure coordinates were optimized in a variety of spin-states, and the lowest energy spin state was confirmed to be $S = 5/2$ for **2*-6***, and $S = 2$ for **7*** (where ***** indicates the geometry optimized coordinates of the complex). The Mössbauer parameters of the lowest energy optimized structures were calculated in order to correlate the resultant optimized structures with experimental data, and matched remarkably well (Table 2).[38,39]

Broken symmetry calculations were employed to investigate the strength of the coupling between the iron center and the diazoalkanyl radical for structure **7***. The antiferromagnetic exchange coupling parameter (J) was calculated to be quite strong, with a value of -1508 cm^{-1}. A spin density plot of the optimized, quintet diazoalkane adduct clearly shows this antiferromagnetic coupling, as the net alpha spin is localized mainly on the iron atom and the net beta spin populates the π-bonding molecular orbital of the N−N fragment of the diazoalkane. This plot is presented alongside a spin density plot of the cumyl oxido structure for comparison in Figure 4. These DFT calculations also describe an overall $S = 2$ system featuring an $S = 5/2$ iron center antiferromagnetically coupled to an $S = 1/2$ ligand-based radical, as deduced from experimental data.

(38) King, E. R.; Hennessy, E. T.; Betley, T. A. *J. Am. Chem. Soc.* **2011**, *133*, 3336.
(39) (a) Neese, F. *Inorg. Chim. Acta* **2002**, *337*, 181. (b) Sinnecker, S.; Slep, L. D.; Bill, E.; Neese, F. *Inorg. Chem.* **2005**, *44*, 2245. (c) Römelt, M.; Ye, S.; Neese, F. *Inorg. Chem.* **2009**, *48*, 784.

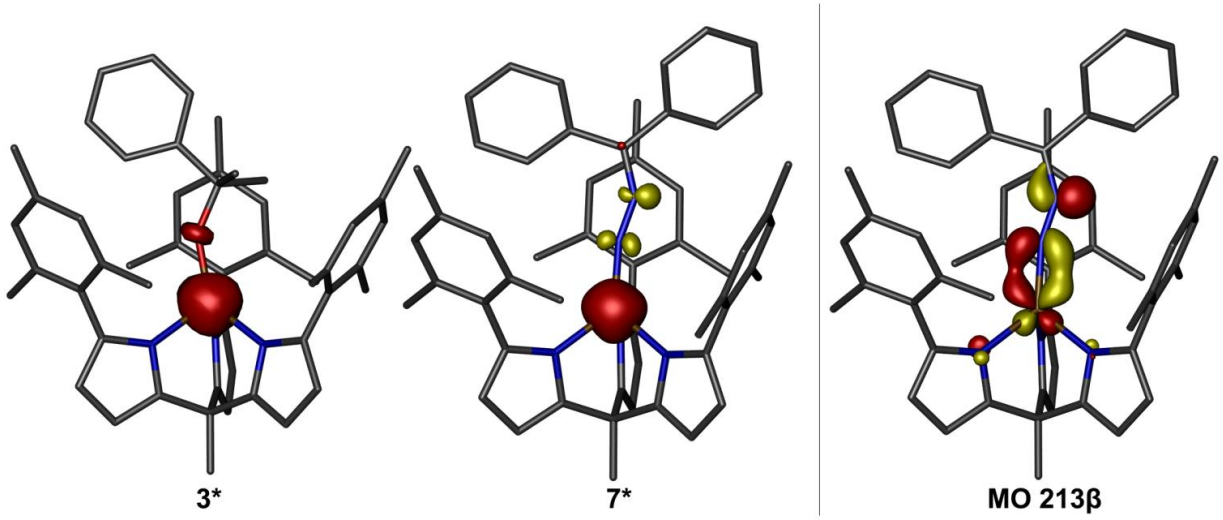

Figure 4.7. (Left) Spin polarization density plots (α – β) from single-point energy calculations of sextet **3*** and BS(5,1) **7*** calculated using the B3LYP functional shown at isovalue 0.01. Structures were optimized prior to single-point energy calculations using the BP86 functional. Bases are described in the experimental details. Net alpha spin density is shown in red, and net beta spin density in yellow. Atoms are labeled with their Mulliken spin population for iron and nitrogens possessing appreciable spin density**.** Hydrogen atoms are omitted for clarity. No localized net beta spin density is observed for the high-spin **3***, whereas significant spatial separation between net alpha and beta spins exists for structure **7***, leading to antiferromagnetic coupling between the Fe and ligand N atoms. (Right) occupied metal-L(π*) molecular orbital responsible for the beta spin polarization density observed (isovalue 0.08).

4-4. Discussion

The foregoing structural and spectroscopic analysis indicate the [(tpe)Fe(THF)]$^-$ synthon can undergo oxidation with concomitant reduction of dialkyl peroxide, dialkyl disulfide, aryl azides, and even diazoalkane substrates. As previously mentioned, the majority of the oxidation products, with the exception of **7**, are ^{1}H NMR silent and structural determination by X-ray crystallographic analysis provides a starting point to understand the reaction products. The charge balance incurred by the addition of alkoxide (**2**, **3**) and benzyl sulfido (**4**) ligands suggest products **2-4** feature a formally Fe^{3+} oxidation state following reaction. The redox potential of **1** is insufficient to reduce the dialkyl peroxides via an outer sphere mechanism,[29] suggesting the dialkyl peroxide, and by extension, dibenzyl disulfide reagents

must coordinate the metal center prior to electron transfer to induce O–O or S–S bond cleavage (Scheme 4.4). A similar reaction pathway has been invoked in the (nacnac)Cu mediated reduction of di-*tert*-butyl peroxide.[40]

Scheme 4.4. Proposed mechanism of inner-sphere oxidation of **1** by dialkyl peroxides and dialkyl disulfides.

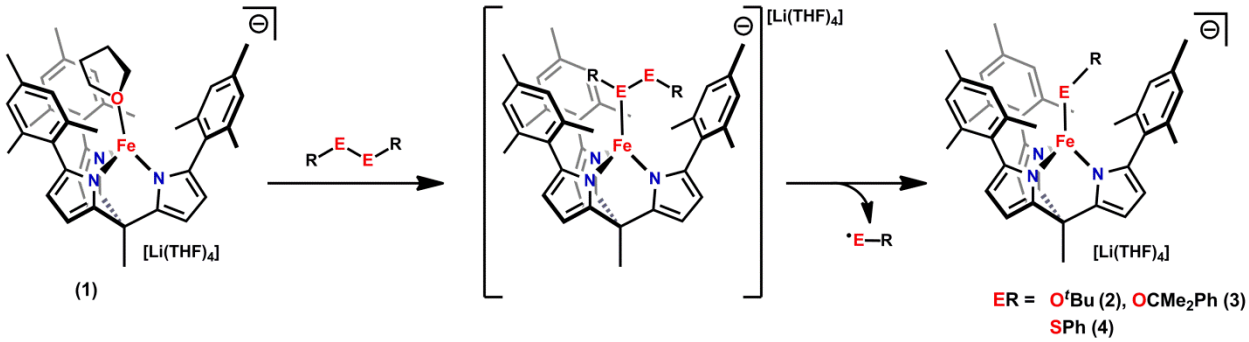

Reaction with organic azides results in complexes wherein, after the identification of the apical ligands in **5** and **6** as monoanionic anilido moieties, charge balance also suggests an Fe^{3+} formulation. Conversion of organic azides to amide ligands typically occurs via azide breakdown following coordination to the transition metal center to produce either imido radical[38] or closed-shell imido products.[41] The former results from single electron transfer to the azide, while the latter from full two-electron oxidation of the metal center. Both intermediates have been shown to be competent for H-atom abstraction reactions and are viable intermediates on the pathway of **1** to anilido products **5** and **6** (Scheme 4.5). Given the observed propensity of pyrrolide ligand-bound iron (II) complexes to undergo single

(40) (a) Kharasch, M. S.; Sosnovsky, G. *J. Am. Chem. Soc.* **1958**, *80*, 756. (b) Kharasch, M. S.; Sosnovsky, G.; Yang, N. C. *J. Am. Chem. Soc.* **1959**, *81*, 5819. (c) Rawlinson, D. J.; Sosnovsky, G. *Synthesis* **1972**, *1972*, 1. (d) Eames, J.; Watkinson, M. *Angew. Chem. Int. Ed.* **2001**, *40*, 3567. (e) Andrus, M. B.; Lashley, J. C. *Tetrahedron.* **2002**, *58*, 845. (f) Gephart, R. T.; McMullin, C. L.; Sapiezynski, N. G.; Jang, E. S.; Aguila, M. J. B.; Cundari, T. R.; Warren, T. H. *J. Am. Chem. Soc.* **2012**, *134*, 17350.

(41) (a) Jensen, M. P.; Mehn, M. P.; Que, L., Jr. *Angew. Chem., Int. Ed.* **2003**, *42*, 4457. (b) Lucas, R. L.; Powell, D. R.; Borovik, A. S. *J. Am. Chem. Soc.* **2005**, *127*, 11596. (c) Shay, D. T.; Yap, G. P. A.; Zakharov, L. N.; Rheingold, A. L.; Theopold, K. H. *Angew. Chem., Int. Ed.* **2005**, *44*, 1508. (d) King, E. R.; Betley, T. A. *Inorg. Chem.* **2009**, *48*, 2361. (e) King, E. R.; Sazama, G. T., Betley, T. A. *J. Am. Chem. Soc.* **2012**, *134*, 17858.

electron transfer events (*vide supra*),[38] we propose the imido radical intermediate might be operative in this example.

Scheme 4.5. Proposed mechanism of inner-sphere oxidation of **1** by organic azides.

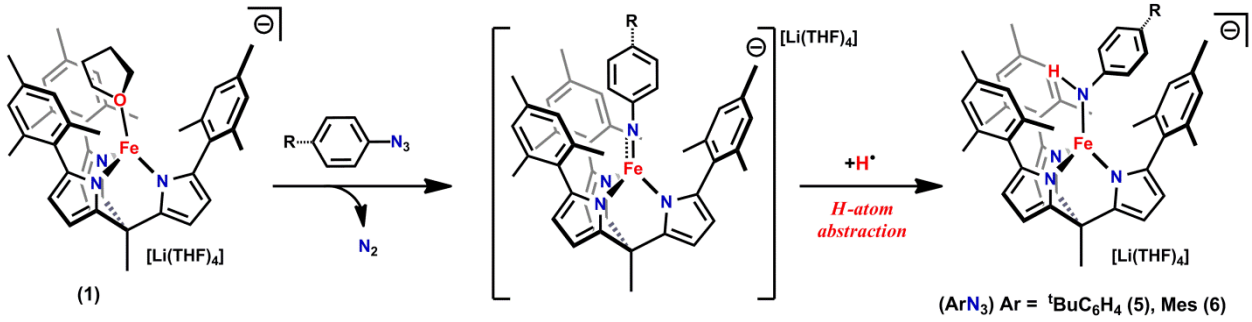

Charge balance is not reliable as an indicator of iron oxidation state for the structure obtained for product **7**, as the diazoalkane ligand could be bound as a neutral ligand or a doubly reduced ligand to adopt imido-like metal-ligand multiple bond.[42] The bond metrics obtained can, however, be compared to those of structures of **2-6**. Product **7** exhibits a shortening of the Fe−$N_{pyrrolide}$ distances similar in magnitude to that found for **2-6**. Additionally, the Fe−N_{diazo} bond distance is shorter than the Fe−$N_{anilido}$ bond length found for **5** and **6**, indicating a further interaction than would be expected between a neutral donor diazoalkane ligand and iron.[43] Further spectroscopic examination served to elucidate this interaction.

Zero-field, ^{57}Fe Mössbauer spectroscopy allows us to assess specifically the physical oxidation state at iron. The complexes remain four-coordinate following each reaction, thus the isomer shifts provide a straightforward indicator of iron oxidation state; the marked isomer shift decreases of 0.48 to 0.55 mm/s from the Fe^{2+} starting material, **1**, (δ = 0.91 mm/s) are strongly indicative of reduced electron density at the Fe atom, suggesting one-electron

(42) Jenkins, D. M.; Betley, T. a; Peters, J. C. *J. Am. Chem. Soc.* **2002**, *124*, 11238.
(43) Bart, S. C.; Bowman, A. C.; Lobkovsky, E.; Chirik, P. J. *J. Am. Chem. Soc.* **2007**, *129*, 7212.

oxidations have occurred. Comparison of the quadrupole splitting values of complexes **2-4** to the known Fe^{2+} species ($|\Delta E_Q|$ = 2.84) shows decreases ranging from 1.81 to 1.96 mm/s. In idealized C_{3v} symmetry, oxidation of a d^6 high-spin Fe^{2+} complex to a d^5 high-spin Fe^{3+} removes the single β electron responsible for the asymmetric population of the low-lying *e* $(x^2–y^2, xy)^3$ set, resulting in higher symmetry electron distribution at iron after oxidation, and thus a lower quadrupole splitting. The Fe^{3+} assignment is also affirmed by Mössbauer for a representative product of reaction of **1** with organic azide (**6**) as well. The EPR data collected corroborates these assignments, as EPR spectra of this shape have been observed previously for four-coordinate high spin Fe^{3+} complexes, including Fe^{III}-catecholate models of DOPA-containing mussel glue precursor proteins,[44] non-heme Fe^{III}-OOR superoxide reductase model complexes,[45] and synthetic Fe^{III} hydroxide complexes.[46] The magnitude of the zero-field splitting is also similar to these biological and synthetic high-spin Fe^{3+} systems reported in the literature.

The Mössbauer parameters acquired for **7**, along with the crystallographic data, allow us to unambiguously assign the oxidation state of iron in compound **7** as Fe^{3+}. Given the overall spin of S = 2 suggested by EPR and SQUID magnetometry together with the formulation of Fe^{3+}, we are also able to assign the oxidation state of the diazoalkane ligand. In order to achieve an overall spin of S = 2 the diazoalkane ligand must be a radical anion with S = 1/2, antiferromagnetically coupled to the S = 5/2 Fe^{3+}. This explanation also provides a rationale for the unusually short $Fe–N_{diazo}$ bond distance.

(44) Weisser, J. T.; Nilges, M. J.; Sever, M. J.; Wilker, J. J. *Inorg. Chem.* **2006**, *45*, 7736.
(45) Wallickt, E.; Cox, D. D.; Benkovic, S. J.; Bloom, L. M.; Bradley, F. C.; Nelson, M. J.; Que, L.; Wallick, D. E. *J. Am. Chem. Soc.* **1988**, *110*, 2026.
(46) MacBeth, C. E.; Gupta, R.; Mitchell-Koch, K. R.; Young, V. G.; Lushington, G. H.; Thompson, W. H.; Hendrich, M. P.; Borovik, A. S. *J. Am. Chem. Soc.* **2004**, *126*, 2556.

With the assignment of Fe^{3+} firmly established for complexes **2-7**, it is remarkable that no electron-transfer from the higher-energy tpe orbitals[19] to the oxidized iron is observed. Due to their weakly-donating nature[47] and poor π overlap with the metal orbitals, no inner-sphere electron transfer pathway between the pyrrolides and iron exists, and the thermodynamic driving force for electron transfer between the two moieties must be too low for an outer-sphere electron transfer to occur. Instead stable Fe^{3+} complexes are isolable with no ligand-to-metal redox communication evident. In other words, inner-sphere electron transfer is capable of accessing electrons in lower-energy, iron-based orbitals without perturbing higher-energy, tpe-based orbitals on the same energetic landscape.

By way of comparison to tpe iron complexes, previously reported examples of redox-active ligand systems feature metal and ligand molecular orbitals fully conjugated with one another and comprise a single molecular redox entity. This is typically observed for binding of the redox-active chelates onto the metal in a geometry that maximizes π-orbital overlap with the metal-based orbitals of appropriate symmetry, generating an orbital pathway that brings both redox reservoirs into conjugation.[3,5-11] In these literature examples, oxidations proceed from the highest to lowest energy molecular orbitals, regardless of oxidation mechanism, permitting the molecular entity to traverse several consecutive redox events. With the $[(tpe)M]^-$ species, the weakly σ-donating pyrrolides[47] enforce a tetrahedral-like geometry at the bound metal center. This geometric restriction, in concert with the weak-field ligand, conspires to engender open-shell configurations for the resulting coordination complexes, diminishing any π-orbital overlap between the pyrrolides and the metal center,

(47) DiFranco, S. A; Maciulis, N. A; Staples, R. J.; Batrice, R. J.; Odom, A. L. *Inorg. Chem.* **2012**, *51*, 1187.

thereby mitigating any available orbital overlap to connect the two redox reservoirs. As a result, the two disparate redox reservoirs are accessible by the different oxidation mechanisms.

The reversible electron-transfer to and from the diphenyldiazomethane provides further insight into the ligand-metal redox communication process. The diphenyldiazomethane ligand features a low lying π*-system with the proper orientation and energetic overlap to allow facile inner-sphere electron transfer from the Fe-based orbitals of π-symmetry. The resulting radical anion is delocalized within the diazoalkane N−N π-system, stabilized by steric protection provided by the (tpe) mesityl units and the CPh_2 terminus of the diazoalkane itself. In this case, the Fe−N bond is quite strong, being significantly shorter than the Fe−N bonds found in the anilido complexes **5** and **6** and even the putative imido radical observed on the related dipyrrin ligand platform.[38] Provided an orbital coupling pathway for electron transfer between metal and ligand, such as present in the diazoalkane adduct, redox communication becomes kinetically facile. In the absence of this orbital conjugation or a large enough thermodynamic driving force for outer-sphere transfer, coordination complexes of class IV are observed, featuring disparate redox reservoirs accessible by different oxidation mechanisms.

4-5. Conclusions

We have shown that tris(pyrrolide)ethane complexes of Fe^{2+} are stable to inner-sphere oxidation, whether one- or two-electron oxidants are employed. In the case of two-electron oxidation, the resultant two-electron oxidized species is unstable and undergoes an H-atom abstraction, resulting in a net single-electron oxidized product.

X-ray crystallography allows for direct comparison of the Fe^{2+} starting materials with the products reported, and suggests oxidation at iron upon reaction. An appreciable change in ^{57}Fe Mossbauer isomer shifts was observed for complexes **2**-**7**, which is a particularly good indicator of iron-specific oxidation. Low-temperature X-band EPR spectroscopy confirms the oxidation states suggested by the Mössbauer data and solidifies the $S = 5/2$ spin state of complexes **2-6** and reveals an $S = 2$ spin state of diazoalkane complex **7**. Taken together, these data unambiguously establish the oxidation state of iron to be 3+, in spite of the known redox liability of the tpe ligand. Removal of the diazoalkane ligand by reaction with a stronger donor demonstrates the feasibility of reversing this oxidation.

Outer- and inner-sphere electron transfers from [(tpe)Fe(THF)] are localized oxidations accessing different redox reservoirs. Oxidation is specific to the redox reservoir accessed, with no electron transfer between reservoirs. Outer-sphere electron transfer (via chemical or electrochemical means) is dominated by the ligand pyrrolide subunits, while inner-sphere chemical oxidation is mediated by the transition metal.